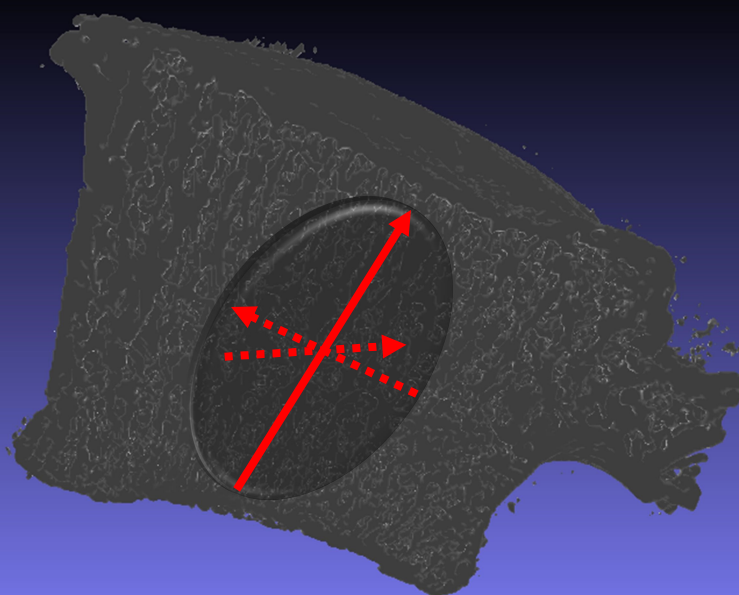


# A Multi-Scale Approach to Implications of the Preferred Vertebral Trabecular Orientation on Spine Biomechanics

Aksel Gudde





# A Multi-Scale Approach to Implications of the Preferred Vertebral Trabecular Orientation on Spine Biomechanics

by

Aksel Gudde

to obtain the degree of Master of Science in Biomedical Engineering  
at Delft University of Technology

Studentnumber: 4470389

Project duration: August 1, 2017 – April 23, 2018

Thesis committee: Prof. dr. ir. H.H. Weinans, TU Delft and UMC Utrecht  
Dr. ir. B. Pouran, TU Delft and UMC Utrecht  
Dr. ir. E.L. Fratila-Apachitei, TU Delft  
Dr. J.J. van den Dobbelsteen, TU Delft

Project supervisors: Dr. ir. B. Pouran  
Dr. ir. V. Arbabi, TU Delft and UMC Utrecht  
Prof. dr. ir. H.H. Weinans

## Acknowledgement

In this short, though sincere, statement I would like to formulate my appreciation for the involvement of my supervisors, Harrie Weinans, Vahid Arbabi and Behdad Pouran, in my graduation project.

I am also thankful for the help given by Bert van Rietbergen, who shared his algorithm and corresponding code “the direct mechanics method”.

The enthusiasm of Harrie Weinans on mechanical fundamentals of bone adaptation and the abstract nature of trabecular quantifications has triggered a deep personal interest to the topic and inspired me to make the best out of this project.

I would like to thank Vahid Arbabi for his involvement and insights on finite element modelling. Furthermore, being pleasant company while doing the research.

Especially I would like to thank my direct supervisor Behdad Pouran, who has supported and motivated me continuously and shown me the relevance of my work. Working together was a truly fun and rewarding experience.

## Abstract

Knowledge of the influence of loading directions on trabecular bone remodeling in spine is of significant value in understanding the development of spine deformities and vertebral bone quality across different scales.

Information on the constitution of a preferred trabecular orientation and mechanical properties of trabecular bone are important indicators in this respect. The current thesis aimed at exploring these aspects across multiple length scales in the spine. The thesis is divided in two parts. The influence of loadings less dominant than compression, i.e. shear, on the constitution of a preferred trabecular orientation in the spine on the macro-tissue level ( $>10$  mm) was investigated in the first part (Part I). This influence was related to mechanical characteristics of trabecular structures on the micro-tissue scale (1-10 mm) in the second part (Part II).

In Part I, primary trabecular orientations ( $PTO_{macro}$ ) near the superior and inferior vertebral endplates of L1 and L5 of 6 human spine cadavers were determined on the macro level using micro computed tomography imaging (voxel size =  $120 \mu m^3$ ), by calculating the dominant fabric principal vector. Their relative deviations to the axial compression vectors in the spines, quantified by the normals to the endplate (NEs), were determined afterwards. The average deviation between the  $PTO_{macro}$  and NEs was  $6.24^\circ (\pm 4.34^\circ)$ . The  $PTO_{macro}$  did not show a preference towards the anterior or posterior direction relative to the NE. From the deviations, it was concluded that trabecular bone in the spine predominantly adapts to compression loads. However, secondary loading directions, such as shear, are of additional influence.

In Part II, 13 small cubes (6.0x6.0 mm) from the volumes of interest in Part I were analysed on the micro level with regard to elasticity. Components, component ratios and primary elastic orientations ( $PEO_{micro}$ ) of elasticity tensors, computed by the simulation of mechanical tests in finite element (FE) models, were calculated.  $PTOs$  of the cubes ( $PTO_{micro}$ ) were compared to the  $PEOs_{micro}$  and related to the  $PTOs_{macro}$  and NEs (Part I) qualitatively. Elasticity tensor components were within a reasonable range (approximately 1-250 MPa, excluding outliers) and no material symmetry was found, i.e. the structures were mechanically anisotropic.  $PTO_{micro}$  deviated  $13.90^\circ (\pm 8.04^\circ)$  with respect to the  $PEOs_{micro}$  on average. 10 out of 13  $PEOs_{micro}$  had similar anterior or posterior tendencies as the  $PTOs_{macro}$  with respect to the NEs. 11 out of 13  $PTOs_{micro}$  had similar anterior or posterior tendencies as  $PTOs_{macro}$  with respect to the NEs.

Elastic properties of typical trabecular structures in the vertebral bodies were successfully determined. Due to a relatively low resolution,  $PEOs_{micro}$  deviated strongly with the  $PTOs_{micro}$ . Such deviations could function as indicators for bone quality in skeletal disease diagnostics using low resolution imaging.  $PTOs_{micro}$  and  $PEOs_{micro}$  agreed relatively well to the  $PTOs_{macro}$  on the macro-tissue level, in terms of anteriorly or posterior tendencies relative to axial loading in the spine. This outcome shows promise for multi-scalar biomechanical analysis of trabecular bone.

## Abbreviations

3D	Three-dimensional
BMD	Bone mineral density
BS/TV	Relative bone surface
BV	Bone volume
BV/TV	Bone volume fraction
DA	Degree of anisotropy
DSO	Design space optimization
EPD	Elastic principal directions
FE	Finite element
FEM	Finite element method
FOV	Field of view
M-CSF	Macrophage colony stimulating factor
MIL	Mean intercept length
NE	Normal to endplate
OPG	Osteoprotegerin
PCM	Pericellular matrix
PEO <sub>macro</sub>	Primary elastic orientation on the macro-tissue level (>10 mm)
PEO <sub>micro</sub>	Primary elastic orientation on the micro-tissue level (1-10 mm)
PGE2	Prostaglandin E2
PTH	Intermittent parathyroid hormone
PTO	Primary trabecular orientation
PTO <sub>macro</sub>	Primary trabecular orientation on the macro-tissue level (>10 mm)
PTO <sub>micro</sub>	Primary trabecular orientation on the micro-tissue level (1-10 mm)
RANK	Receptor activator of nuclear factor $\kappa$ B
RANK-L	" " ligand
S1L1sup	In the superior region of the L1 vertebra in spine number 1
SE	Strain energy
SED	Strain energy density
SLD	Secondary loading direction
TGF- $\beta$	Transforming growth factor $\beta$
TPD	Trabecular principal directions
Tr. N	Trabecular number
Tr. Sp	Trabecular spacing
Tr. Th	Trabecular thickness
TV	Total volume
VOI	Volume of interest
$\mu$ CT	Micro-computed tomography

# Contents

<b>1</b>	<b>Introduction.....</b>	<b>1</b>
Part I: The Preferred Trabecular Orientation in the Vertebral Mechanical Environment		
<b>2</b>	<b>Background .....</b>	<b>4</b>
2.1	<i>Mechanical signalling on the cellular level.....</i>	4
2.1.1	Bone remodeling cycle and mechanical points of action.....	4
2.1.2	Mechanics in the osteocyte environment.....	5
2.2	<i>Trabecular trajectory models .....</i>	6
2.2.1	The trajectorial theory.....	6
2.2.2	Hert's model .....	8
2.2.3	Shear coupling .....	8
2.3	<i>An image-based tool for quantifying trabecular orientation.....</i>	9
2.3.1	Imaging.....	9
2.3.2	Fabric/Mean intercept length.....	10
2.4	<i>Trabecular orientation in vertebrae .....</i>	11
2.4.1	Knowns and unknowns in vertebral trabecular orientation .....	12
2.4.2	Research aim.....	13
<b>3</b>	<b>Methods .....</b>	<b>14</b>
3.1	<i>Micro computed tomography imaging.....</i>	14
3.1.1	Image processing .....	14
3.1.2	Trabecular bone parameters.....	14
3.2	<i>Shear dependent adaptation model.....</i>	16
3.3	<i>Data analysis .....</i>	18
3.3.1	Quantitative analysis.....	18
3.3.2	Qualitative analysis.....	18
<b>4</b>	<b>Results.....</b>	<b>19</b>
4.1	<i>Vertebral configurations.....</i>	19
4.2	<i>Structural parameters .....</i>	19
4.3	<i>Primary trabecular orientations .....</i>	20
<b>5</b>	<b>Discussion .....</b>	<b>23</b>
<b>6</b>	<b>Conclusion .....</b>	<b>25</b>

## Part II:

# The Relation between the Preferred Trabecular Orientation and Elasticity on the Vertebral Trabecular Micro Level

<b>7</b>	<b>Background</b>	<b>27</b>
7.1	<i>Elasticity in trabecular bone</i>	27
7.2	<i>Principal directions of elasticity</i>	27
7.3	<i>Trabecular elastic principal directions in vertebrae</i>	28
7.4	<i>Research aim</i>	29
<b>8</b>	<b>Methods</b>	<b>30</b>
8.1	<i>Segmentation</i>	30
8.2	<i>FE simulations</i>	30
8.2.1	Mesh generation	31
8.2.2	Material properties	31
8.2.3	Contact	31
8.2.4	Steps	32
8.2.5	Boundary conditions	32
8.2.6	Field Output Request	32
8.3	<i>Elasticity parameters</i>	33
8.3.1	The direct mechanics method	33
8.4	<i>Data analysis</i>	34
<b>9</b>	<b>Results</b>	<b>36</b>
9.1	<i>Principal elastic components</i>	36
9.2	<i>Trabecular and elastic orientations</i>	36
9.3	<i>Trabecular and elastic orientations from micro to macro level</i>	38
<b>10</b>	<b>Discussion</b>	<b>40</b>
10.1	<i>Implications for mechanical anisotropy</i>	40
10.2	<i>Relation between trabecular and elastic orientations</i>	41
10.3	<i>Relation between trabecular micro mechanics and spine biomechanics</i>	41
<b>11</b>	<b>Conclusion</b>	<b>43</b>
	<b>References</b>	<b>44</b>
	<b>Appendix</b>	<b>49</b>
A.	Degree of Anisotropy	49
B.	Structural indices	50
C.	Trabecular primary orientation-normal to endplate visualizations	51
D.	Finite element model validation	57
E.	Algorithm rotation to orthotropic elasticity	58





# 1 Introduction

In the field of bone mechanics, it is well-known that the dynamic feature of bone micro is created at an intersection where biological and mechanical factors meet. Although the impact of mechanics on the bone remodeling - the formation and resorption of the micro - has been extensively investigated, the role of the mechanical stimuli on the sustainability of cancellous bone architecture is not fully understood<sup>1</sup>. A distortion of trabecular structure is involved in high prevalence bone diseases, as discussed shortly. Gaining knowledge on the origin and function of these changes is essential for understanding, diagnostics and treatment of bone disorders.

First of all, architectural abnormalities of cancellous bone may lead to diseases that have a local impact at the microscale (30-1000  $\mu\text{m}^*$ ) and micro level (1-10 mm)<sup>2</sup>, such as an increased fracture risk in osteoporosis. Homminga et al.<sup>3</sup> found an increased trabecular longitudinal orientation of osteoporotic vertebral bodies compared to healthy ones. This difference makes the osteoporotic structure more susceptible to infrequent collateral loadings. Similarly, this occurs in osteogenesis imperfecta bones - decreased bone volume fraction and trabecular number and an increased inhomogeneity of the trabecular network - elevating the fracture risk<sup>4</sup>.

In contrast, irregularities in microstructure can also strongly affect the skeleton on the macro-level ( $\geq 10$  mm). In fact, the most common form of osteoporotic diseases, age-related osteoporosis, can lead to a progressive spinal deformity<sup>5</sup>. Here, as a consequence of an accumulation of compression fractures in spine, the height of spine decreases and a progressive thoracic kyphosis develops. Furthermore, Paget's disease, the second most common bone disorder after osteoporosis, is associated with architectural disarrangements of trabecular bone<sup>6</sup>. The effect of this ailment is again apparent on a larger scale, considering the possible evolvement of skeletal deformities or osteoarthritis at joints adjacent to the affected trabecular micro<sup>5</sup>. Moreover, idiopathic scoliosis, a three-dimensional deformity of the spine, is believed to be connected to abnormalities of trabecular microarchitecture. As such, Wang et al.<sup>7</sup> found a reduced trabecular number and connectivity and, consequently, a slightly reduced apparent modulus in the iliac crest of adolescent idiopathic scoliosis patients.

Beside intrinsic processes of the body, architectural organization of trabeculae is of influence when external factors come into play. At implantation sites of orthopaedic devices, the trabecular arrangement can be heavily disturbed. Eventually, this may lead to repeated numbers of revisions and discomfort for patients<sup>8</sup>. By better predicting how trabecular architecture is influenced by the external mechanical cues, it is possible to reduce the risk of implant failure. Furthermore, understanding the growth patterns of trabeculae as a response to scaffolds and grafts, aids in mechanical design approaches in bone micro engineering<sup>9,10</sup>. Finally, the reaction of bone micro and its mechanosensing cells, osteocytes, to stimuli can reveal insights on how cells behave under mechanical stress<sup>10,11</sup>.

As the first examples above imply, microarchitectural and the accompanying mechanical malfunctioning is often defined by a combination of unusual quantities of bone material and disorders in trabecular orientation. Structural parameters of cancellous bone have been reportedly investigated on their mechanical meaning<sup>12-16</sup>. However, a lot of unknowns still remain, in particular, the development of a preferred trabecular orientation, i.e. the primary trabecular orientation (PTO), as a result of mechanical cues.

---

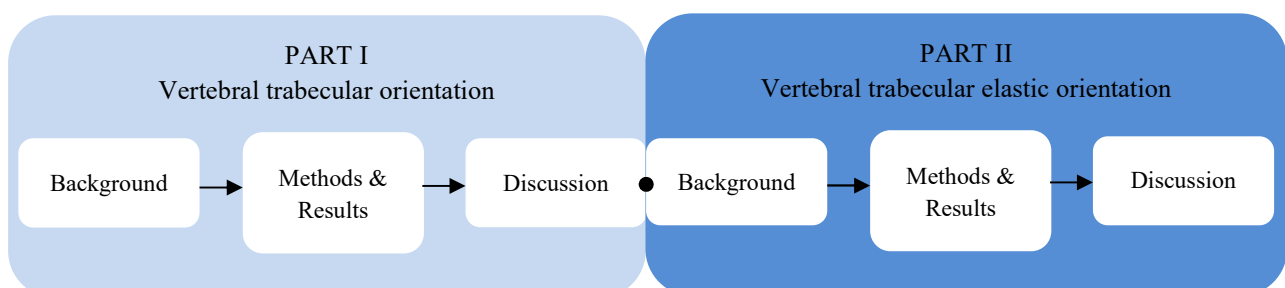
\* The scales in this study are based on literature and defined such that there is a consistency throughout the report. The terms micro-tissue and micro-scale in this report both refer to the tissue scale ranging from 1-10 mm. For the macro-tissue scale and macro-scale, both terms refer to a range  $>10$  mm.

The position of these orientational factors in the mechanical equilibrium of bony structures is clearly remarkable in the field of bone mechanics and mechanobiology.

The trajectorial theory of Wolff<sup>17</sup> has served as a foundation for a better understanding of the relation between trabecular growth patterns and mechanics over the years. A profound number of findings strongly supports this theory<sup>13,18-21</sup>, which states that trabeculae follow the direction of compression and tension lines, leading to an orthogonally arranged structure. However, alternative ideas and contradicting research outcomes<sup>21-24</sup> raise the need for nuance in Wolff's concept. It is suggested that in some situations, complex loadings cause secondary loading directions (SLDs), oblique directed<sup>22,25</sup> and shear forces<sup>23</sup>, to impact bone adaptation next to the more dominant compression and tension. Most studies on the development and directions of trabecular trajectories in relation to loading patterns, have focused on the cancellous architecture of the femur. However, other skeletal parts may be more strongly subjected to SLDs. Vertebral bodies make an interesting candidate, since the presence of shear can be easily identified<sup>26</sup>. For example, in certain spinal deformities, vertebrae are shifted anteriorly<sup>27</sup> or posteriorly<sup>28</sup> with respect to their superior or inferior neighbors, indicating that shear forces are present. Studying the trabecular main orientations of vertebral bodies in relation to the mechanical environment of the bone signifies the influence of loading types other than compression and tension on trabecular bone adaptation.

Trabecular bone mechanics is not only defined by the adaptation of trabecular bone in response to loading, but also by the mechanical function of the resulting cancellous architecture. Namely, trabecular bone adapts to daily forces in order to resist them. The trabecular primary direction can be viewed as being a contributor to the mechanical integrity of cancellous bone. The mechanical character of the main orientation of the trabecular architecture expresses itself through the elasticity of the structure. It has been shown by Odgaard et al.<sup>13</sup> that trabecular principal directions (TPDs) closely correspond to the elastic principal directions (EPDs), directions along which the material stiffness reaches its maximum and minimum. EPDs align with principal stresses. Thus, the trabeculae analyzed in the study additionally followed principal stress directions consistent with Wolff's law. Moreover, the finding of the closely related TPDs and EPDs indicates that trabecular orientation measurements can be used as a tool to predict loading directions in the skeleton's mechanical environment<sup>13</sup>. However, results of more recent work to this relation in human elderly vertebrae<sup>29</sup>, showed less agreement between TPDs and EPDs. Little research has been done on TPDs-EPDs and no study has related the alignment to the mechanical environment of vertebrae to our knowledge. Further research on TPD-EPD alignments in vertebrae is therefore demanding. Such investigation can further verify the influence of SLDs to trabecular bone adaptation. Moreover, in case of close TPD-EPD alignments in vertebrae, dominant loading vectors present in the spine can be identified. Thus, for this particular situation, the alignments help researchers and clinicians to better comprehend the complex biomechanics of the spine.

This thesis focusses on vertebral trabecular mechanics to explore the presence of shear-dependent trabecular bone adaptation on the macro- and micro- tissue level. As such, the project aims at clarifying uncertainties of trajectory theories and dominant force directions in the vertebral mechanical environment. This is done in two parts. Part I focusses on the primary direction of trabecular bone depending on the mechanical environment of vertebrae on the macro level. Trabecular structures are mechanically characterized in Part II in the context of their elastic orientation on the micro level. The latter part consequently contains an analysis of the trabecular and elastic directions across the two scales.



## Part I

# The Preferred Orientation of Trabecular Bone in the Vertebral Mechanical Environment

# 2 Background

## 2.1 Mechanical signalling on the cellular level

The development of the arrangement of trabeculae is ultimately a result of the bone homeostasis that is maintained at a cellular level. This process, called bone remodeling, consists of 5 stages of activation, bone breakdown, i.e. resorption, formation and quiescence (termination). The teamwork between bone resorbing osteoclasts, bone forming osteoblasts and mechanosensing osteocytes, is believed to be potently driven by the mechanical stimuli. Other involved factors are cytokines and hormones<sup>30</sup>, as will be elaborated shortly. Osteoclast and osteoblasts execute their tasks and move in close proximity together with a group of mononuclear cells, responsible for the removal of collagen debris remaining from the resorption phase<sup>31</sup>. These dense functional packets total of the cells mentioned above goes by the name of the basic multicellular unit (BMU)<sup>32</sup>. The constitution of a mechanically stable architecture by BMU-activity is reflected in two ways.

Firstly, the BMU has a protective function, by designing the bone architecture such that it can resist daily external forces and body mass. Furthermore, remodeling offers repair of damaged bone in order to maintain structural integrity. Microdamage induces the assemblage of osteoclasts that remove damaged micro and osteoblasts follow to regain bone material. This form of the process is frequently named targeted remodeling<sup>33</sup>.

Both mechanisms are eventually realized by mechanotransduction, the conversion of a mechanical stimulus in the secretion of molecules by the cells. In bone, this function is primarily executed by the osteocytes<sup>34,35</sup>.

### 2.1.1 Bone remodeling cycle and mechanical points of action

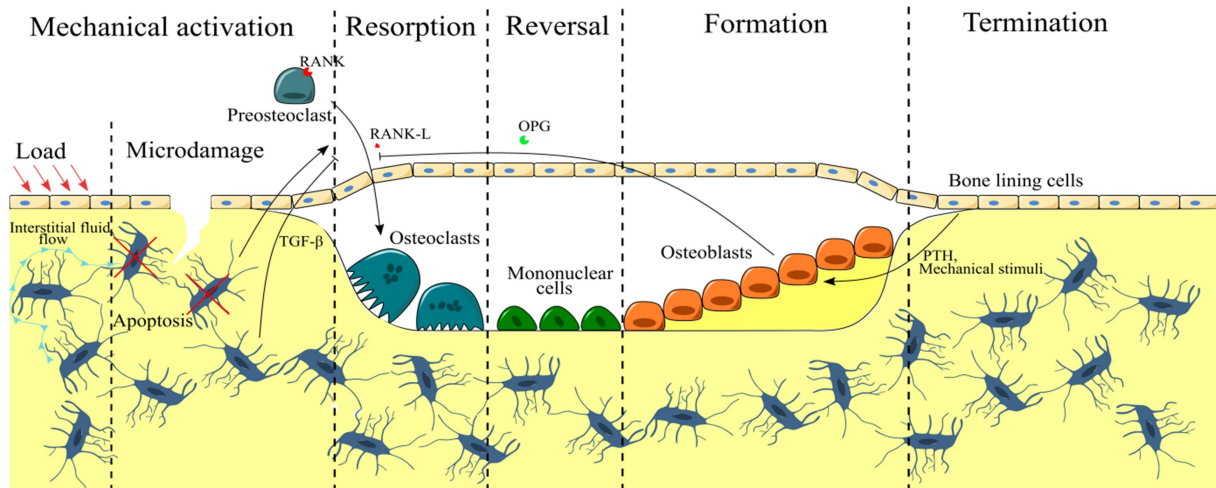
From a mechanical perspective, the remodeling cycle is initiated by strain or fatigue sensed in the osteocyte environment<sup>31,36</sup>.

For the microdamage-induced remodeling (targeted remodeling), research has indicated that the cycle starts with the apoptosis of osteocytes adjacent to a microcrack<sup>37</sup>. Under living conditions, osteocytes secrete transforming growth factor  $\beta$  (TGF- $\beta$ ), which has been shown to inhibit osteoclastogenesis<sup>38</sup>. After apoptosis, the osteocytes cease to produce TGF- $\beta$ , allowing the formation of osteoclasts<sup>31</sup>.

Osteoclastogenesis starts with the generation of mononuclear cells (preosteoclasts) from hematopoietic stem cells after being stimulated by macrophage colony stimulating factor (M-CSF)<sup>30</sup>. When preosteoclasts enter the bloodstream, they fuse to form immature osteoclasts as a result of the binding of receptor activator of nuclear factor  $\kappa$ B ligand (RANK-L) to its receptor RANK<sup>39</sup> and the presence of M-CSF<sup>30</sup>. Due to osteoclastic gene expression and continuous presence of RANK-L, osteoclasts mature. After reaching the damaged bone site, osteoclasts use  $\alpha$ v $\beta$ -integrin receptor to form an adhesion with the bone matrix<sup>40</sup>. Osteoclasts transfer acids ( $H^+$  and HCl) into the extracellular environment to demineralize the bone<sup>41</sup>, after which the resorption phase is concluded.

In the wake of the osteoclasts, some collagen is leftover, which is digested by mononuclear reversal cells<sup>31</sup>. Over the course of this so-called reversal phase, these cells mature into the bone forming osteoblasts<sup>42</sup>. Alternatively, osteoblasts can evolve from bone lining cells that are located at a bone region in rest. These quiescent cells are stimulated mechanically or by intermittent parathyroid hormone (PTH).

Mature osteoblasts produce unmineralized bone matrix composed of collagen I and osteocalcin. Mineralization takes place under the activity of alkaline phosphatase afterwards, which is additionally secreted by the osteoblasts<sup>30</sup>. During the activity of bone formation, osteoclastogenesis is prevented due to



**Figure 1:** Basic multicellular unit (BMU) activated to execute the bone remodeling cycle as a result of microdamage.

the production of the soluble decoy receptor osteoprotegerin (OPG) by the osteoblasts. OPG binds to RANK-L as a competitor for RANK, thus blocking the RANK/RANK-L binding necessary for bone resorption<sup>30,43</sup>.

While a line of active osteoblasts moves away from the bone surface, a part of the cells is left behind in the newly produced matrix. These cells develop long processes that function as communicators with the neighboring cells. Research suggests that the dendrite elongation is a result of mechanical loading<sup>44,45</sup>. As the matrix mineralizes the precursors start to mature to become osteocytes<sup>30</sup>, ending the remodeling cycle. In Figure 1 an overview of the remodeling cycle is shown.

### 2.1.2 Mechanics in the osteocyte environment

Beside microdamaging bone, mechanical loading can trigger osteocytes by causing a pressure differential in the fluidic interstitial spaces between bone matrix and the osteocyte body and processes, named lacunae and canaliculi, respectively<sup>34</sup>. Weinbaum et al.<sup>46</sup> proposed that the lacunar-canalicular network consists of pericellular matrix (PCM) of the monomeric heparin sulphate proteoglycan perlecan<sup>47</sup> with pores through which fluid flows due to the pressure gradient.

Wang et al.<sup>48</sup> proposed a model to explain how the flow of the interstitial fluid could possibly initiate intracellular processes. The perlecan proteins function as transverse tethering elements<sup>47</sup>, that connect the canalicular wall to cross-filaments via transmembrane proteins. Intracellularly, the cross-filaments are bonded to an actin filament bundle. When fluid flows, the tethering elements get stretched. Since the transmembrane proteins are intracellularly coupled to the actin filaments<sup>49</sup>, the strain in the tethering elements gets transmitted to the cytoskeleton of the osteocyte. As a result, the actin filaments slide and deform. Deformation of the actin filament bundle is sensed by integrins in the process membrane. The integrins get mechanically activated, inducing a cascade of intracellular processes. These processes include the spread of  $Ca^{2+}$  from the osteocyte process to the osteocyte body<sup>50</sup> and increased expression of the lipid prostaglandin E2 (PGE2)<sup>51</sup>. PGE2 recruits precursor cells and promotes them to differentiate into osteoblasts<sup>52</sup>. Furthermore, studies have indicated that cytoskeletal deformation of osteocyte-like cells leads to an increased Wnt gene expression<sup>11</sup>, of which the signalling inhibits osteoclast differentiation<sup>53</sup>.

These findings support the reasoning that bone remodeling, thus the development of trabecular trajectories is orchestrated by osteocytes under the influence of mechanical loading via deformations on the substrate level.

## 2.2 Trabecular trajectory models

Extensive research has been carried out on stimulated trabecular bone adaptation as a consequence of mechanical loading. The theoretical basis for this relation started more than a century ago with the idea of Julius Wolff that trabeculae grow directionally such that they can resist the principal stresses most efficiently, known as Wolff's law or trajectorial hypothesis<sup>17</sup>. Herein, efficiency was defined by Wolff as the minimum mass necessary to obtain mechanical reliability<sup>17,54</sup>. This aspect of bone remodeling has frequently been simulated with the finite element method (FEM), especially to model femoral components<sup>54-59</sup>.

As principal stresses follow compression and tension vectors, the trabeculae are in general believed to align accordingly<sup>18,24,60</sup>. Adachi and co-workers<sup>58,59</sup> simulated bone remodeling at the surface of trabeculae following a variety loading patterns. It was found that their models are capable of predicting the functional adaptation of trabecular bone from the microscale up to the micro level in accordance to Wolff's law. Jang et al.<sup>54</sup> constructed a similar adaptation model by using topology optimization, a simulation that iteratively distributes material to certain regions of an object – in this case trabecular bone – such that it leads to an optimal material arrangement. For example, regions of relatively high strain energies gain material, whereas low strain energy-regions lose material.

Although these models showed supporting findings for the trajectorial hypothesis, some doubt still exists regarding skeletal regions where more complicated loading patterns and shear play a role<sup>10,23,24,60,61</sup>, which will be elaborated in sections 2.3.2 and 2.3.3.

### 2.2.1 The trajectorial theory

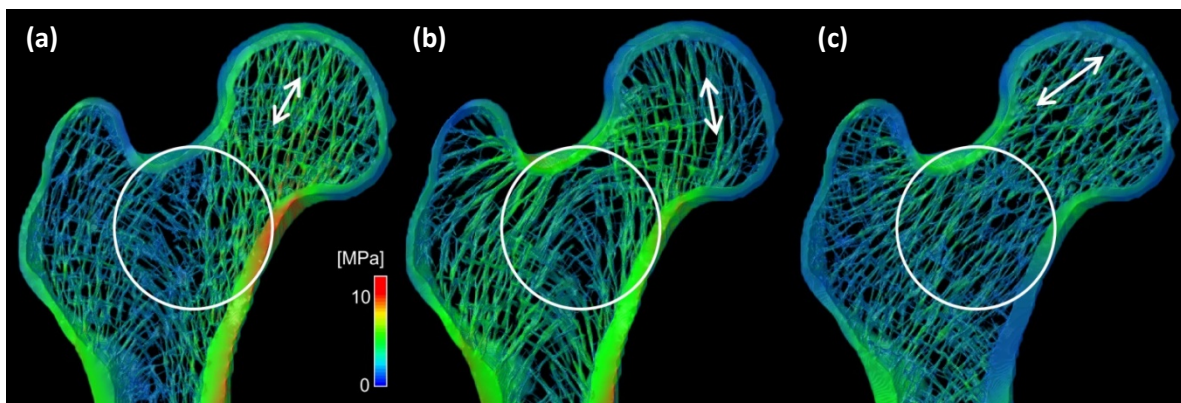
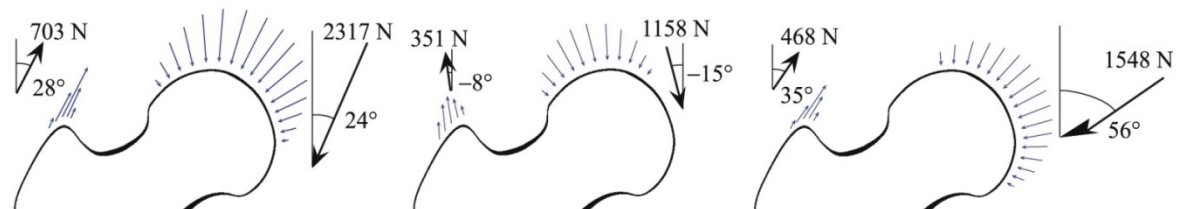
The development of trabecular orientation in response to mechanical stimuli that support the trajectorial hypothesis has been frequently simulated. For example, Mullender and Huiskes<sup>62</sup> set up a model that took the function of mechanically sensitive osteocytes to modulate bone mass adaptation through osteoclast- and osteoblast-activity. During simulation, a structure was created that showed close resemblance with a typical trabecular architecture. In fact, when altering loading patterns, the strut's orientation changed such that it aligned with the principal stress directions. Huiskes et al.<sup>55</sup> have quantified bone formation and resorption in terms of changes in shape and density. They considered the strain energy density (SED) – by definition the strain energy per unit bone volume in MPa – to be the stimulus.

Although the SED-model of Huiskes and co-workers<sup>55,56</sup> has been adopted in different simulations<sup>54,57,63,64</sup>, Adachi et al.<sup>58</sup> considered an alternative stimulus. A model was developed that simulated bone remodeling at the surface of trabecular struts to predict changes in the structure's architecture. Here, the remodeling was assumed to be driven by local stress nonuniformities in the trabeculae in order to eventually establish a uniform stress state.

Based on the non-uniformity remodeling approach of Adachi et al.<sup>58</sup>, co-authors<sup>18</sup> simulated a 3D FE-model of the femur that mapped changes in trabecular orientation following different loading situations. An initial isotropic (material properties are equal in all directions) and uniform porous trabecular structure was assumed. Three loading cases – one legged stance, abduction and adduction – were applied afterwards. Following the selective apposition and resorption of bone by the non-uniformity-model, the trabecular structure responded to the loadings. The trabeculae of the femoral head were found to align with the direction of the different loadings, as shown in Figure 2. The trabecular structure within the femoral neck was orthogonally patterned for the one legged stance and abduction (Figure 2a and b). This finding was explained by the presence of a clockwise bending moment due to the loading at the articular surface. The adduction loading aligned with the orientation of the femoral neck, thereby preventing a bending moment. As a result, a unidirectional trabecular orientation was seen (Figure 2c). In addition, results showed close correspondence between the principal trabecular directions and stresses. Thereby, the non-uniformity model supports the trajectory theory of Wolff<sup>17</sup>.

Boyle and Kim further reinforced Wolff's law in a FE-model of the proximal femur<sup>19</sup>, using a specialized technique of topology optimization, named design space optimization (DSO)<sup>65</sup>. Topology optimization drives changes in a solid architecture by adding mass at locations where loadings are largest<sup>66</sup>. In this way, the method tries to obtain maximum stiffness and a uniform strain energy (SE) over a domain of the structure. DSO is a form of topology optimization where material is added and removed at high and low loading regions, respectively, following recorded SE values. The uniqueness of DSO lies in its ability to map the adaptation progress over time<sup>19</sup>. The trabecular remodeling simulation of Boyle and Kim strives for the ideal combination of maximum strength and minimum weight. To secure this feature, the DSO bone adaptation simulation was initiated in an isotropic state under physiological loading conditions and run until the smallest global SE value was reached<sup>19</sup>. Results of the study showed alignment of the trabecular structure with the principal stresses. Furthermore, using topology optimization, Wolff's law was supported from the perspective that bone is an optimum material; The orientation is developed in such a way that minimum bone micro was needed to satisfy the mechanical demands.

Trabecular bone has experimentally been accepted to have its anisotropy most closely resembled by orthotropy (material properties differ along three orthogonal axes)<sup>67-69</sup>. Nevertheless, in trabecular trajectory simulations, many bone adaptation models assume isotropic material properties to lower the computational time<sup>55,70,71</sup>. Fernandes et al.<sup>72</sup> already modeled cancellous bone as an orthotropic material in an early topology optimization model of the femoral head to support Wolff's trajectory theory. However, not for all applied loading cases, an alignment of principal strains and orthogonal directed trabeculae were found. Therefore, it was suggested that an optimal orientation of trabeculae is not completely bounded to an orthotropic microstructure. Still, Gerdal et al.<sup>73</sup> argued bone adaptation models that assume an initial non-orthotropic state of trabecular bone. In their FE study of the complete femur, an alternative adaptation algorithm was developed that started with an orthotropic trabecular structure and an orientation already aligned with the principal stresses following Wolff's law. In comparison to an isotropic approach, the orthotropic model provided better bone density predictions and new information on material orientation.



**Figure 2:** The FE trajectory adaptation model in one-legged stance (a), abduction (b) and adduction (c). The arrows represent the main loading directions applied to the femoral head. The circles circumvent the trabeculae of the femoral neck. Here, the structure shows an orthogonal pattern for situation (a) and (b) (notice higher stress region around the femoral neck due to the bending moment) and a unidirectional pattern for situation (c).<sup>18</sup>



In summary, the described simulation models gave advanced directional adaptation predictions of trabecular responses to mechanical loadings. Furthermore, they accurately agreed with the Wolff's law, implying a step forward to a general consensus regarding the relation between mechanical stimuli and preferential trabecular orientation. Finally, taking anisotropic factors into account, allows researchers to better refine trajectory simulations.

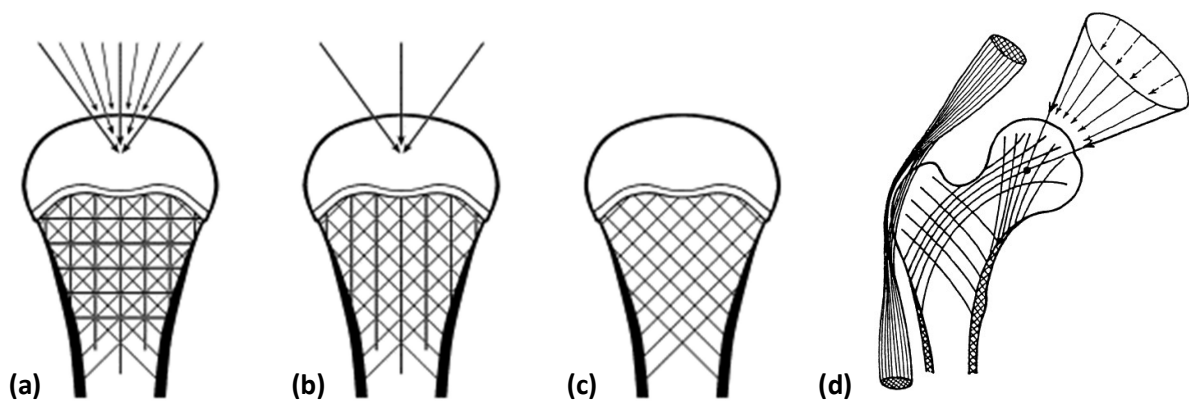
### 2.2.2 Hert's model

Although the models mentioned in the previous section indeed strongly support Wolff's law, some findings have failed to clearly imply the same. Firstly, the early observation that non-orthogonal directed trabeculae appear at sharp and obtuse angles, contradict the  $90^\circ$  trabecular alignment of Wolff's trajectory<sup>74</sup>. Likewise, a non-orthogonal microstructure in the frequently modeled femoral neck is observed<sup>18,23–25,54,74,75</sup>. Studies suggest that trabecular orientation develops due to multidirectional joint loads, rather than a unidirectional loading as proposed by Wolff<sup>74</sup>.

First of all, following Hert<sup>23,25</sup>, oblique loading from the extreme positions on a joint are dominant over axial loading. As a result, secondary trabeculae that arise from the primary spongiosa (trabecular structure that forms as replacement for cartilage during early skeletal development<sup>76</sup>) are more stimulated in the oblique directions, hence create a non-orthogonal structure<sup>22</sup>. Hert's model is displayed in the form of a fictional joint in Figure 3. Moreover, Skedros and Baucom<sup>24</sup> evaluated the trajectory hypothesis by analyzing the cancellous architecture of relatively simply loaded skeletal parts (sheep and deer calcanei) and cantilevered beams (compressive and tensile stress trajectories were drawn from earlier studies) and more complex loaded skeletal parts (human and chimpanzee proximal femur). The results showed orthogonal structures for the straightforward loaded samples and non-orthogonal alignments in the neck region of the complex loaded femurs. The topology optimization model of the human proximal femur by Jang and Kim confirmed these findings<sup>54</sup>. Measured trabecular intersection angles at the femoral neck and trochanter indicated non-orthogonal and orthogonal alignments, respectively, and were in close correspondence with those predicted by Skedros and Baucom.

### 2.2.3 Shear coupling

Furthermore, multi-directional loading is thought to cause non-orthogonal patterns in certain skeletal regions due to shear-dependent bone adaptation<sup>24</sup>. This belief is based on the finding that trabecular bone is weaker when subjected to shear than subjected to compression and tension in failure tests<sup>61,77</sup>. Since bone ideally adapts in a way that its weakest portions grant priority, bone matrix should be produced in a way to strengthen the micro in the shear direction, which is accommodated by the formation of a non-orthogonal



**Figure 3:** Hert's model of oblique dominant loading stimuli. **a** Bone is subjected to alternating directed loadings. **b** Oblique loadings cause more strain in oblique directed trabeculae than compressive loadings do on axial trabeculae. **c** Therefore bone is dominantly formed in the oblique directions, ultimately leading to a structure of oblique struts. **d** In this manner Hert accounted for the non-orthogonal pattern in the femoral neck.<sup>24</sup>

structure<sup>24</sup>. This idea was later supported in a study where differences were found in micro-damage buildup in cancellous bone between compressive and shear loadings<sup>78</sup>.

Moreover, a recent study reinforced the involvement of shear in trabecular alignment after finding peak shear moduli in a FE-model of the femur at regions that are associated with non-orthogonal trabecular patterns<sup>79</sup>.

Finally, Pidaparti and Turner<sup>23</sup> proposed a model that predicts non-orthogonal alignments resulting from shear coupling caused by multidirectional loading. In this explanation, anisotropic materials such as trabecular bone are subjected to shear coupling when the principal stress direction is not aligned with the material symmetry axis. Cancellous bone homeostasis should find a way to limit the impact of the large strains that may follow shear coupling. The model showed that a non-orthogonal alignment of trabeculae under multi-directional loading reduced the shear coupling effect 33-75% as opposed to the orthogonal alignment of Wolff. Thus, following this model, trabecular bone adapts its structure to multi-directional loadings in a non-orthogonal fashion so that it reduces a shear coupling effect to obtain more mechanical integrity.

Although Wolff's trajectory hypothesis has been widely recognized over the years, more recent studies show that the theory does not always completely hold. Especially with regard to Wolff's view that orthogonality results from compression and tension lines, contradicting studies have implied that multi-directional loadings may cause shear stresses to alter trabecular orientation.

## **2.3 An image-based tool for quantifying trabecular orientation**

Several measurement tools are available to study the micro-architectural arrangement of the trabecular bone. To perform analysis on the bone quantity in a cancellous structure, indices namely, bone mineral density (BMD), porosity, relative bone surface (BS/TV), bone volume fraction (BV/TV), trabecular thickness (Tr. Th), trabecular separation (Tr. Sp) and trabecular number (Tr. N) are used<sup>3,15,16,80</sup>. BS/TV and BV/TV here are defined as the trabecular bone surface and volume, respectively, normalized over the total volume of a sample<sup>15</sup>. Structural indices are relevant for the diagnosis and understanding of bone diseases<sup>81</sup>. They are useful tools when assessing the mechanical quality of bone. For example, it has been shown that BV/TV is a good predictor of strength and elastic modulus<sup>15,82</sup>. However, it is necessary to know the orientation of the trabecular structure for a better prediction of the mechanical properties of the cancellous bone. Trabecular orientation is determined in terms of the structure's principal directions.

The most common method to quantify these directions, is to calculate the fabric of the trabecular bone. Fabric was firstly defined by Cowin to characterize the microstructural arrangement of a porous or multiphase material<sup>83</sup>. The tool is denoted by a second order tensor, which can be plotted as an ellipsoid. The orthogonal axes of the ellipsoid correspond to the material's principal directions. Furthermore, fabric allows for the determination of anisotropic features of a structure. Anisotropy is defined by the difference in quantity of a material property per orthogonal direction. Since anisotropy is a different property of cancellous bone than trabecular orientation, these features are described by different aspects of the fabric tensor (section 2.3.2).

### **2.3.1 Imaging**

Micro-computed tomography ( $\mu$ CT) is a relatively new imaging technique, that has been shown to be very effective when used to quantify structural parameters of trabecular bone<sup>84</sup>.  $\mu$ CT is capable of segregating hard from soft micro with a resolution up to a few microns<sup>85</sup> in three dimensions (3D) non-destructively<sup>86</sup>. Quantifying the desired parameters using  $\mu$ CT-imaging requires the three steps, sample preparation and scanning (1), image pre-processing (2) and post-processing (3). Sample preparation and scanning, as it implies, involves setting up the materials such that scanning of the appropriate part of the specimen is possible<sup>87</sup>. The scanning settings, such as scanning time, field of view and resolution need to be specified.

The images are often binarized during pre-processing to make the output of a  $\mu$ CT-scan useful for structural analysis<sup>88</sup>. An accurate binary representation of the sample is obtained by adjusting the brightness and contrast of the images, thresholding them and removing noise. Choosing regions of interest and segmentation is also part of pre-processing. Commercial software<sup>89</sup> is available, that offer in-built algorithms allowing for executing the pre-processing tasks. Finally, post-processing is the actual calculation of the parameter values based on the pre-processed images<sup>90</sup>. Different methods and algorithms are used to acquire the quantities. The most common one for obtaining fabric based trabecular orientation is described in the subsequent section.

### 2.3.2 Fabric/Mean intercept length

The mean intercept length (MIL) is the gold standard for quantifying the orientation of anisotropic materials by means of fabric. Furthermore, this fabric tensor has often been used in relation to mechanical properties of trabecular bone<sup>13–16,80,91</sup>. This technique is therefore focused on in this study. In order to do so, firstly, the MIL is used as an example to explain how the trabecular principal direction can be determined from fabric tensor calculation.

The MIL is defined as the total length  $L$  of the linear grid placed on the microstructure (Figure 4a), divided by the number of bone/marrow intersects  $I$ . Mathematically this is simply expressed by

$$\text{MIL}(\omega) = \frac{L}{I(\omega)} \quad (1)$$

where  $\omega$  is the 3D orientation of the grid<sup>13,92,93</sup>. This grid-angle means the measurement is performed in a specific direction. This direction can be projected in a Cartesian coordinate system in the form of a unit vector  $\mathbf{n}$ . The MIL is plotted by relating  $\mathbf{n}$  to the Cartesian coordinates as follows<sup>94</sup>

$$\begin{aligned} x_1 &= \text{MIL}n_1 \\ x_2 &= \text{MIL}n_2 \\ x_3 &= \text{MIL}n_3 \end{aligned} \quad (2)$$

where  $[n_1, n_2, n_3] = \mathbf{n}^T$ . An ellipsoid serves as a suitable approximation to graphically summarize the MIL measurements. In general an ellipsoid is mathematically described by the following formula<sup>95</sup>

$$m_{11}x_1^2 + m_{22}x_2^2 + m_{33}x_3^2 + 2m_{23}x_2x_3 + 2m_{13}x_1x_3 + 2m_{12}x_1x_2 = 1 \quad (3)$$

Combining Eq. (3)  $m_{11}x_1^2 + m_{22}x_2^2 + m_{33}x_3^2 + 2m_{23}x_2x_3 + 2m_{13}x_1x_3 + 2m_{12}x_1x_2 = 1$   
(3with Eq. (2) then gives<sup>94</sup>

$$\text{MIL}^2(m_{11}n_1^2 + m_{22}n_2^2 + m_{33}n_3^2 + 2m_{12}n_1n_2 + 2m_{13}n_1n_3 + 2m_{23}n_2n_3) = 1 \quad (4)$$

Alternatively, this could be summarized as

$$1/\text{MIL}^2 = \mathbf{n} \cdot [\mathbf{M}] \cdot \mathbf{n} \quad (5)$$

where  $[\mathbf{M}]$  represents the second order MIL fabric tensor, fully written as

$$[\mathbf{M}] = \begin{bmatrix} m_{11} & m_{12} & m_{13} \\ m_{21} & m_{22} & m_{23} \\ m_{31} & m_{32} & m_{33} \end{bmatrix} \quad (6)$$

The ellipsoid representation is a general graphical way of visualizing the fabric tensor. The principal axes of the ellipsoid are found by decomposing the fabric tensor into its characteristic eigenvalues and eigenvectors, which determine the magnitude and orientation, respectively, of the ellipsoid's radii<sup>92,96</sup>. The primary principal axis of the material (trabecular structure) corresponds to the orientation of the largest radius and thus largest eigenvector of the ellipsoid. Since the radius  $R_i$  of the ellipsoid is related to the eigenvalue  $\lambda_i$  as

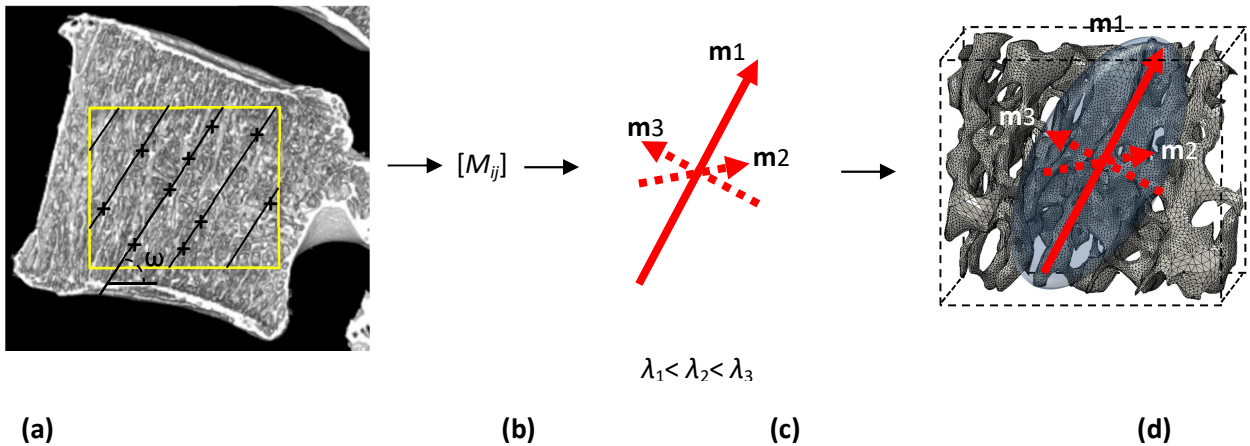
$$\lambda_i = (1 / R_i)^2 \quad (7)$$

the largest eigenvector belongs to the smallest eigenvalue<sup>92,94</sup>. Theoretically this relation is explained by a small eigenvalue indicating a long MIL and less boundaries per unit of length. In Figure 4 an overview of the steps to obtain the ellipsoid representation with the trabecular principal directions from a single MIL calculation is given.

Although trabecular orientation and structural anisotropy are both determined by fabric factors, they do not influence each other mathematically. Where the microstructure's principal trajectories are defined by the direction of the fabric eigenvectors, anisotropy is quantified by the ratio between their minimum and maximum magnitudes, depicted by the maximum and minimum eigenvalues, respectively<sup>97</sup>. The latter description makes sense considering that the degree of anisotropy (DA) is the extent to which a material property differs per direction. Mathematically the DA is given by

$$DA = 1 - \frac{\lambda_{\min}}{\lambda_{\max}} \quad (8)$$

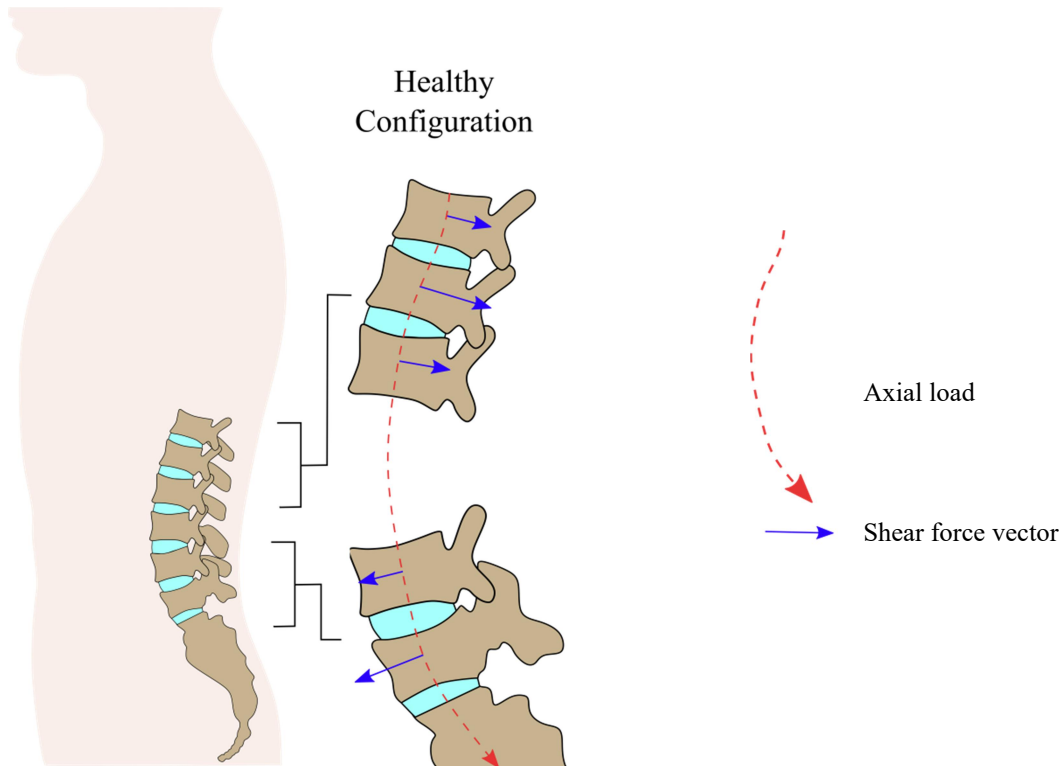
where  $\lambda_{\min}$  and  $\lambda_{\max}$  are the minimum and maximum eigenvalues of the fabric tensor, respectively<sup>98</sup> and  $DA < 1$ . It can be easily seen that the larger the DA, the less isotropic is the material. In ellipsoid representation, it shows that a smaller DA, thus more similar magnitudes of the principal directions, leads to a more spherical geometry.



**Figure 4:** The steps required for obtaining the fabric ellipsoid from a mean intercept length (MIL) measurement. **a** One MIL calculation of vertebral trabecular bone imaged using micro computed tomography at a grid angle  $\omega$ . **b** MIL fabric tensor calculation. **c** Eigendecomposition providing eigenvectors  $\mathbf{m}$  and eigenvalues  $\lambda_i$ . **d** Ellipsoid with corresponding eigenvectors representation.

## 2.4 Trabecular orientation in vertebrae

Thus, as Lanyon<sup>60</sup> already mentioned in an early study to the trabecular orientations in sheep calcanei, the bone's internal structure may not adapt so straightforwardly to its environment as suggested by the



**Figure 5:** The vertebral inclinations cause vertebrae to be subjected to shear loads.

trajectorial hypothesis, especially in complex loading cases. The alternative ideas by Pidaparti and Turner<sup>23</sup> and Hert<sup>22</sup>, reinforced by the work of Skedros and Baucom<sup>24</sup> (sections 2.2.2 and 2.2.3), raise the need for exploring the influence of shear on trabecular orientation. Given that most of the studies reported in this work have focussed on the trabecular architecture of femurs, expanding the range of skeletal sites could substantiate the understanding of trabecular bone adaptation to this respect.

Vertebral bodies are an interesting candidate since the degrees of freedom of the spine allows for multi-directed loadings. Flexion and extension, lateral bending and axial rotation cause vertebrae to be subjected to a variety of shears throughout one's lifespan. Moreover, in the sagittal plane, the spine curvature creates a difference in orientations between vertebrae. The inclinations of vertebrae due to the curve result in anterior and posterior shear<sup>26</sup>, as presented in Figure 5. In some cases of spinal deformities, vertebrae are shifted anteriorly or posteriorly with respect to their superior or inferior neighbours, indicating an increase of shear forces compared to a healthy alignment of vertebrae in the spine.

#### 2.4.1 Knowns and unknowns in vertebral trabecular orientation

The influence of loadings different from compression on trabecular adaptation in vertebrae was brought to the attention in a study by Smit et al.<sup>99</sup> An x-ray image taken from the sagittal plane showed that trabeculae were densely concentrated at the pedicles and diverged towards the superior and inferior endplate as if they formed a fan-shaped structure. After quantifying trabecular orientations in different regions of a vertebra in terms of MIL fabric eigenvectors, the trabeculae were found to predominantly follow axial compression. A later investigation by Smit and co-workers<sup>100</sup> found a dominance of compression lining trabeculae in the spine of a sheep, although it was emphasized that the spine biomechanics of quadruped cannot be directly reflected on the human situation. Furthermore, Homminga et al.<sup>3</sup> found a preferred trabecular orientation in the longitudinal direction in an osteoporotic vertebra in comparison to a healthy vertebra. As a response to loss of bone, the micro was encouraged to adapt itself to dominant axial loadings. With their findings these studies were able to reinforce the applicability of the trajectorial theory in vertebral trabecular bone adaptation.

However, some calculations performed by Smit et al.<sup>99</sup> indicated misalignment of trabecular trajectories with respect to the compression line, which could be due to bone adaptation to shear forces.

Although trabecular orientation in vertebral bodies using fabric has been quantified in a number of studies, the relation between the dominant orientation of the trabeculae in relation to spine mechanics has barely been investigated. A clear view of the influence of shear forces to bone adaptation in vertebrae thus remains unclear.

#### 2.4.2 Research aim

The aim was to point out whether there is an influence of anterior and posterior shear forces in the spinal column on vertebral primary trabecular orientation (PTO) on the macro level (>10 mm). Since the inclination differences and the shifts are likely to be a continuous source of anterior and posterior directed shear in the spine, an analysis of vertebral PTO in relation to the loadings in the spine, could provide insights in the influence of shear on trabecular bone adaptation.

Therefore, the aim could be tackled by fulfilling the combination of the following three main tasks:

1. Determining the angle between the primary fabric direction of trabecular bone, i.e. PTO, in human vertebrae to the axial compression line in the spine in the sagittal plane.
2. Determining the average tendency of a part of the structure to be anteriorly or posteriorly oriented with respect to the axial compression line.
3. Relating these aspects to shear directions predicted from the configuration of the vertebrae in spine.

# 3 Methods

## 3.1 Micro computed tomography

Two vertebral bodies that show a relatively large orientation difference in a healthy spine, L1 and L5, were chosen for the analysis. The L1 and L5 belonged to 6 cadaveric human spines with ages approximately between 75 and 90 years and sex unknown.

All samples were scanned using a  $\mu$ CT system (Quantum FX, PerkinElmer, Waltham, MA, USA) at the using a tube voltage of 90 kV and tube current of 180  $\mu$ A. Spines were ideally placed in the cylindrical sample holder as a whole. A field of view (FOV) was set to 60 mm so that a scan could capture the entire vertebral body<sup>101</sup>. In case a spine did not fit the  $\mu$ CT entirely, it was cut between L2 and L3 and between T12 and T11. The spatial resolution of the scans was 120  $\mu\text{m}^3$ , which was the highest resolution for the size of the samples and 3600 projections were made during a scan time of 2 minutes.

### *Image processing*

The images were binarized using Fiji (ImageJ)<sup>89</sup> after brightness and contrast adjustments. Next, Phansalkar was chosen as the standard auto local threshold method. If necessary, noise was removed. The volumes of interest (VOIs) for analysis on trabecular structures were selected according to the portions of the vertebrae where shear is most likely of influence. It was assumed that, when there is a shift between vertebrae in the spine, the resulting shear is largest nearby the endplates. In this line of reasoning, the superior and inferior one-thirds of each vertebral body were chosen as VOIs. Calculations of trabecular parameters based on these VOIs were on the macro level (section 1), as they comprised the entire width of a human vertebra (>10 mm).

The trabecular structures defined by the VOI domains were named S1L1<sub>sup</sub>, S1L1<sub>inf</sub>, S1L5<sub>sup</sub>, S2L1<sub>sup</sub>, etc., where the subscript refers to the superior or inferior region of the vertebra, L1 depicts the anatomical name of the vertebra and S1 is an abbreviation for spine number 1.

Only trabecular bone was included in the VOIs for these analyses. Finally, VOIs of the superior and inferior endplates were taken for the normal to endplate (NE) calculation, as further explained in the subsequent paragraph.

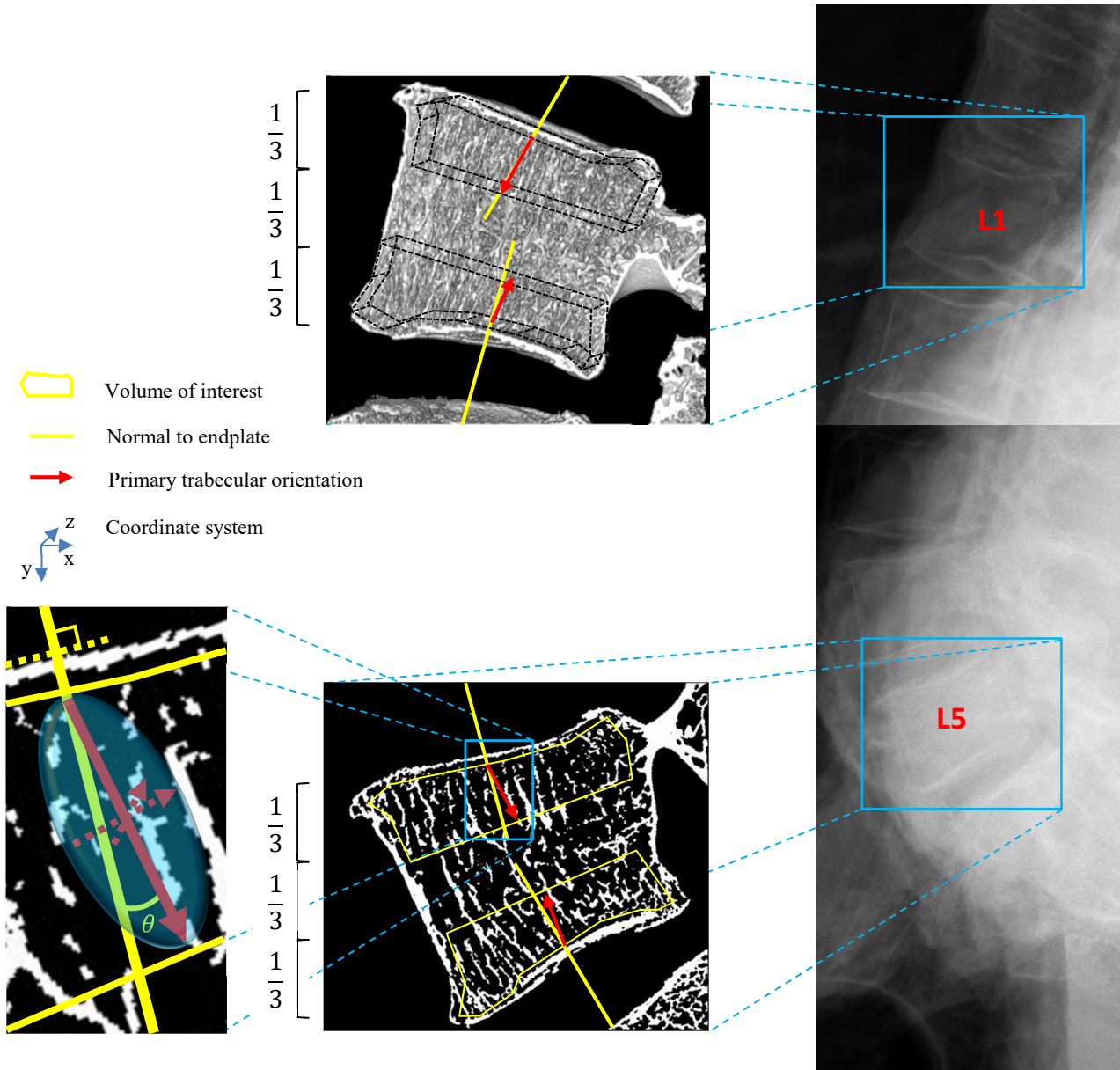
### 3.1.1 Trabecular bone parameters

For each VOI of trabecular micro the BV/TV, Tb. Th, Tb. Sp, were calculated and compared with previous work as a rough indicator of the quality of the bone structures. All structural parameters were calculated using the BoneJ<sup>102</sup> plugin provided by Fiji (ImageJ). DA was calculated in Fiji based on the ratio between the minimum and maximum eigenvalues,  $\lambda_{\min}$  and  $\lambda_{\max}$ , respectively, of the MIL fabric tensor as  $DA=1-(\lambda_{\min}/\lambda_{\max})^{94}$ .

BoneJ allows for the option to record eigenvectors and eigenvalues of the MIL fabric tensor during the calculation of DA. The eigenvectors and eigenvalues were given by Fiji in the following form

$$\begin{bmatrix} v_{11} & v_{12} & v_{13} \\ v_{21} & v_{22} & v_{23} \\ v_{31} & v_{32} & v_{33} \end{bmatrix} \text{ and } \begin{bmatrix} \lambda_1 & 0 & 0 \\ 0 & \lambda_2 & 0 \\ 0 & 0 & \lambda_3 \end{bmatrix}$$

respectively, where each column of the eigenvector matrix represented the coordinates of one fabric principal direction. The vector-column corresponding to the column of  $\lambda_{min}$  contained the coordinates of the primary fabric direction, thus the  $PTO_{macro}$ . As the PTOs and NEs in the current part were based on VOIs and endplate regions on the macro level, they are depicted by  $PTO_{macro}$  and  $NE_{macro}$ , respectively. A small error tolerance ( $error_{max} = 0.0005$ ) was specified before running the DA and fabric eigenvector computation. The DA showed a clear convergence over the number of iterations towards the solution. The validation by



**Figure 6:** The trabecular primary principal directions of the superior and inferior one-thirds in the L1 (above) and L5 (below) vertebral bodies. L1 and L5 belong to the spine, captured by X-Ray imaging, on the right. L1 and L5 are visualized using  $\mu$ CT. L1 is presented by a cut half-way through the vertebra in 3D. L5 is presented by a cut half-way through the vertebra in 2D to give a clearer impression of the internal structure. Zooming in on the superior one-third of L5 (bottom-left) reveals the angle ( $\theta$ ) between the trabecular primary orientation (PTO) and the normal to the endplate's (NE) averaged surface (dotted line). In this example, all trabecular primary directions were oriented posteriorly with respect to the  $NE_{macro}$ . It is relevant here to notice for Part II the coordinate system, which is defined by ImageJ.

convergence is shown in Appendix A. Note that orientations of individual trabeculae vary throughout a  $VOI^{103}$ . Thus, a  $PTO_{macro}$  quantified with the fabric eigenvectors, based on an entire VOI, represents the average primary principal direction of the trabecular structure.



The  $NE_{macro}$  was quantified using the Moments of Inertia plugin in BoneJ. This plugin calculates the moments of inertia around the principal axes of an object, in this case the endplate. Note that only the principal axes of the endplates, which are actually an accessory to the Moments of Inertia function, were analysed. The eigenvectors representing the principal directions of the endplates were given in a similar form as the basis matrix of fabric. The smallest principal direction corresponded to the endplate normal. Thus, the NE was visualized by the eigenvector corresponding to the maximum eigenvalue of the moments of inertia.

$PTO_{macro}$  of a superior or inferior one-third was compared with the NE of the corresponding endplate. The orientation of  $PTO_{macro}$  relative to the  $NE_{macro}$  could be visually assessed by overlapping their origins. Since the  $PTO_{macro}$  and  $NE_{macro}$  were calculated in the same coordinate system, coordinate transformation of the directions was not necessary for comparison. Since shear is only considered in the sagittal plane in this study, its influence on trabecular bone is evaluated in one plane. Therefore, the  $PTO_{macro}$ - $NE_{macro}$  deviations ( $\theta$ ) in this paper are calculated in the two dimensions of the sagittal plane. Figure 6 presents an example of the visualization of  $\theta$  for one spine. The PTO- and NE-vectors were visualized based on their coordinates using a simple Python-code.

### 3.2 Shear dependent adaptation model

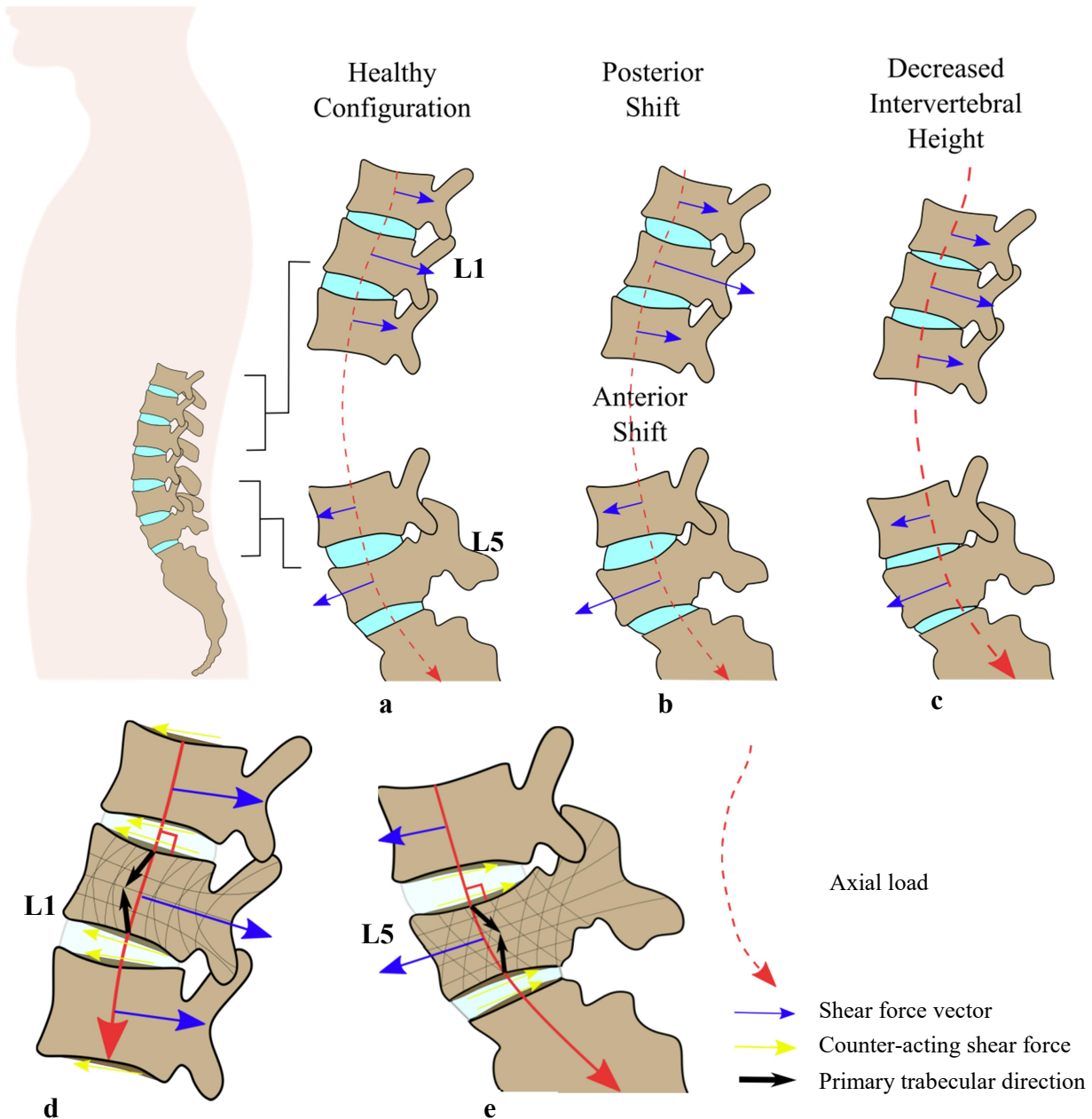
It was assumed that the configuration of the vertebrae provided sufficient information to assess the vertebral mechanical environment in terms of the axial and shear loading directions they were subjected to in the sagittal plane, as shown in Figure 7. The mechanical environment of the vertebral bodies was described in the following manner.

The axial force component throughout the spine was assumed to exactly follow the spine curvature. Therefore, the compression force at each vertebra aligned with  $NE_{macro}$  (Figure 7d and e).

The direction of the shear depended on the vertebral orientations, where L1 and L5 of a healthy spine have their anterior sides inclined in the cranial and caudal directions, respectively (Figure 2a). As a result, L1 and L5 are subjected to posterior and anterior directed forces, respectively<sup>26</sup>, in this study referred to as the shear loading components. At the endplates, counter-acting shear forces appear in the opposite direction to the shear loading components to reassure mechanical equilibrium<sup>104</sup>. The magnitude of the counter-acting shear forces at the endplate is equal to the difference between the shear loading component of one vertebra and its neighbour. Note that these vector magnitudes are not drawn accordingly in Figure 7d and e in order to maintain good visibility for the reader. It is proposed in the model that if shear indeed influences trabecular orientation adaptation, the trajectories reorient to slightly deviate from  $NE_{macro}$ , thus from the axial compression line, equivalent to the magnitude and direction of the counter-acting shear forces at the endplates. Since the shear stress at the endplates of L5 is posteriorly oriented, the  $PTOs_{macro}$  move away from the endplate normal accordingly (Figure 7d). For L1, a force component points to the posterior direction, therefore leading to a counter-acting shear at the endplate surfaces in the opposite direction. Trabeculae deviate slightly towards the anterior direction. Since Smit et al.<sup>99</sup> found that trabeculae tend to grow to the load bearing pedicles of vertebrae and thereby form a fan-shaped structure, the trabeculae in this model do so as well. Figure 7d and e show how the structure should look like under the influence of shear in the sagittal plane. Note that deviations of the  $PTO_{macro}$  with respect to the  $NE_{macro}$  are exaggerated in this figure to make the deviation visible.

An anterior shift, which is more likely to occur at L5 than at L1, or a posterior shift, which is more likely to occur at L1 than at L5, leads to a larger shear force component on the vertebra in the shift direction (Figure 7b). Following the shear adaptation theory, such a shift should lead to larger  $PTO_{macro}$ - $NE_{macro}$  deviations.

A decreased height of the intervertebral discs was associated with an increase in axial directed loading (Figure 7c)<sup>105,106</sup>. In this case, the trabecular structure is thus more dominantly subjected to the axial loading, causing the trabeculae to deviate less from  $NE_{macro}$ .



**Figure 7:** Loading components in the human spine following the shear dependent adaptation model. **a** The spine in healthy configuration. The shear load components are largest at L1 and L5 since they are most inclined. The adjacent vertebrae are more horizontal, leading to smaller shear load components. To create equilibrium, shear stresses at the endplate surfaces should be oppositely directed relative to the shear loading components. The shear stresses should have a magnitude equal to the difference between the shear load components of L1 or L5 and their respective neighbors. **b** The spine containing an anterior shift at L5 and a posterior shift at L1, causing increased load shear loading components. **c** The spine with decreased intervertebral disc heights, which is a sign of an increased axial load (larger arrow). **d** The anteriorly directed counter-acting shear components at L1 lead to an adaptation of trabeculae in a similar direction near the endplates with respect to the endplate normal or axial loading component. **e** For L5, trabeculae are oriented posterior to the axial loading component to maintain mechanical integrity of the vertebra. In both L1 and L5 the trabeculae ultimately are directed towards the pedicles, to support these load bearing regions.

### 3.3 Data analysis

#### 3.3.1 Quantitative analysis

L1 and L5 were compared based on their structural parameters (BV/TV, Tb. Th, Tb. Sp, DA and  $\theta$ ). The superior and inferior VOIs of each vertebra were additionally compared based on these measurements. Differences between L1 and L5 and between the superior and inferior VOIs of each parameter were tested on their significance ( $p < 0.05$ ).

The deviation angle ( $\theta$ ) and orientation (anterior or posterior) of  $PTOs_{macro}$  with respect to  $NEs_{macro}$  were related to the predicted mechanical environment of each VOI based on the vertebral configurations as presented in Figure 7. It was assumed that the larger the deviation, the larger the influence of shear. The  $PTO_{macro}$  considered to align with the  $NE_{macro}$  if  $\theta < 0.5^\circ$ .

#### 3.3.2 Qualitative analysis

The orientation of  $PTOs_{macro}$  relative to the corresponding  $NEs_{macro}$  were analysed on their agreement with the proposed shear dependent adaptation model (Figure 7d and e).

# 4 Results

## 4.1 Vertebral configurations

X-ray images of the spines and  $\mu$ CT images of the vertebrae in the sagittal plane are listed in Appendix C. S1L1, S1L5, S2L1 and S2L5 showed no anterior or posterior shift with respect to their neighbouring vertebrae. The intervertebral discs showed a relatively healthy height (larger intervertebral heights than most of the other studied spines<sup>107</sup>), thus the vertebrae could be classified as having a healthy configuration (Figure 7a). S2L1 showed a degenerated superior endplate. S3L1 had a healthy configuration. S3L5 aligned with the spine curvature and showed healthy intervertebral height, apart from the posterior part of the intervertebral disc, which was relatively thin. S4L1 was in posterior shift and showed a deformed superior endplate in the anterior region, leading to a decreased vertebral height in this area. S4L5 aligned with the spine curvature. The intervertebral discs superior and inferior of S4L5 had a lower height. The inferior-posterior region of S5L1 was posteriorly positioned with respect to S5L2, leading to a counter clockwise-inclination of the vertebra with respect to the spine curvature. The superior endplate was deformed. S5L5 showed a healthy configuration. The intervertebral discs superior and inferior to S6L1 had a lower height. The superior endplate of L1 was deformed. The intervertebral discs superior and inferior to S6L5 were of healthy height. The inferior-posterior region of L4 was posteriorly positioned with respect to L5, causing a counter-clockwise inclination of L5 with respect to the spine curvature. Additionally, the vertebral body aligned more with L1 than with L4.

## 4.2 Structural parameters

L1 and L5 differed in terms of their structural indices on average (Table 1), although insignificantly ( $p>0.05$ ). The same was true for the difference in structural indices between the inferior and superior ROIs of the vertebral bodies (Figure 8).

The PTO-NE deviation differed the most between the two vertebral orientations (29% larger for L5 than for L1) of all parameters. From the same orientation perspective, Tb. Th differed the least (1.4% larger for L5 than for L1) of all structural indices. Regarding the comparison between the superior and inferior VOIs within the vertebrae, the BV/TV differed the most (15% and 18% increase for the inferior with respect to the superior ROI of L1 and L5 on average, respectively) and the DA (0.18% and 3.5% larger for the superior ROI than for the inferior ROI of L1 and of L5 on average, respectively) differed the least of all.

The parameters per ROI per vertebral body are listed in Appendix B. **Structural indices.**

Vertebra	BV/TV (-)	Tb. Th. (mm)	Tb. Sp. (mm)	DA (-)	$ \theta (^{\circ})$
L1	$0.126 \pm 0.037$	$0.343 \pm 0.035$	$1.151 \pm 0.113$	$0.561 \pm 0.085$	$5.444 \pm 3.484$
L5	$0.135 \pm 0.049$	$0.348 \pm 0.033$	$1.169 \pm 0.206$	$0.607 \pm 0.089$	$7.028 \pm 5.087$

Values are mean  $\pm$  SD.

BV/TV = bone volume fraction; Tb. Th. = trabecular thickness; Tb. Sp. = trabecular spacing; DA = degree of architectural anisotropy

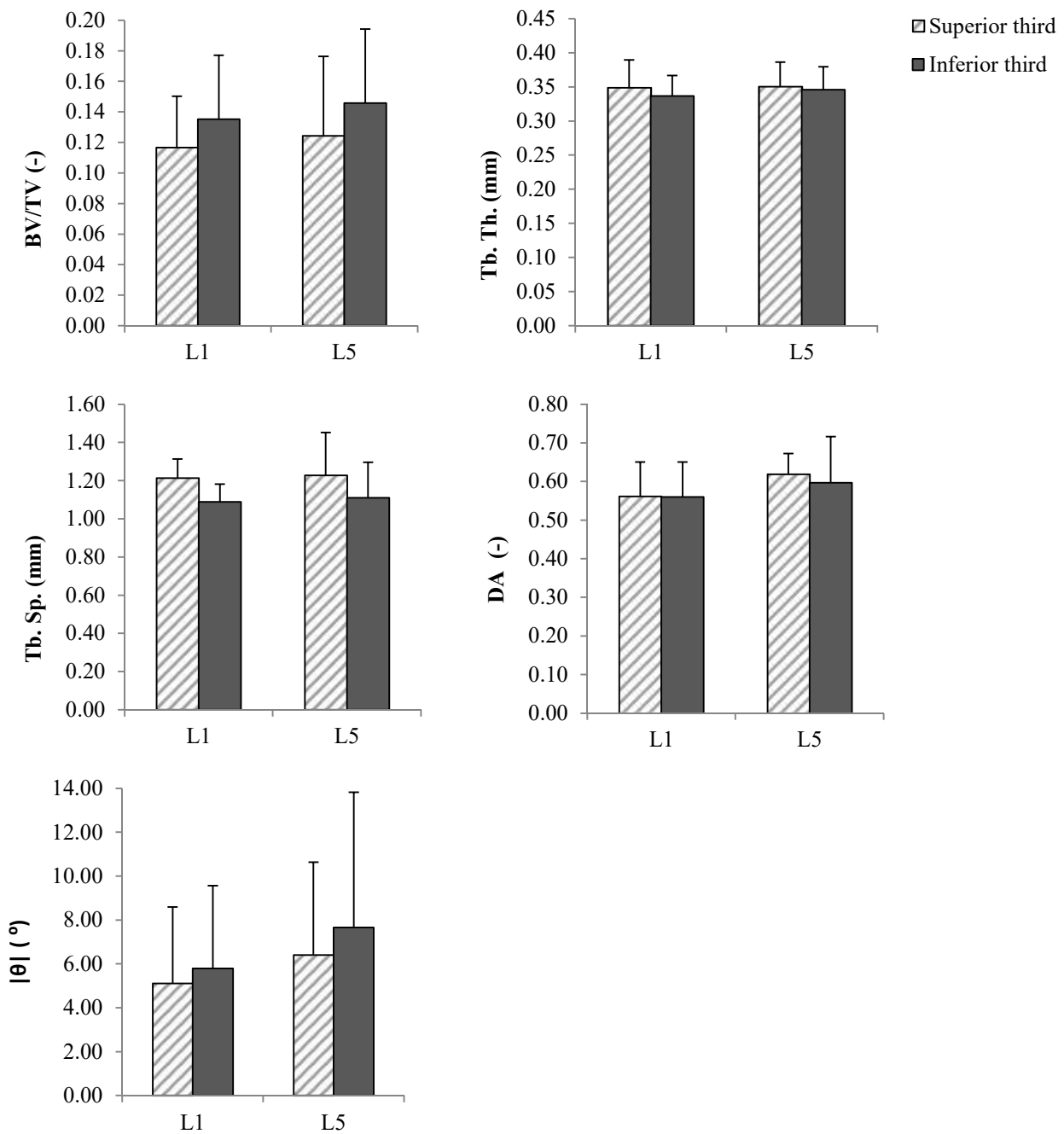
**Table 1:** The means of each structural parameter for L1 and L5 without taking into account differences between superior and inferior one-thirds.

### 4.3 Primary trabecular orientations

PTO<sub>macro</sub>-NE<sub>macro</sub> deviations of S1L1<sub>sup</sub> and S1L1<sub>inf</sub> were 0.883° and 7.19°, respectively, and 7.80° and 4.15° for S1L5<sub>sup</sub> and S1L5<sub>inf</sub>, respectively. S1L1<sub>sup</sub>, S1L1<sub>inf</sub>, S1L5<sub>sup</sub> and S1L5<sub>inf</sub> all showed posterior oriented PTO<sub>macro</sub> with respect to NE<sub>macro</sub>.

PTOs of S2L1<sub>sup</sub> and S2L1<sub>inf</sub> deviated 3.11° in the posterior and 1.44° in the anterior direction for the superior and inferior regions, respectively, and 0.526° and 1.78° in the posterior direction for both of the respective VOIs of S2L5.

For S3L1<sub>sup</sub> of spine 3, the PTO<sub>macro</sub> aligned with the NE<sub>macro</sub>, since the deviation was 0.474° (< 0.5°). The PTO<sub>macro</sub>-NE<sub>macro</sub> deviation of S3L1<sub>inf</sub> was 1.98° with an anterior relative orientation of PTO<sub>macro</sub>. S3L5<sub>sup</sub> showed an anterior deviation of 2.02° of the PTO<sub>macro</sub> with respect to NE<sub>macro</sub>. A posterior deviation of 8.66°



**Figure 8:** A graphical outline of the comparisons of each structural parameter between the superior and inferior one thirds and between the L1's and L5's.

of the  $PTO_{macro}$  with respect to  $NE_{macro}$  was found for  $S3L5_{inf}$ .

$S4L1_{sup}$   $PTO_{macro}$  was anteriorly oriented with respect to  $NE_{macro}$  with a deviation of  $17.32^\circ$ , whereas the  $S4L1_{inf}$   $PTO_{macro}$  aligned with the  $NE_{macro}$  ( $\theta = 0.282^\circ$ ). The  $S4L5$  showed an anteriorly oriented PTO for the superior VOI of  $1.34^\circ$  and a posterior oriented PTO for the inferior VOI of  $9.72^\circ$  with respect to their corresponding NE's.

The trabeculae in  $S5L1_{sup}$  showed a general tendency towards the anterior direction having a  $PTO_{macro}-NE_{macro}$  deviation of  $9.12^\circ$ .  $S5L1_{inf}$  showed a posteriorly oriented  $PTO_{macro}$  with respect to the corresponding  $NE_{macro}$  with a deviation of  $13.18^\circ$ .  $PTOs_{macro}$  of  $S5L5$  were posteriorly oriented for both superior and inferior VOIs under an angle of  $3.57^\circ$  and  $7.98^\circ$ , respectively, with respect to their corresponding  $NEs_{macro}$ .

The trabecular structure of  $S6L1$  showed an average anterior orientation of  $3.62^\circ$  and  $2.62^\circ$  for both superior and inferior one-thirds, respectively, relative to their corresponding  $NEs_{macro}$ . As for  $S6L5$ , its superior  $PTO_{macro}$  aligned with the associated  $NE_{macro}$  ( $\theta = 0.255^\circ$ ) and the inferior  $PTO_{macro}$  deviated from its  $NE_{macro}$  in the anterior direction under an angle of  $4.076^\circ$ .

Table 2 presents a summary of the results for each VOI analysed in this study. Three out of twenty-four VOIs, the  $S3L1_{sup}$ ,  $S4L1_{inf}$  and  $S6L5_{sup}$  showed a close alignment between their  $PTO_{macro}$  and  $NE_{macro}$  ( $\theta < 0.5^\circ$ ). Twenty-one out of twenty-four VOIs showed a clear deviation between  $PTO_{macro}$  and  $NE_{macro}$  ( $\theta > 0.5^\circ$ ). Out of these deviations, fourteen, 6 anterior  $PTOs_{macro}$  for L1 and 8 posterior  $PTOs_{macro}$  for L5, were directed in the shear dependent directions as suggested in the shear dependent adaptation model of Figure 7d and e. The measurements related to solid quantities in trabecular bone fell within the range of those reported in the studies by Homminga et al.<sup>3</sup>, Yeni et al.<sup>108</sup> (BV/TV) and Majumdar et al.<sup>109</sup> (Tb. Th. and Tb. Sp.).

Spine	Ver.	Sup/Infer	Config. /comments	$ \theta $ (°)	Direction	Agreement with theory
1	L1	Superior	Healthy	3D: 0.989	Posterior	None
		Inferior		2D: 0.883	Posterior	None
	L5	Superior	Healthy	3D: 7.20	Posterior	None
		Inferior		2D: 7.19	Posterior	Shear dependent theory
				3D: 8.22	Posterior	Shear dependent theory
				2D: 7.80	Posterior	Shear dependent theory
				3D: 4.54 (-)	Posterior	Shear dependent theory
				2D: 4.15 (-)		
2	L1	Superior	Degenerated endplate	3D: 8.00 (-)	Posterior	None
		Inferior	Healthy	2D: 3.11 (-)	Anterior	Shear dependent theory
2	L5	Superior	Healthy	3D: 1.49 (-)	Anterior	Shear dependent theory
		Inferior		2D: 1.44 (-)	Posterior	Shear dependent theory
				3D: 3.50	Posterior	Shear dependent theory
				2D: 0.526	Posterior	Shear dependent theory
				3D: 2.15 (-)	Posterior	Shear dependent theory
				2D: 1.78 (-)		
3	L1	Superior	Healthy	3D: 6.95 (-)	Alignment	Trajectorial theory
		Inferior		2D: 0.474 (-)	Anterior	Shear dependent theory
3	L5	Superior	Healthy	3D: 2.07	Anterior	Shear dependent theory
		Inferior		2D: 1.98	Anterior	None
				3D: 4.74	Anterior	None
				2D: 2.02	Posterior	Shear dependent theory
				3D: 9.30 (-)	Posterior	Shear dependent theory
				2D: 8.66 (-)		
4	L1	Superior	Deformed endplate	3D: 19.07	Anterior	Shear dependent theory
		Inferior	Posterior shift	2D: 17.32	Alignment	Trajectorial theory
4	L5	Superior	Decreased intervert. height	3D: 1.96	Alignment	Trajectorial theory
		Inferior		2D: 0.282	Anterior	None
				3D: 7.24 (-)	Anterior	None
				2D: 1.34 (-)	Posterior	Shear dependent theory
				3D: 11.57	Posterior	Shear dependent theory
				2D: 9.72		
5	L1	Superior	Counter-clockwise rotation and deformed endplates	3D: 10.20 (-)	Anterior	Shear dependent theory
		Inferior		2D: 9.12 (-)	Posterior	None
5	L5	Superior	Healthy	3D: 13.53 (-)	Posterior	None
		Inferior		2D: 13.18 (-)	Posterior	Shear dependent theory
				3D: 4.18	Posterior	Shear dependent theory
				2D: 3.57	Posterior	Shear dependent theory
				3D: 7.97	Posterior	Shear dependent theory
				2D: 7.98		
6	L1	Superior	Decreased intervert. height	3D: 5.15 (-)	Anterior	Shear dependent theory
		Inferior		2D: 3.62 (-)	Anterior	Shear dependent theory
6	L5	Superior	Counter-clockwise rotation	3D: 2.96	Anterior	Shear dependent theory
		Inferior		2D: 2.62	Alignment	Trajectorial theory
				3D: 2.53	Alignment	Trajectorial theory
				2D: 0.255	Anterior	None
				3D: 4.15	Anterior	None
				2D: 4.08		

**Table 2:** Overview of the agreement of the combination of vertebral configuration, PTO-NE deviations ( $\theta$ ) and the relative PTO orientation with one of the trabecular trajectory adaptation models.

# 5 Discussion

This part presents, to our knowledge, the first analysis on trabecular bone orientation in vertebrae in relation to mechanics depending on the vertebral configuration. Sensitivity of bone adaptation to loading patterns different from the axial force component throughout the spine, such as shear, was successfully addressed based on the number of strongly deviating averaged trabecular trajectories with respect to the NEs (21 out of 24). Still, all  $PTO_{macro}$  deviated much less with respect to the axial loading component than to the shear force component. That all  $PTO_{macro}$  preferably aligned with the axial loading component, supports Wolff's law from the perspective that trabecular bone orients predominantly to the compression line.

Regarding bone quantity measurements, the related structural indices did not differ significantly between VOIs and vertebral bodies. However, there was a large variation of the indices between VOIs, especially of BV/TV. Standard deviations pointed out that the BV/TV of the  $L1_{sup}$  and  $L1_{inf}$  varied  $\pm 29\%$  and  $\pm 31\%$  with respect to the averages, respectively, and the BV/TV of the  $L5_{sup}$  and  $L5_{inf}$  varied  $\pm 42\%$  and  $\pm 34\%$  with respect to the averages, respectively. As this parameter is an indicator for trabecular porosity and vertebrae were mainly retrieved from elderly, their variance most likely indicate that the specimens included osteoporotic vertebrae. This variance could have an effect on the DA and PTO, since studies have shown that an osteoporotic trabecular structure leads to a stronger apposition of bone in the PTO than the secondary and tertiary trabecular orientations and a stronger alignment of the PTO with the compression line<sup>3</sup>. This study is in line with the latter finding since the VOIs containing the smallest BV/TV showed a relatively close alignment of  $PTO_{macro}$  with the  $NE_{macro}$ , thus with the compression line. In fact, three of those  $PTO_{macro}$  were the ones deviating less than  $0.5^\circ$  from the  $NE_{macro}$ , in this study considered to be completely in line with the trajectorial theory of Wolff.

In this study it was reasoned that when an anterior or posterior shift was present, there should be a larger PTO-NE deviation due to the increased shear at the endplates. The only vertebra where a clear shift was seen, was spine 4 L1, in the posterior direction. The resulting deviation of the PTO near the superior endplate was largest of all ( $17.32^\circ$ ), supporting the model of shear dependent trabecular orientation. It should be noted that the large deviation could also be due to a locally increased compressive load in the anterior region. Namely, the superior endplate was deformed as if it were indented by T12 at its anterior part. As a result, trabeculae might be directed towards the corresponding region to support the vertebra mechanically<sup>110</sup>, on average creating a strong preferential orientation in the anterior direction. Moreover, the next largest deviation was seen in spine 5 L1, where also deformed endplates were seen, likely the result of locally pressurizing adjacent vertebrae onto the anterior superior and posterior inferior endplate regions, causing a counterclockwise rotation with respect to the spine curvature as specified in Table 2. The deformations were visible at the anterior and posterior regions of the superior and inferior endplates, respectively. Similar to spine 4 L1, trabecular trajectories were oriented towards the deformed regions, so a strong anterior ( $9.12^\circ$ ) and posterior ( $13.18^\circ$ ) directed deviation for the PTOs of the superior and inferior VOI.

As for the argument that decreased intervertebral heights should indicate a relatively close PTO-NE alignment, this logic was not supported by the results. The vertebral bodies in between decreased intervertebral heights showed  $PTO_{macro}$ - $NE_{macro}$  deviations of  $1.34^\circ$  and  $9.72^\circ$  ( $S4L5_{sup}$  and  $S4L5_{inf}$ , respectively) and  $3.62^\circ$  and  $2.62^\circ$  ( $S6L1_{sup}$  and  $S6L1_{inf}$ , respectively). Although three of those were well below the average ( $6.236^\circ$ ), the deviation for  $S4L5_{inf}$  was relatively large. This study thereby does not



support the idea, that trabeculae nearby decreased intervertebral disc heights align more strongly with the axial force vector as a consequence of increased compression<sup>105</sup>.

However, as a response to the other  $PTOs_{macro}$  that did not fit one of the proposed theories as well (Table 2), loading patterns mapped in three dimensions may reveal explanations of unexpected results. Torsion in the spine could play a role in amplifying or overruling the shear in the sagittal plane. For example, scoliosis has been associated with increased torsions in the spine. As a consequence, trabeculae could align more dominantly to the shear stresses caused by torsion, rather than the shear stresses in the sagittal plane as suggested here. When comparing the 3D- to the 2D-deviation angles in Table 2, large differences can be seen, implying the influence of forces in the z-dimension additional to the loadings in the x-y-plane (Figure 7) as focused on in this study.

Therefore, future research should include analysis of the three-dimensional configuration of vertebral bodies to describe their mechanical environments. Using mathematical models of the vertebral configurations, could aid in understanding the biomechanical situation of the vertebra<sup>111</sup>.

In addition, trabecular bone adaptation simulations or in vivo time-lapsed  $\mu$ CT images, where shear forces are applied to the specimen, should be analysed on changes in primary trabecular orientations over time to better quantify the influence of shear with respect to compression and tension on bone adaptation.

Moreover, to get an estimation of the overall tendency of trabeculae to adapt to shear stresses near the endplates, the entire superior and inferior one-thirds were chosen as VOI in this study. However, the trabecular orientation varies within these VOIs along the posterior-anterior direction. A more complete view of regional differences of the trabecular orientation and the role of shear in vertebral trabecular bone adaptation would be obtained if the VOIs would also be divided in an anterior, medial and posterior segment.

# 6 Conclusion

In short, trabecular trajectories predominantly adapt to compression in the spine. Still, the trabecular primary orientation deviated strongly with respect to the dominant, vertical force component acting on the vertebral endplates, being  $6.24^\circ(\pm 4.34^\circ)$  on average. This suggests that shear forces are of substantial influence on the constitution of the primary trabecular orientation in vertebrae. The impact of shear on trabecular remodeling should be further investigated and be taken into account in future studies to investigate bone adaptation with potential applications in the improvement of orthopaedic implants and biomaterials.

## Part II

# The Relation between the Preferred Trabecular Orientation and Elasticity on the Vertebral Trabecular Micro-Tissue Level

# 7 Background

## 7.1 Elasticity in trabecular bone

The mechanical character of trabecular bone can be effectively described by defining its elastic properties. From the elasticity, it is possible for biomedical engineers to assess stiffness magnitudes, mechanical anisotropy<sup>29</sup> and orientations of the structures in which they are stiffest and least stiff<sup>12</sup>.

These aspects of elasticity can be directly or indirectly drawn from the elasticity tensor. The elasticity relates the stress to the strain of a material by

$$\boldsymbol{\sigma} = \mathbf{C} \boldsymbol{\varepsilon} \quad (9)$$

where  $\boldsymbol{\sigma}$  and  $\boldsymbol{\varepsilon}$  are the second order stress and strain tensors, respectively, and  $\mathbf{C}$  is the fourth order elasticity tensor and in case of Eq. (9) also called the stiffness tensor. The inverse of  $\mathbf{C}$  is called the compliance matrix.

Elasticity is described by the stiffness tensor in this report, thus both terms are used to describe the same physical quantity. For trabecular bone, which is considered to be an orthotropic structure, the stiffness tensor can be depicted by

$$\mathbf{C}^{\text{ORT}} = \begin{bmatrix} c_{11} & c_{12} & c_{13} & 0 & 0 & 0 \\ c_{12} & c_{22} & c_{23} & 0 & 0 & 0 \\ c_{13} & c_{23} & c_{33} & 0 & 0 & 0 \\ 0 & 0 & 0 & c_{44} & 0 & 0 \\ 0 & 0 & 0 & 0 & c_{55} & 0 \\ 0 & 0 & 0 & 0 & 0 & c_{66} \end{bmatrix},$$

showing nine independent components. The components of this matrix firstly indicate how stiff the structure is. The larger the components, the stiffer the material.

Secondly, the material symmetry can be drawn from the ratio between two of the smaller diagonal, or principal, elastic constants that describe the stiffness as a result of the material in compression/tension ( $c_{11}$ ,  $c_{22}$ ,  $c_{33}$ ). For instance, in their investigation of anisotropic elastic properties, Unnikrishnan et al.<sup>29</sup> found that elderly vertebral bodies contain an anisotropic trabecular structure and no transverse isotropy, for which must be true that the ratio between two of the smaller principal stiffness components approximately equals one. They also found that as the bone volume fraction increased (BV/TV), this ratio had a mild tendency to get closer to unity.

## 7.2 Principal directions of elasticity

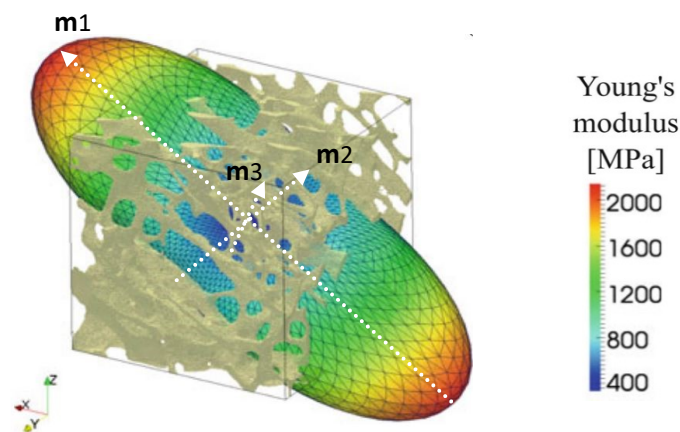
The direction wherein struts of cancellous bone grow, is such that the structure does not fail under the mechanical demands in daily life. Considering that the resistance of a material in structural mechanics to deform as a result of the forces that are exerted on it, presents itself in the form of elasticity, a relation should exist between the latter and trabecular orientation. The relation seems apparent already, taking into account that the directional growth of bone leads to more bone deposition and thus an increased stiffness in certain directions compared to others. The directions of a structure along which there are minima and maxima of stiffness, are called the principal elastic directions. Just like the principal directions of fabric are

derived from the fabric tensor, the principal directions of elasticity can be extracted from the elasticity or stiffness tensor.

Finding the visual approximation of the stiffness tensor is substantially more complicated than of the fabric tensor as a result of its high rank nature. Nevertheless, Gross et al.<sup>112</sup> displayed the stiffness tensor of trabecular bone graphically by visualizing the distribution of the Young's moduli over the structure of interest in colour and geometry. The resulting peanut shaped geometry is presented in Figure 9. Similar to the fabric visualization, principal directions are shown which depict the directions in which there are minima (secondary and tertiary) and maxima (primary) of stiffness.

A thorough understanding of the relation between trabecular orientation and elasticity allows us to understand the mechanical function of directional properties of trabecular bone. Knowing how the desired state of elasticity is constituted from trabecular orientation, may provide specialists in the field of orthopaedics with novel approaches to predict the mechanical quality of bone<sup>13</sup>.

Odgaard et al.<sup>13</sup> found a close relation between directionality of the cancellous structure quantified by fabric and elasticity as a way of expressing trabecular orientation in its mechanical role. From this perspective, trabecular orientation functions as a way to strengthen trabecular bone in terms of stiffness. Namely, elastic principal directions align with the principal stress directions. Thus, when trabeculae are equally oriented to the elastic principal axes, they additionally align with the principal stress directions. Hence, the trabecular structure is in this case oriented to support the skeleton in the directions where the largest (principal) stresses appear. This finding implies that fabric can be used not only to estimate elastic principal directions, but also to predict loading directions in the skeleton's mechanical environment. Odgaard et al.<sup>13</sup> thereby found a new method to predict loading directions in biomechanics of the skeleton. Determining the elastic principal directions combined with the fabric in vertebrae gives a firmer view of the direction which the trabeculae have been adapting to. Fabric and elastic orientations deviating from the axial direction in the spine strongly suggest the influence of alternative directed loadings on the bone adaptation.



**Figure 9:** Graphical representation of an anisotropic elasticity tensor and elastic principal directions of an arbitrary bone cube. m1, m2 and m3 correspond to the primary secondary and tertiary This figure is re-used with permission of the publisher<sup>112</sup>

### 7.3 Trabecular elastic principal directions in vertebrae

A recent study to human vertebral bodies in elderly by Unnikrishnan et al.<sup>29</sup> however, has not shown the close relation between elastic and trabecular principal directions that one would expect from the findings of Odgaard et al.<sup>13</sup> The primary elastic orientation (PEO) aligned much more with the primary fabric orientation ( $5.61^\circ$ ) than the secondary and tertiary elastic orientations did with the secondary and tertiary fabric orientations, respectively ( $20.40^\circ$  and  $23.00^\circ$ ). Still, all deviations were larger than the close alignments found by Odgaard et al.<sup>13</sup> ( $0.55^\circ$ ,  $3.10^\circ$  and  $3.10^\circ$ , respectively). The inaccurate outcomes of the

former study were ascribed to the size of the VOIs (cubes with a side length of 5.0 mm) in combination with a low bone volume fraction. This issue is especially relevant when analysing elderly samples, such as the ones in the current study, as they often exhibit relatively porous trabecular regions.

#### **7.4 Research aim**

Investigating elastic properties per direction of the structures elucidates the mechanical function of trabecular orientation. The goal of the current part is to present elastic properties of trabecular bone within the regions analysed in Part I on a smaller scale, the micro-tissue level (1-10 mm). The motivation for this aim was two-fold:

1. To assess whether the primary elastic orientation was able to predict the primary trabecular orientation on the micro-scale. The extent to which these directions were related should give insights on the quality of the samples and reveal challenges or opportunities in mechanical analysis of elderly vertebrae.
2. To find relations between the elastic and fabric orientations found in Part I and the fabric orientations found in Part II. As the orientations calculated in Part I and II were determined on different scales, relations between the two should show how mechanics and trabecular directions depends on the scale in which they are analysed.

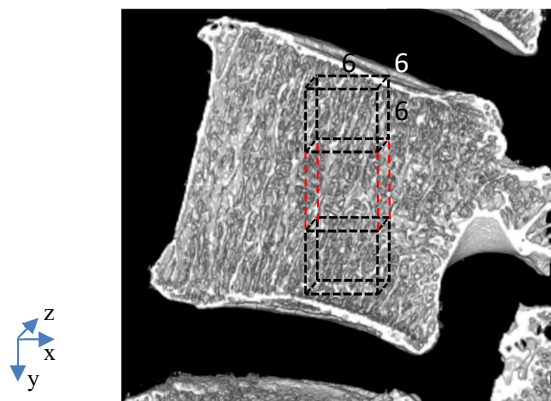
# 8 Methods

The elasticity tensor should be calculated first in order for the PEO to be determined. To calculate the components of the elasticity tensor, finite element (FE) modelling of the VOI was performed. This paragraph describes the selection of VOIs for the FE models in the range of the micro-tissue level (1-10 mm), the FE model specifics, how PEOs on the micro-tissue level ( $PEOs_{micro}$ ) were found from the stiffness tensors and finally how all data was analysed quantitatively and qualitatively.

## 8.1 Segmentation

Firstly, cubic VOIs were selected from the binarized  $\mu$ CT-images constructed in Part I. The FE-models should be representative for the structures analysed in Part I, however on the micro-tissue level. The cubes should therefore fit one-third of the height of a vertebral body maximally, as this was the portion of the vertebral height used for the quantifications in Part I. Since the height between vertebrae is different and the height within a vertebra varies and a constant cube size should be chosen, the VOI size was limited to side lengths of 6.0 mm, which was just less than one-third of the minimum height of the smallest vertebra. Which such side lengths the cubes automatically met the requirement of being within the micro-tissue level (1-10 mm).

The cubes were selected in the superior and inferior centres of the vertebrae with exactly the same x and z coordinates (Figure 10).



**Figure 10:** The superior and inferior cubic VOIs (yellow) of side length 6.0 mm visualized in one of the vertebrae. The red dotted lines show that the VOIs were defined as having the same x- and z-coordinates.

## 8.2 FE simulations

Finding the PEOs involves the calculation of the full anisotropic stiffness tensor using FE modelling. The tensor components were calculated by applying 6 mechanical tests in total, three compressive and three shear tests. One plate was placed on one side of the cube with another one on the opposite side. Displacement of one of the plates with respect to the other resulted in deformation of the trabecular bone. The components of the elasticity matrix could be determined one by one through the constitutive equation, the known (applied) strain and calculated average stress<sup>112</sup> by the FE model.

### 8.2.1 Mesh generation

The commercial software Mimics (V14.01, Materialise, Leuven, Belgium) was used to convert the stacks of VOIs into three dimensional objects. The portion of trabecular bone within the VOIs was selected that formed a continuous structure of interconnected struts. Singularities were thus removed. 11 of 24 cubes had to be excluded from analysis. The remaining of these cubes after choosing the continuous portion of the cube was too small to use for the FE-modelling. This exclusion was based on the initial positions of the plates at all mechanical tests, which should be at a 6.0 mm distance with respect to each other. The regions and vertebral bodies that did not meet this exclusion criterion, are listed in Table 3. Mimics automatically meshed the remaining of the cubes with triangular surface elements. To remove sharp edges, the surface mesh was smoothed. The result was exported as an STL-file to be remeshed in 3-matic (V5.1, Materialise, Leuven, Belgium) for FE-analysis. An element size that should lead to accurate stress values was chosen after a validation model was made. The elements were divided by the minimum factor that would lead to convergence of the stress over the number of elements to minimize computational costs. Abaqus (V16.4) was used as the FE modelling software. According to the validation model, the elements were divided by 2 to obtain sufficient convergence. This validation model is shown in Appendix D. The surface mesh was converted in Abaqus to a volume mesh of linear tetrahedral elements. The resulting number of elements for the trabecular bone structures varied between 133400 – 700900 depending on the relative bone volume (BV/TV). The plates were designed in Abaqus, had a side length of 6.5 mm and were 0.5 mm thick. To prevent problems related to the algorithm for the contact between the plates and the bone structure, the plate elements were larger than the bone elements. The plates counted 3072 linear hexahedral elements each.

Spine	Vertebra	Region
1	L1	Superior Inferior
	L5	Superior Inferior
2	L5	Superior
5	L1	Superior Inferior
	L5	Superior Inferior
6	L1	Superior Inferior
	L5	Superior Inferior

**Table 3:** Cubes from these sample regions were used for analysis.

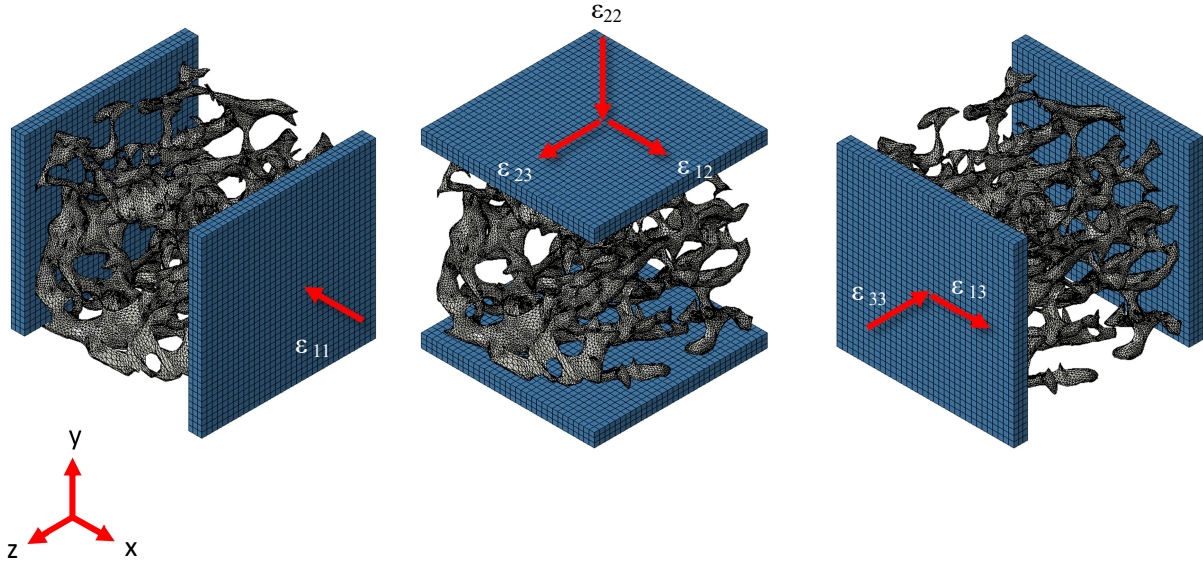
### 8.2.2 Material properties

The bone part of the model was the deformable object and the plate was assumed to be non-deformable, in Abaqus referred to as the slave and master, respectively. The bone structures were assumed to be isotropic and to deform linear elastically. A Young's modulus of 1 GPa<sup>15</sup> was assigned to the elements and the Poisson's ratio was 0.3. The master plates had a Young's modulus of 1x10<sup>3</sup> GPa to ensure negligible deformation of the plates. The Poisson's ratio again was 0.3.

### 8.2.3 Contact

A frictionless surface-surface contact was defined between the plates and the bone. The tolerance adjustment zone was set to 0.06 to make sure that all elements of the slave surface within this region initially were in contact with the master surface without penetrating the master surface. Settings were changed such that the slave surface automatically adapted to the displacement of the plate so that no





**Figure 11:** A FE-model of one of the trabecular cubes. The strains corresponding to the applied plate displacements of the six mechanical tests are shown. Note that the strains 11-, 22-, 33-, 23-, 13-, 12-directions corresponded to x-, y-, z-, yz-, xz- and xy-displacements in the given coordinate system (bottom-left), respectively.

penetration during the step took place. Adjusted slave surfaces during simulation were tied to the master to ensure displacement of the bone in one direction at the surface.

#### 8.2.4 Steps

One static, general step was defined. An algorithm (NLgeom) provided by Abaqus was applied, which functions to let the simulation take nonlinear effects of the complex structure geometries into account during analysis of the deformation.

#### 8.2.5 Boundary conditions

One moving plate was assigned a non-zero Dirichlet boundary condition of a displacement corresponding to a strain of 0.016 for all mechanical tests. If a compression in the 11-direction was applied, the corresponding displacement  $\delta$  could simply be calculated by solving

$$\varepsilon_{11} = \frac{\delta}{L_1}, \quad (10)$$

where  $\varepsilon_{11}$  was the strain in the 11-(x-) direction and  $L_1$  was the original side-length of the cube, considering that the material was assumed to behave linear elastically. The oppositely placed plate was assigned a zero Dirichlet boundary condition, preventing any movement of this plate. Displacements in the other directions were prevented by additionally tying the plates to the bone. An overview of the FE-models and the applied boundary conditions is shown in Figure 11.

#### 8.2.6 Field Output Request

Stresses in all directions were requested as output of the simulation since the averages were used to solve the constitutive equation. Contact forces were requested and checked after each simulation to verify that contact algorithms actually worked.

### 8.3 Elasticity parameters

Finding the components of the full anisotropic elasticity tensor involved solving the constitutive equation at each mechanical test. Displacements in the directions other than the one in which the movable plate was translated were prevented. All strains could therefore be set to zero, except the one corresponding to the translation, such that  $\boldsymbol{\varepsilon} = [\varepsilon_{11} \ 0 \ 0 \ 0 \ 0 \ 0]^T$  if there is a compression in the 11-direction. The first component  $c_{11}$  could therefore be calculated by dividing the average stress value  $\sigma_{11}$  by the compressive strain  $\varepsilon_{11}$  by  $c_{11} = \sigma_{11}/\varepsilon_{11}$ <sup>113</sup>. The other elasticity components of the first column (green vertical rectangle) were calculated based on this strain and stresses calculated by the FE-simulation in the other directions. Since the stiffness matrix can be assumed to be symmetric<sup>114</sup>, the symmetric counterpart of the first column (green dashed horizontal rectangle) could be filled as well

$$\begin{bmatrix} \sigma_{11} \\ \sigma_{22} \\ \sigma_{33} \\ \sigma_{23} \\ \sigma_{13} \\ \sigma_{12} \end{bmatrix} = \begin{bmatrix} c_{11} & c_{12} & c_{13} & c_{14} & c_{15} & c_{16} \\ c_{12} & c_{22} & c_{23} & c_{24} & c_{25} & c_{26} \\ c_{13} & c_{23} & c_{33} & c_{34} & c_{35} & c_{36} \\ c_{14} & c_{24} & c_{34} & c_{44} & c_{45} & c_{46} \\ c_{15} & c_{25} & c_{35} & c_{45} & c_{55} & c_{56} \\ c_{16} & c_{26} & c_{36} & c_{46} & c_{56} & c_{66} \end{bmatrix} \begin{bmatrix} \varepsilon_{11} \\ 0 \\ 0 \\ 0 \\ 0 \\ 0 \end{bmatrix}$$

Applying compression in the 22-direction lead to the elasticity components of the second column and row

$$\begin{bmatrix} \sigma_{11} \\ \sigma_{22} \\ \sigma_{33} \\ \sigma_{23} \\ \sigma_{13} \\ \sigma_{12} \end{bmatrix} = \begin{bmatrix} c_{11} & c_{12} & c_{13} & c_{14} & c_{15} & c_{16} \\ c_{12} & c_{22} & c_{23} & c_{24} & c_{25} & c_{26} \\ c_{13} & c_{23} & c_{33} & c_{34} & c_{35} & c_{36} \\ c_{14} & c_{24} & c_{34} & c_{44} & c_{45} & c_{46} \\ c_{15} & c_{25} & c_{35} & c_{45} & c_{55} & c_{56} \\ c_{16} & c_{26} & c_{36} & c_{46} & c_{56} & c_{66} \end{bmatrix} \begin{bmatrix} 0 \\ \varepsilon_{22} \\ 0 \\ 0 \\ 0 \\ 0 \end{bmatrix}$$

All columns in the elasticity matrix were filled in this way according to the six mechanical tests.

#### 8.3.1 The direct mechanics method

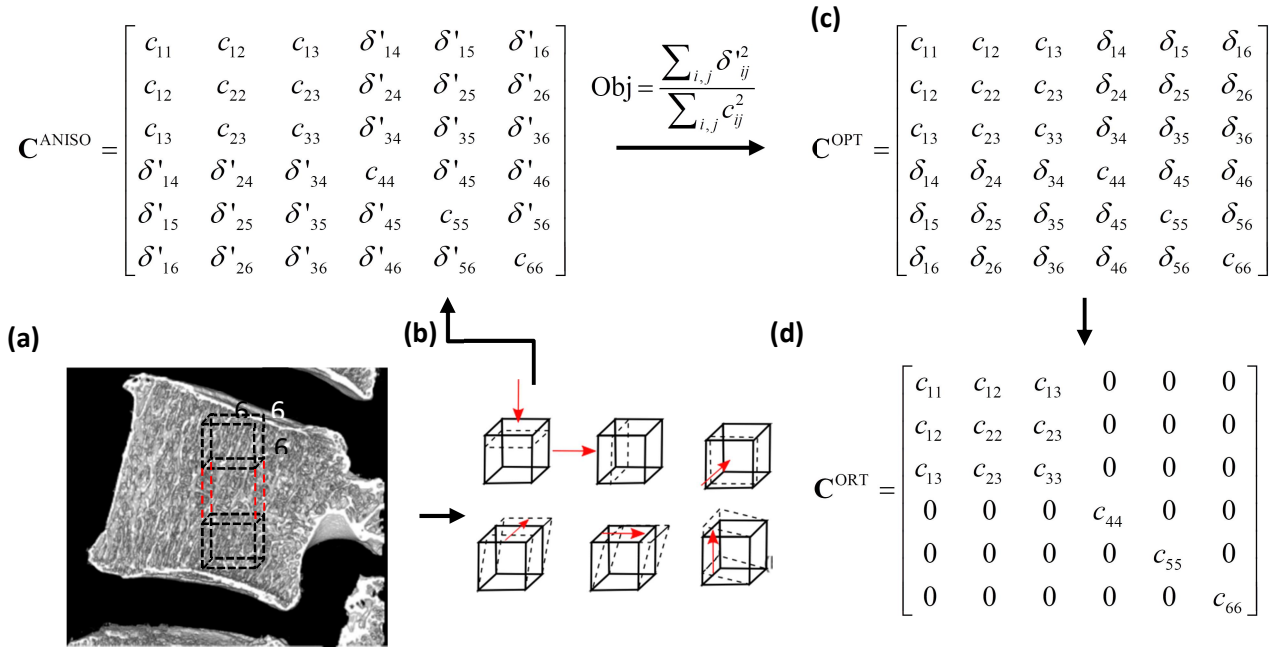
The PEOs were calculated via the transformation matrix that converted the full anisotropic stiffness tensor  $\mathbf{C}^{ANISO}$  in its most orthotropic representation  $\mathbf{C}^{OPT}$ . This method of calculating the PEOs of a structure is called the direct mechanics method<sup>12,29</sup>. An objective function was used to minimize the components of  $\mathbf{C}^{ANISO}$  that should be zero in order for the stiffness tensor to depict orthotropy. The objective function was

$$Obj = \frac{\sum_{i,j} \delta'_{ij}}{\sum_{i,j} c_{ij}^2}, \quad (11)$$

where  $\delta'_{ij}$  were the stiffness components which were minimized and  $c_{ij}$  all other stiffness components. The coordinates of the PEOs were derived from the columns of the transformation matrix that related  $\mathbf{C}^{ANISO}$  to  $\mathbf{C}^{OPT}$

$$\mathbf{C}_{ijkl}^{ANISO} = \mathbf{R}_{i\alpha} \mathbf{R}_{j\beta} \mathbf{R}_{k\gamma} \mathbf{R}_{l\delta} \mathbf{C}_{\alpha\beta\gamma\delta}^{OPT}, \quad (12)$$

where  $\mathbf{R}$  is a second order tensor that rotates the stiffness tensor until its most orthotropic representation is found.  $\mathbf{R}$  is given in the form of



**Figure 12:** The steps required to get the orthotropic stiffness tensor using FEM. **a** Cubes of trabecular bone are extracted from a 3D  $\mu$ CT image of a vertebral body. **b** Six different displacements are applied to each cube delivers the full anisotropic stiffness matrix. **c** The optimized stiffness matrix is obtained by applying an algorithm involving the coordinate transformation of  $\mathbf{C}^{\text{ANISO}}$  to the fabric coordinate system. **d** At last, residual stiffness components are set to zero, leaving the orthotropic stiffness tensor.<sup>29</sup>

$$\mathbf{R} = \begin{bmatrix} \cos \alpha \cos \chi + \sin \alpha \sin \beta \sin \chi & \sin \alpha \cos \beta & -\cos \alpha \sin \chi + \sin \alpha \sin \beta \cos \chi \\ -\sin \alpha \cos \chi + \cos \alpha \sin \beta \sin \chi & \cos \alpha \cos \beta & \sin \alpha \sin \chi + \cos \alpha \sin \beta \cos \chi \\ \cos \beta \sin \chi & -\sin \beta & \cos \beta \cos \chi \end{bmatrix},$$

where  $\alpha$ ,  $\beta$  and  $\chi$  are the angles of rotation around the z-, x- and y-axis, respectively. Following van Rietbergen et al.<sup>12</sup>, the columns of  $\mathbf{R}$  are equivalent to the orthonormal basis and thus principal directions of the orthotropic stiffness tensor. For an overview, the steps to calculate the PEOs are schematically summarized in Figure 12.

## 8.4 Data analysis

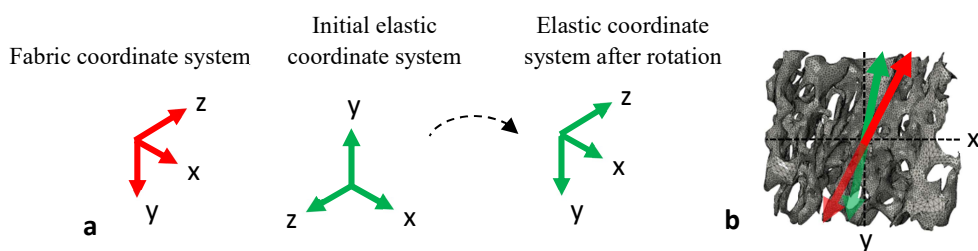
Firstly, the principal components  $c_{ii}$  (diagonal) of the orthotropic representation of the elasticity tensor were evaluated by means of their median, minimum and maximum. By presenting these values, the results are comparable to an earlier study<sup>29</sup> to elasticity of vertebral trabecular bone, which will be elaborated in section 10 (Discussion). These elastic constants gave an impression which mechanical test gave the largest stresses, thus along which coordinate axis stiffness was dominant. For the sake of clarity, the components  $c_{11}$ ,  $c_{22}$  and  $c_{33}$  were the stiffness constants relating stresses and strains in compressions along the x-, y- and z-axes, respectively, and components  $c_{32}$ ,  $c_{13}$  and  $c_{12}$  related the shear stresses and strains in the zy-, xz- and xy-directions, respectively (Figure 11). Additionally, ratios between the principal compressive stiffness constants were calculated, as well as their relation to the bone volume fraction were not reported since the sample size ( $n = 13$ ) and correlation coefficient ( $R^2 = 0.18$ ) were too small.

Next, the PTOs were determined based on the fabric principal directions, just as in Part I, only now applied to the cubic VOIs, representative for the micro-tissue level. The measurements of the  $PTO_{micro}$  were again validated by checking the convergence of the DA calculation, as was elaborated in Part I. The solution converged successfully (Appendix A.). The  $PEO_{micro}$  was read from the column of the rotation matrix representing the longest, thus dominant, principal axis. This column corresponded to the column with coordinates closest to the dominant fabric eigenvector.

All  $PTO_{micro}$  and  $PEO_{micro}$  were visualized in one coordinate system in the x-y plane, equivalent to the sagittal plane in the spine. Viewing the vectors from this perspective was convenient for relating findings on the micro-tissue level to those on the macro level (Part I), where PTO-analysis was also done in the sagittal plane. Furthermore, the coordinate system of the  $PEO_{micro}$  was rotated to coincide with that of the  $PTO_{micro}$ , since the  $PTO_{micro}$  and  $PEO_{micro}$  initially existed in their own coordinate systems. Both coordinate systems and the rotation necessary for the correspondence in coordinate systems is shown in Figure 13. After system rotation was applied, a comparison between the  $PEO_{micro}$  and  $PTO_{micro}$  could be made. First the vectors were visualized, where the centre of the trabecular structures was considered as the point of origin. In words, the visualization was described with respect to this origin in the superior half of the structure. Laterally, the vectors were described as being oriented left and right for pointing in the negative and positive z-direction, respectively.

Deviations between the  $PEO_{micro}$  and  $PTO_{micro}$  were finally calculated in the three-dimensional angle (degrees). They were summarized by means of a box-plot, such that the variation in deviations could be easily assessed<sup>29</sup>. Small deviations and a small variation implied accurate determination of the  $PEO_{micro}$  for the used bone samples and/or methodology. Large deviations and a large variation indicated that the  $PEO_{micro}$  were inaccurate following the samples and approach used in this study.

Finally, the directional properties calculated on the micro-tissue level were compared to those on the macro level (Part I). An attempt was made to describe the impact of spine biomechanics on the macro scale (>10 mm) to trabecular structures on the micro-tissue level (1-10 mm) in this way. The  $PEO_{micro}$  and  $PTO_{micro}$  were related to the axial loading direction, determined by the  $NEs_{macro}$  of adjacent endplates (Part I). Their direction with respect to the  $NEs_{macro}$  were qualitatively determined, in terms of anterior or posterior tendency in the sagittal plane. The outcome thereof was compared to the tendencies of the  $PTO_{macro}$  (Part I) with respect to the  $NEs_{macro}$ . In addition, the  $PTO_{micro}$  and  $PTO_{macro}$  were quantitatively compared by calculating their alignment in the sagittal plane (2D). The idea behind this analysis was to determine whether the  $PTO_{micro}$  could well predict the  $PTO_{macro}$ .



**Figure 13:** **a** The coordinate system of the PTOs and PEOs in red and green, respectively. The coordinate system of the PEO had its z-axis originally opposite directed with respect to the z-axis of the coordinate system of the PTO. Rotation of the PEO coordinate system to coincide with that of the PTO therefore required the y- and z-coordinate of the PEO vector to be multiplied with -1. The vectors were in 2D visualized in the resulting coordinate system. **b** The centre of the cube represented the coordinate system origin. The vectors were drawn in the top half of the system. The vectors were posteriorly oriented with respect to the origin in this example.

# 9 Results

## 9.1 Principal elastic components

The medians, minima and maxima of principal elastic constants, or the diagonal components, in MPa of the orthotropic elasticity tensor are shown in Table 4. Regarding the structure stiffness in compression, the largest median was that of  $c_{22}$ , which thus corresponded to the principal stress-strain relation the y-direction. The same component also had the smallest minimum and the largest maximum.  $c_{11}$  was smallest based on its median value. However, this component was relatively close to the  $c_{33}$  median with a difference of 1.721 MPa. These two constants also had a similar minimum, although the maximum of  $c_{11}$  was much larger than that of  $c_{33}$  (difference: 110.9 MPa).

As for the elastic constants in shear, on median based,  $c_{66}$ , which corresponded to shear in the 12-direction, was largest, slightly bigger than  $c_{44}$  (difference: 0.299 MPa), corresponding to the principal shear stiffness at a mechanical test applied in the 32-direction. However,  $c_{44}$  contained the largest minimum, followed by  $c_{66}$ . The maximum of  $c_{66}$  was again largest and that of  $c_{44}$  the smallest.  $c_{55}$ , relating the shear stress and strain in the 13-direction, was the smallest in median and also contained the smallest minimum, although its maximum was in between that of  $c_{44}$  and  $c_{66}$ .

Ratios between the compression stiffness components clearly showed a dominance of stiffness in the y-direction. Looking at the medians of the ratios  $c_{22}/c_{11}$  and  $c_{22}/c_{33}$ , both were well above unity as shown in Table 4. The ratio between the less dominant stiffness components  $c_{33}/c_{11}$  showed a median of close to unity.

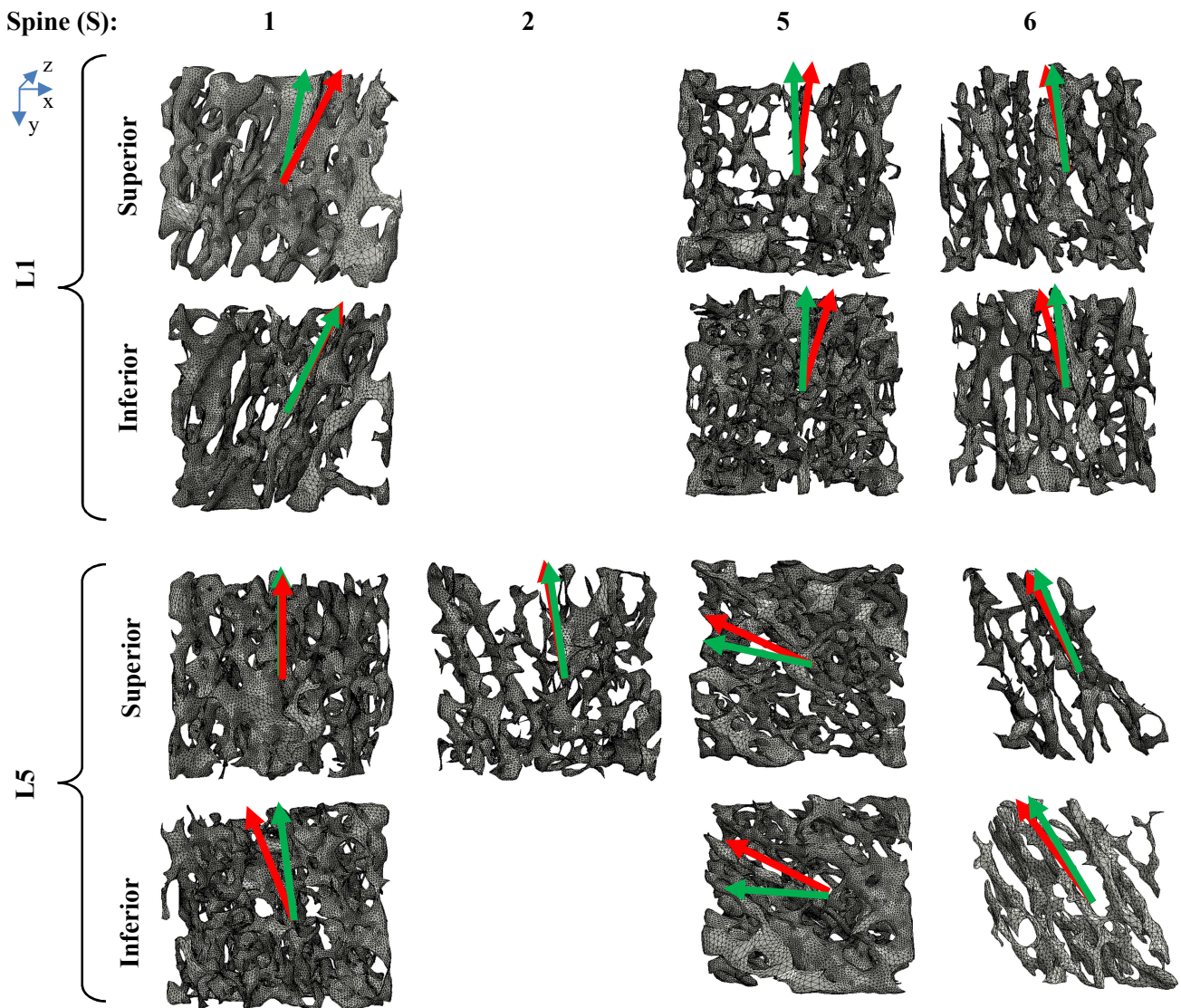
Elastic constant	Median (MPa)	Minimum (MPa)	Maximum (MPa)
$c_{11}$	6.743	1.419	168.771
$c_{22}$	38.693	0.672	254.939
$c_{33}$	8.464	1.329	57.828
$c_{44}$	3.186	0.727	7.19
$c_{55}$	1.913	0.062	9.364
$c_{66}$	3.485	0.274	12.826
$c_{33}/c_{11}$	0.960	0.010	8.576
$c_{22}/c_{11}$	13.352	0.009	46.518
$c_{22}/c_{33}$	4.746	0.045	48.477

**Table 4:** A summary of the values found for the diagonal components of the elasticity tensor by means of their median, minimum and maximum. Note that the minima also include outliers. Ratio's between the principal compressive stiffness components are also given.

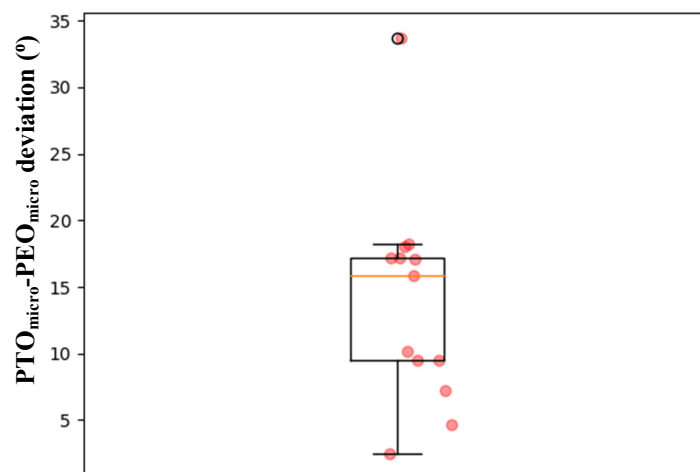
## 9.2 Trabecular and elastic orientations

The deviations of the  $PEOs_{\text{micro}}$  and  $PTOs_{\text{micro}}$  are shown in the xy-plane in Figure 14. The  $PEO_{\text{micro}}$  of  $S1L1_{\text{sup}}$  was right postero-laterally oriented with respect to the axial direction, whereas the  $PTO_{\text{micro}}$  was left postero-laterally oriented. The vectors deviated with angle of  $17.13^\circ$ . For  $S1L1_{\text{inf}}$  the  $PTO_{\text{micro}}$  and  $PEO_{\text{micro}}$  were both oriented in the postero-lateral direction and approximately aligned in the sagittal plane (2D).

However, here, the  $PTO_{micro}$  pointed far to the right and the  $PEO_{micro}$  slightly to the left anatomical direction of the body, causing a 3D deviation of  $15.83^\circ$ .  $S1L5_{sup}$  again showed a close relation between the  $PEO_{micro}$  and  $PTO_{micro}$  in the sagittal plane and both approximately aligned with the axial axis of the cube. The  $PEO_{micro}$  was slightly oriented to the right and the  $PTO_{micro}$  to the left of the cube. The orientations deviated mildly with  $2.50^\circ$ . The  $PEO_{micro}$  and  $PTO_{micro}$  of  $S1L5_{inf}$  were left and right antero-laterally directed with respect to the axial line of the cube, respectively. The deviation angle was  $18.19^\circ$ . The deviation of the  $PEO_{micro}$  and  $PTO_{micro}$  of  $S2L5_{sup}$  was again small, viewed from the 2D sagittal view as Figure 14 suggests, although much larger in 3D being  $17.15^\circ$ . The  $PEO_{micro}$  was oriented towards the left antero-lateral direction, whereas the  $PTO_{micro}$  was oriented towards the right antero-lateral direction. The trabeculae of  $S5L1_{sup}$  on the micro-tissue level were oriented in the left postero-lateral direction according to the  $PTO_{micro}$ . However, the  $PEO_{micro}$  was very slightly oriented in the right antero-lateral direction. The difference resulted in a deviation of  $18.04^\circ$ . The deviation for the cube in  $S5L1_{inf}$  was  $10.15^\circ$ . In the lateral direction, the  $PEO_{micro}$  very slightly oriented to the right, while the  $PTO_{micro}$  did more so. Both were posteriorly directed although the  $PTO_{micro}$  did more so than the  $PEO_{micro}$ .  $S5L5_{sup}$  showed a  $PTO_{micro}$ - $PEO_{micro}$  deviation of  $17.21^\circ$ . Both  $PTO_{micro}$  and  $PEO_{micro}$  were more horizontally oriented than vertically as opposed to most of the other structures. They were anteriorly directed with respect to the defined origin. The  $PTO_{micro}$  deviated to the left and the  $PEO_{micro}$  to the right laterally. The deviation between the  $PTO_{micro}$  and  $PEO_{micro}$  of  $S5L5_{inf}$



**Figure 14:** The visualizations of the PTOs (red) and PEOs (green) in the sagittal, xy-, plane. The cubes of side length 6.0 mm are ordered in the caudal direction from top to bottom.



**Figure 15:** A boxplot showing the distribution of the deviations between the primary trabecular and primary elastic orientations. There was one outlier of 33.70°.

was 33.70°. The PEO<sub>micro</sub> indicated almost an horizontal dominant anterior elastic direction. The PTO<sub>micro</sub> was also anteriorly directed, although less horizontally. Laterally, the PEO<sub>micro</sub> and PTO<sub>micro</sub> both directed very slightly to the right. The PTO<sub>micro</sub> and PEO<sub>micro</sub> of S6L1<sub>sup</sub> both mildly oriented to the posterior side with a small lateral deviation to the right, which was slightly larger for the PTO<sub>micro</sub> than for the PEO<sub>micro</sub>. The angle between the vectors was 4.68°. For S6L1<sub>inf</sub> the deviation was 9.52°. Again, both vectors were mildly posteriorly oriented, the PTO<sub>micro</sub> more than the PEO<sub>micro</sub>. From a coronal view, the PTO<sub>micro</sub> was right laterally and the PEO<sub>micro</sub> left laterally oriented. The PTO<sub>micro</sub> and PEO<sub>micro</sub> of the S6L5<sub>sup</sub> cube followed an anterior right and left lateral direction, respectively. The PTO<sub>micro</sub> again had a stronger anterior tendency than the PEO<sub>micro</sub>. The deviation was 9.46°. For S6L5<sub>inf</sub>, the vectors were oriented in the anterior direction, again with the PTO<sub>micro</sub> doing more so than the PEO<sub>micro</sub>. However, here, both vectors deviated laterally to the right side. The vectors deviated with an angle of 7.20°.

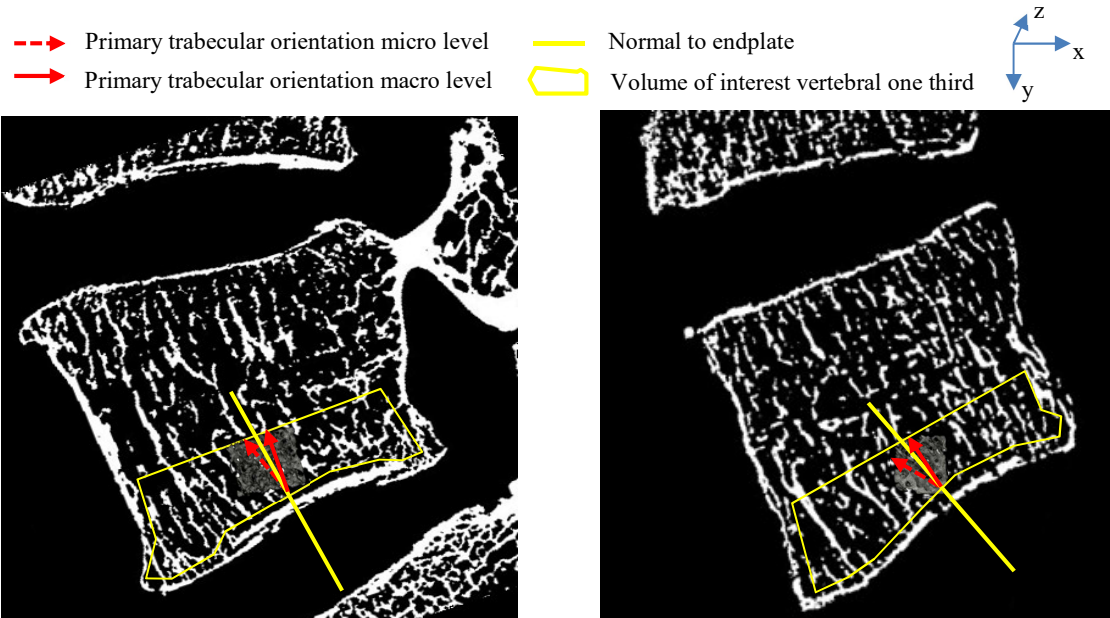
11 out of 13 PEO<sub>micro</sub> were more vertically inclined than their corresponding PTO<sub>micro</sub>. The other 2 cubes, of the S5L5<sub>sup</sub> and S5L5<sub>inf</sub> regions, showed a more horizontally oriented structure in general, i.e. the PTO<sub>micro</sub> deviated more than 45° with the vertical (y-) axis.

The deviations are summarized in the form of a boxplot in Figure 15. The angles were within the range of 2.50° and 18.19°, although there was one outlier of 33.70°. The interquartile range (IQR) was 7.76°. The median was 15.83°. Six deviation angles were relatively close to each other, varying in between 15.83° and 18.19°. Apart from the outlier, the other angles were smaller, in between 2.50° and 10.15°.

In general, PTO<sub>micro</sub> and PEO<sub>micro</sub> showed consistency when comparing the superior to the inferior region within each individual vertebral body. The struts as well as the preferred elastic orientations were equally oriented, anteriorly or posteriorly, for each vertebra in the sagittal plane.

### 9.3 Trabecular and elastic orientations from micro to macro level

11 out of 13 PTO<sub>micro</sub> agreed relatively well on sight with the PTO<sub>macro</sub> (Part I), representing the trabecular orientation of the entire vertebral one-thirds, in the sagittal plane, which can be seen by comparing Figure 14 to the PTO<sub>macro</sub>-NE<sub>macro</sub> visualizations presented in Appendix C. To be more specific, a calculation of the PTO<sub>micro</sub> would lead to a similar relative orientation to the NE<sub>macro</sub> in terms of posterior and anterior direction. The two other PTO<sub>micro</sub>, those of the cubes within S1L5<sub>inf</sub> and S5L5<sub>inf</sub>, were differently oriented with respect to the NE<sub>macro</sub> than the PTO<sub>macro</sub>. The PTO<sub>micro</sub> of S1L5<sub>inf</sub> and S5L5<sub>inf</sub> were both anteriorly



**Figure 16:** The S1L1<sub>inf</sub> (left) and S5L5<sub>inf</sub> (right) cubes showed a primary trabecular orientation in another direction with respect to the normals to the endplate than the PTOs of these entire inferior one thirds

directed with respect to the  $NE_{macro}$  as opposed to the corresponding respective  $PTOs_{macro}$ , which were posteriorly oriented (Figure 16).

Since most  $PEOs_{micro}$  deviated from the  $PTOs_{micro}$  and  $PTOs_{micro}$  were comparable to  $PTOs_{macro}$ , the  $PEOs_{micro}$  consequently deviated from the  $PTOs_{macro}$ . Only the  $PEOs_{micro}$  in S1L5<sub>sup</sub> and S6L1<sub>sup</sub> deviated relatively little from the  $PTOs_{macro}$ , with angles of  $5.93^\circ$  and  $4.29^\circ$ , respectively.

However, the  $PEOs_{micro}$  had a very similar tendency toward anterior and posterior directions relative to the  $NEs_{macro}$  in the sagittal plane. Just like for the  $PTO_{micro}$ , the  $PEOs_{micro}$  in S1L5<sub>inf</sub> and S5L5<sub>inf</sub> did not agree with the  $PTOs_{macro}$  relative to the  $NEs_{macro}$  in these regions. One other disagreement was found. In the superior region of S5L1, the  $PTO_{macro}$  was oriented in the anterior direction with respect to the  $NE_{macro}$ , whereas the  $PEO_{micro}$  of the cube would have been posteriorly oriented relative to the  $NE_{macro}$ . Just like with their  $PTOs$ , all other cubes had  $PEOs$  in agreement with the  $PTOs_{macro}$  regarding the relative anterior or posterior direction to the  $NE_{macro}$ . The agreements between orientational relative to the  $NE_{macro}$  on the micro-level and macro-tissue level are summarized in Table 5.

The  $PTO_{cubes}$  and  $PTO_{part I}$  deviated with  $4.61^\circ (\pm 4.40^\circ)$  on average in the sagittal plane.

Region	$PTO_{micro}$ - $PTO_{macro}$ agreement	$PEO_{micro}$ - $PTO_{macro}$ agreement	$PTO_{micro}$ - $PEO_{micro}$ agreement
S1L1 <sub>sup</sub>	Yes	Yes	✓
S1L1 <sub>inf</sub>	Yes	Yes	✓
S1L5 <sub>sup</sub>	Yes	Yes	✓
S1L5 <sub>sup</sub>	No	No	✓
S2L5 <sub>sup</sub>	Yes	Yes	✓
S5L1 <sub>sup</sub>	Yes	No	✗
S5L1 <sub>inf</sub>	Yes	Yes	✓
S5L5 <sub>sup</sub>	Yes	No	✓
S5L5 <sub>inf</sub>	No	No	✓
S6L1 <sub>sup</sub>	Yes	Yes	✓
S6L1 <sub>inf</sub>	Yes	Yes	✓
S6L5 <sub>sup</sub>	Yes	Yes	✓
S6L5 <sub>inf</sub>	No	No	✓

**Table 5:** An outline of the agreements between the primary trabecular orientation ( $PTO_{micro}$ ) on the micro scale and macro scale ( $PTO_{macro}$ ) and between the primary elastic orientation on the micro scale ( $PEO_{micro}$ ) and  $PTO_{macro}$  with regard to their anterior or posterior tendency relative to the normal to the endplate ( $NE_{macro}$ ). The outmost right column depicts whether the  $PTO_{micro}$  and the  $PEOs_{micro}$  agreed regarding their anterior or posterior tendency relative to the  $NE_{macro}$ .



# 10 Discussion

The novelty of this work lies in the abstraction of the elastic and fabric orientation computations on a micro-level to loading directions as a part of spine biomechanics on the macro scale ( $> 10$  mm).

The selection of trabeculae was limited to certain criteria since cubic models of the trabeculae allow for easy elastic assessment via FE simulations, they should be within the VOIs of Part I, and the chosen trabecular pieces should be approximately at similar central regions of each vertebra for consistency. Combined with the fact that samples were taken from elderly and were thus likely to contain highly porous structures, obtaining sufficiently homogeneous and continuous bone models was strongly hindered. It was emphasized in an earlier recent study by Unnikrishnan et al.<sup>29</sup> on orthotropy of vertebral trabecular bone in elderly, that in such cases, the size of VOI is of substantial influence on the agreement between elastic and fabric principal directions. The similarity of the study by Unnikrishnan et al. and the current one, makes the former useful for comparison.

## 10.1 Implications for mechanical anisotropy

Regarding the principal elastic constants (section 9.1), the largest compressive elastic constant was clearly  $c_{22}$ , which corresponded to the principal compressive stiffness in the y-direction. Looking at the cubes (Figure 14), this large relative stiffness was sensible considering that the structures predominantly follow the vertical direction. They are thus more directed along the y-axis than the x- and z-axis. The finding that  $c_{22}$  was dominant is validated, as stiffness should be largest along the axis along which the most bone appears, the z/y-axis.

Regarding the compressive principal elastic constants (Table 4,  $c_{11}$ ,  $c_{22}$ ,  $c_{33}$ ), medians were within the range defined by the minima and maxima reported in the study by Unnikrishnan et al. The values were in the same order of magnitude. Two shear principal elastic constants (Table 4,  $c_{55}$ ,  $c_{66}$ ) were smaller and one was within the given range in the former study ( $c_{44}$ ). The minimum of  $c_{55}$  (0.062) was unusually small and actually represented an outlier. Although all other elastic constants were roughly in a similar order of magnitude, the medians, minima and maxima of the current study were considerably and consistently smaller than the ones found by Unnikrishnan et al. A reason for the inequality of stiffness magnitudes lies in the assignment of different Young's moduli to the FE-models, which was 13 GPa in the work of Unnikrishnan et al. and 1 GPa in the current study. Increasing the Young's modulus to 13 GPa would result in closer stiffness levels.

The ratios between compressive stiffness constants found in this study indicate a preference of vertebral trabecular bone to form an orthotropic above a transversely anisotropic structure. Anisotropy was thus defined through mechanical characteristics of the trabecular cubes. Transverse anisotropy would result in a ratio of the less dominant stiffness constants ( $c_{33}/c_{11}$ ) to be close to unity. Although the median did so, the range between the minimum and maximum and an IQR of 2.59 MPa proves a too big variation to show transverse anisotropy. This finding supports the idea of trabecular bone being orthotropic rather than transversely isotropic.

Following Unnikrishnan et al., an increase in BV/TV would lead to increased material symmetry, thus a tendency of the ratio between the less dominant compressive principal elastic constants ( $c_{11}/c_{33}$ ) towards unity. The relation between BV/TV and  $c_{11}/c_{33}$  was not reported here, since the combination of a small sample size ( $n = 13$ ) and correlation factor ( $R^2 = 0.18$ ) were insufficient for a statement regarding this aspect.

## 10.2 Relation between trabecular and elastic orientations

There was a strong deviation in general ( $\text{avg.}=13.90^\circ \pm 8.04^\circ$ ) between the PEOs and PTOs on the micro level, considering that they should closely align. This outcome was most likely due to the removal of unconnected struts before performing FE-analysis but after determining the PTOs. The unconnected trabeculae would act as singularities in FE simulations. Solutions would not converge as a result.

To prevent divergence, singularities were deleted. Some trabeculae were therefore included during the calculation of the  $\text{PTOs}_{\text{micro}}$  whilst being absent in the FE-computations. The removed struts could be of substantial influence on principal directions, hence probably lead to different fabric than elastic orientations. Unnikrisnan et al. found a median deviation between elastic and trabecular primary orientations of  $5.61^\circ$ , which is much smaller than the deviation reported here. In their study, elderly vertebral samples were used as well and relative bone volumes were in a similar range as reported here, indicating that bone quality should be comparable. Thus, the problem of the removal of disconnected structures should apply to their study as well. A logical reason for the difference between the findings is the high resolution used by Unnikrishnan et al. relative to the resolution in the current study, which were 37 and  $120 \mu\text{m}$ , respectively. Since it was needed to capture the complete vertebral cancellous structures, FOVs had to be sufficiently large, resulting lower resolutions. The lower resolution led to less accurate thresholding, which probably caused the imaged structures to be less connected than they are *in vivo*. Although low resolutions hinder quantifications of trabecular microstructures, they remain relevant in clinical context, as voxel sizes of clinical CT-scans are normally maximally  $250 \mu\text{m}$ <sup>3115</sup>. There are improvements being made to increase clinical CT-scan resolution to 82 microns/voxel<sup>115</sup>.

In general, non-alignments could be additionally due to the advanced age of the samples<sup>29</sup>. As a result, they exhibited less homogeneous and more sparse structures. It is therefore recommended that future fundamental studies use denser trabecular specimens. From a clinical perspective, the use of the current samples remain relevant, as increased porosity and fragility of internal vertebral structures is a major issue for elderly. In fact, deviations between elastic principal directions and fabric principal directions might be used as an indicator for the mechanical integrity of osteoporotic vertebrae. Mechanical analysis of trabecular bone could be done in a more medical context in the future. It is advised to explore the use of fabric and elastic quantifications, such as their components and principal directions, as parameters in optimizations of diagnostics strategies, orthopaedic implants and micro engineering technology.

Although  $\text{PEO}_{\text{micro}}$ - $\text{PTO}_{\text{micro}}$  angles were large, the average deviation ( $13.90^\circ$ ) was smaller than a deviation found by Odgaard et al. in a whale vertebral specimen, which was  $18.40^\circ$ . Furthermore, looking at the structures from the sagittal plane (xy-plane), as presented in Figure 14, all  $\text{PEOs}_{\text{micro}}$  have an approximate similar deviation with respect to the coordinate system's axes. To elaborate, the direction of the  $\text{PEOs}_{\text{micro}}$  are equal to the  $\text{PTOs}_{\text{micro}}$  in the sense that they are both anteriorly or posteriorly oriented relative to the y-axis for all the cubes.

Apparently, deviations were less related in the coronal view, since almost all  $\text{PEOs}_{\text{micro}}$  and  $\text{PTOs}_{\text{micro}}$  were oppositely directed relative to the y-axis in the coronal plane (zy-plane). Taking into account that the removal of trabecular singularities probably was the biggest contributor to the deviations, more singularities could be of larger influence on the trabecular orientation in the coronal plane than in the sagittal plane.

## 10.3 Relation between trabecular micro mechanics and spine biomechanics

Although the  $\text{PEOs}_{\text{micro}}$  and  $\text{PTOs}_{\text{micro}}$  did not closely align in 3D, their tendency to both follow the anterior or posterior direction relative to the  $\text{NE}_{\text{macro}}$  were similar on the micro scale. An exception was the  $\text{PEO}_{\text{micro}}$  and  $\text{PTO}_{\text{micro}}$  of  $\text{S5L1}_{\text{sup}}$ , which were posteriorly and anteriorly oriented with respect to the  $\text{NE}_{\text{macro}}$ , respectively. The inaccuracy of the  $\text{PEO}_{\text{micro}}$  determination apparently lead to a change in orientation relative to the  $\text{NE}_{\text{macro}}$  in this particular case.

It was also noticeable from the sagittal point of view, as visualized in Figure 14, that the  $PTOs_{micro}$  and  $PEOs_{micro}$  of the superior region within each vertebra were similar to the  $PTOs_{micro}$  and  $PEOs_{micro}$  in the inferior region in relation to the y-axes. This insight reveals that inconsistencies of the differences in the PTOs relative to the NE for superior and inferior regions between the vertebrae are more due to differing  $NEs_{macro}$  per vertebra than PTOs. Thus, the axial force vector in the spines used in this study changed due to the curve, while the primary trabecular directions remained relatively constant per vertebral body.

Furthermore, in comparison to the  $PTOs_{macro}$ , the relative orientations agreed arguably well, with 11 out of 13 agreements between the  $PTO_{micro}$  and  $PTOs_{macro}$  and 10 out of 13 agreements between the  $PEOs_{micro}$  and  $PTOs_{macro}$ . The cubes were able to predict orientations on a larger scale well from this view. However, deviations between the  $PTOs_{micro}$  and  $PTOs_{macro}$  still was  $4.61^\circ$  with a relatively large standard deviation of  $4.40^\circ$ . From these findings it can thus be drawn that most, but not all, cubes on the micro level were typical for the regions on the macro level.

The fact that tendencies between the  $PTOs_{macro}$  and  $NEs_{macro}$  and between the  $PEOs_{micro}$  and  $NEs_{micro}$  were similar and deviated with respect to the  $NEs_{macro}$ , indicates that adaptation to secondary loading directions in addition to the dominant compressive force direction is apparent on both the macro- (Part I) and micro-tissue level (Part II). However, note that the deviation between the PTO on the micro-tissue level and the PTO on the macro-tissue level of  $4.61^\circ$  means that measurements on the micro-tissue level are still not sufficiently accurate to predict structural parameters on the macro-tissue level. Furthermore, it is emphasised here that future applicative research should focus on the extent to which trabecular bone adapts to primary (compression) and secondary (shear) loading directions along the different anatomic scales. As mentioned in the discussion of Part I (section 5), an advised approach is *in vivo* time-lapsed imaging. Applying shear forces on trabecular bone samples and recording and analysing changes in trabecular bone orientation over time would provide information on the extent to which trabecular bone adapts to shear. Understanding how trabecular bone in vertebrae relates to biomechanics of the spine may be of significant value in diagnostics. For instance, if increased shear in the spine could be read from patterns in vertebrae at a young age, clinicians can predict whether it is likely if a person will develop a scoliotic spine. Treatment could be appropriately adjusted to ensure a life for the patient without limited mobility or worse.

# 11 Conclusion

Trabecular structures within the superior and inferior regions of earlier investigated vertebral trabecular bone were successfully analysed on different elastic characteristics. The magnitude of the stiffness constants was within a reasonable range (1-250 MPa approximately, excluding outliers). Regressions between bone volume fraction and material symmetry were hindered due to a limited sample size ( $n = 13$ ). Regarding primary fabric and elastic orientations, close alignment between the two was not found as the average deviation was  $13.90^\circ (\pm 8.04^\circ)$ . The reason for this outcome was a combination of poor bone quality related to the advanced sample ages and a low  $\mu$ CT resolution (voxel size =  $120 \mu\text{m}^3$ ). The clinical relevance of such deviations could be found by relating them to bone quality indicators as an approach to assess the health of the bone. Finally, overall tendencies of primary fabric and elastic orientations on the micro-tissue level (1-10 mm) agreed well with those on the macro-tissue scale ( $>10$  mm), both suggesting that, besides compression, secondary loading directions such as shear are of influence on trabecular bone adaptation. This finding implies that research to bone adaptation across scales could provide suggestions on how to use trabecular bone analyses on a small scale to predict unhealthy skeletal growth of patients at an early stage.

# References

1. Maurer, M. M., Weinkamer, R., Müller, R. & Ruffoni, D. Does mechanical stimulation really protect the architecture of trabecular bone ? A simulation study. *Biomech. Model. Mechanobiol.* 795–805 (2015). doi:10.1007/s10237-014-0637-x
2. Hamed, E., Jasiuk, I., Yoo, A., Lee, Y. & Liszka, T. Multi-scale modelling of elastic moduli of trabecular bone. *J. R. Soc. Interface* **9**, 1654–1673 (2012).
3. Homminga, J., Lochmu, E. M., Eckstein, F. & Huiskes, R. The osteoporotic vertebral structure is well adapted to the loads of daily life , but not to infrequent ““ error ”” loads. *Bone* **34**, 510–516 (2004).
4. Kocijan, R. *et al.* Bone structure assessed by HR-pQCT , TBS and DXL in adult patients with different types of osteogenesis imperfecta. *Osteoporos. Int.* 2431–2440 (2015). doi:10.1007/s00198-015-3156-4
5. U.S. Department of Health and Human Services. Bone Health and Osteoporosis: A Report of the Surgeon General. Rockville, MD: U.S. Department of Health and Human Services, Office of the Surgeon General. 40–61 (2004).
6. Roodman, G. D., Siris, E. S. & Roodman, G. D. in *Primer on the Metabolic Bone Diseases and Disorders of Mineral Metabolism* 659–668 (2015). doi:10.1002/9780470623992.ch72
7. Wang, Z. *et al.* Unique local bone micro characteristics in iliac crest bone biopsy from adolescent idiopathic scoliosis with severe spinal deformity. *Nat. Publ. Gr.* 1–10 (2017). doi:10.1038/srep40265
8. Boldt, J. G., Cartillier, J.-C., Machenaud, A. & Vidalain, J.-P. Long-term Bone Remodeling in HA-coated Stems: A Radiographic Review of 208 Total Hip Arthroplasties (THAs) with 15 to 20 Years Follow-up. *Surg. Technol. Int.* **27**, 279–286 (2015).
9. Lin, C. Y., Kikuchi, N. & Hollister, S. J. A novel method for biomaterial scaffold internal architecture design to match bone elastic properties with desired porosity. *J. Biomech.* **37**, 623–636 (2004).
10. Keaveny, T. M., Mmacro, E. F., Niebur, G. L. & Yeh, O. C. Biomechanics of Trabecular Bone. 1–25 (2001).
11. Klein-Nulend, J., Bakker, A. D., Bacabac, R. G., Vatsa, A. & Weinbaum, S. Mechanosensation and transduction in osteocytes. *Bone* **54**, 182–190 (2013).
12. Van Rietbergen, B., Odgaard, A., Kabel, J. & Huiskes, R. Direct mechanics assessment of elastic symmetries and properties of trabecular bone architecture. *J. Biomech.* **29**, 1653–1657 (1996).
13. Odgaard, A., Kabel, J., van Rietbergen, B., Dalstra, M., Huiskes, R. Fabric and Elastic Principal Directions of Cancellous Bone are Closely Related. *J. Biomech.* **30**, 487–495 (1997).
14. Kabel, J., Odgaard, A. & Huiskes, R. Constitutive Relationships of Fabric, Density, and Elastic Properties in Cancellous Bone Architecture. *Bone* **25**, 481–486 (1999).
15. Ulrich, D., Laib, A. & Ru, P. The Ability of Three-Dimensional Structural Indices to Reflect Mechanical Aspects of Trabecular Bone. *Bone* **25**, 55–60 (1999).
16. Homminga, J., Mccreadie, B. R., Weinans, H. & Huiskes, R. The dependence of the elastic properties of osteoporotic cancellous bone on volume fraction and fabric. *J. Biomech.* **36**, 1461–1467 (2003).
17. Wolff, J. *Das Gesetz der Transformation der Knochen.* (Hirchwild, Berlin, 1892).
18. Tsubota, K., Suzuki, Y., Yamada, T. & Hojo, M. Computer simulation of trabecular remodeling in human proximal femur using large-scale voxel FE models : Approach to understanding Wolff ’ s law Entire bone Cancellous structure. *J. Biomech.* **42**, 1088–1094 (2009).
19. Boyle, C. & Kim, I. Y. Three-dimensional micro-level computational study of Wolff’s law via trabecular bone remodeling in the human proximal femur using design space topology optimization. *J. Biomech.* **44**, 935–942 (2011).
20. Villette, C. C. & Phillips, A. T. M. Microscale poroelastic metamodel for efficient mesoscale bone remodelling simulations. *Biomech. Model. Mechanobiol.* (2017). doi:10.1007/s10237-017-0939-x
21. Hammer, A. The paradox of Wolff’s theories. *Irish J. Med. Sci. (1971 -)* **184**, 13–22 (2015).
22. Heřt, J. A new attempt at the interpretation of the functional architecture of the cancellous bone. *J. Biomech.* **27**, 239–242 (1994).

23. Pidaparti, R.M.V., Turner, C. H. Cancellous Bone Architecture: Advantages of Nonorthogonal Trabecular Alignment under Multidirectional Joint Loading. *J. Biomech.* **30**, 979–983 (1997).
24. Skedros, J.G., Baucom, S. L. Mathematical Analysis of Trabecular Trajectories in Apparent Trajectorial Structures: The Unfortunate Historical Emphasis on the Human Proximal Femur. *J. Theor. Biol.* **244**, 15–45 (2007).
25. Hert, J. A new explanation of the cancellous bone architecture. *Funct. Dev. Morphol.* **2**, 15–21 (1992).
26. Cheng, J. C. *et al.* Adolescent idiopathic scoliosis. *Nature* **1**, (2015).
27. Melnyk, A. D. *et al.* The effect of disc degeneration on anterior shear translation in the lumbar spine. *J. Orthop. Res.* **33**, 450–457 (2015).
28. Chadha, M., Sharma, G., Arora, S. S. & Kochar, V. Association of facet tropism with lumbar disc herniation. *European Spine Journal* **22**, 1045–1052 (2013).
29. Unnikrishnan, G. U., Gallagher, J. A., Hussein, A. I., Barest, G. D. & Mmacro, E. F. Elastic Anisotropy of Trabecular Bone in the Elderly Human Vertebra. *J. Biomech. Eng.* **137**, 1–6 (2015).
30. Robling, A. G., Castillo, A. B. & Turner, C. H. Biomechanical and molecular regulation of bone remodeling. *Annu. Rev. Biomed. Eng.* **8**, 455–498 (2006).
31. Raggatt, L. J. & Partridge, N. C. Cellular and Molecular Mechanisms of Bone Remodeling \*. *J. Biol. Chem.* **285**, 25103–25108 (2010).
32. Frost, H. M. The Utah paradigm of skeletal physiology : an overview of its insights for bone , cartilage and collagenous micro macros. *J. Bone Miner. Metab.* **18**, 305–316 (2000).
33. Herman, B. C., Cardoso, L., Majeska, R. J., Jepsen, K. J. & Schaf, M. B. Activation of bone remodeling after fatigue : Differential response to linear microcracks and diffuse damage. *Bone* **47**, 766–772 (2010).
34. Chen, J.-H., Liu, C., You, L. & Simmons, C. A. Boning up on Wolff’s Law: Mechanical regulation of the cells that make and maintain bone. *J. Biomech.* **43**, 108–118 (2010).
35. Maguire, P. *et al.* Analysing a Single Osteoblast Cell : Mechanotransduction Using Atomic Force Microscope Indention Indented cell. *Microsc. Microanal.* **11**, 952–953 (2017).
36. Verborgt, O., Gibson, G. J. & Schaffler, M. B. Loss of Osteocyte Integrity in Association with Microdamage and Bone Remodeling After Fatigue In Vivo \*. *J. Bone Miner. Res.* **15**, 60–67 (2000).
37. Cardoso, L., Herman, B. C., Verborgt, O., Laudier, D. & Majeska, R. J. Osteocyte Apoptosis Controls Activation of Intracortical Resorption in Response to Bone Fatigue. *J. Bone Miner. Res.* **24**, 597–605 (2009).
38. Heino, T. J., Hentunen, T. A. & Väänänen, H. K. Osteocytes Inhibit Osteoclastic Bone Resorption Through Transforming Growth Factor- b : Enhancement by Estrogen. *J. Cell. Biochem.* **85**, 185–197 (2002).
39. Kennedy, O. D., Laudier, D. M., Majeska, R. J., Sun, H. B. & Schaffler, M. B. Osteocyte Apoptosis is Required for Production of Osteoclastogenic Signals Following Bone Fatigue in vivo. *Bone* **64**, 132–137 (2014).
40. Mchugh, K. P. *et al.* Mice lacking  $\beta$  3 integrins are osteosclerotic because of dysfunctional osteoclasts. *J. Clin. Invest.* **105**, 433–440 (2000).
41. Teitelbaum, S. L. Bone Resorption by Osteoclasts. *Science (80-. )*. **289**, 1504–1509 (2000).
42. Delaisse, J. The reversal phase of the bone-remodeling cycle : cellular prerequisites for coupling resorption and formation. *Bonekey Rep.* **3**, 1–8 (2014).
43. Udagawa, N. *et al.* Osteoprotegerin produced by osteoblasts is an important regulator in osteoclast development and function. *Endocrinology* **141**, 3478–3484 (2000).
44. Zhang, K. *et al.* E11/gp38 selective expression in osteocytes: regulation by mechanical strain and role in dendrite elongation. *Mol. Cell. Biol.* **26**, 4539–4552 (2006).
45. Plotkin, L.I., Bellido, T. Osteocytic signalling pathways as therapeutic targets for bone fragility. *Nat. Publ. Gr.* 1–13 (2016). doi:10.1038/nrendo.2016.71
46. Weinbaum, S., Cowin, S.C., Y. Z. A model for the excitation of osteocytes by mechanical loading-induced bonde fluid shear stresses. *J. Biomech.* **27.3**, 339–360 (1994).
47. Wijeratne, S. S. *et al.* Single molecule force measurements of perlecan/HSPG2: A key component of the osteocyte pericellular matrix. *Matrix Biol.* **50**, 27–38 (2016).
48. Wang, Y., Mcnamara, L. M., Schaffler, M. B. & Weinbaum, S. A model for the role of integrins in flow induced mechanotransduction in osteocytes. *PNAS* **104**, 15941–15946 (2007).

49. Nulend, Klein, Bacabac, R.G., Bakker, A. D. Mechanical loading and how it affects bone cells : the role of the osteocyte cytoskeleton in maintaining our skeleton. *Eur. Cells Mater.* **24**, 278–291 (2012).
50. Thi, M., Suadicani, S., Schaffler, M., Weinbaum, S. & Spray, D. Polarized mechanotransduction in osteocytes: role of  $\alpha$ V $\beta$ 3 integrin on the cell processes (1180.9). *FASEB J.* **28**, (2014).
51. Haugh, M. G., Vaughan, T. J. & McNamara, L. M. The role of integrin  $\alpha$ V $\beta$ 3 in osteocyte mechanotransduction. *J. Mech. Behav. Biomed. Mater.* **42**, 67–75 (2015).
52. Rosa, N., Simoes, R., Magalhães, F.D., Marques, A. T. From mechanical stimulus to bone formation : A review. *Med. Eng. Phys.* 719–728 (2015). doi:10.1016/j.medengphy.2015.05.015
53. Weivoda, M. M. *et al.* Wnt Signaling Inhibits Osteoclast Differentiation by Activating Canonical and Noncanonical cAMP/PKA Pathways. *J. bone Miner. Res.* **31**, 65–75 (2016).
54. Jang, I. G. & Kim, I. Y. Computational study of Wolff's law with trabecular architecture in the human proximal femur using topology optimization. *J. Biomech.* **41**, 2353–2361 (2008).
55. Huiskes, R. *et al.* Adaptive bone-remodeling theory applied to prosthetic-design analysis. *J. Biomech.* **20**, 1135–1150 (1987).
56. Weinans, H., Huiskes, R. and Grootenboer, H. J. The Behavior of Adaptive Bone-Remodeling Simulation Models. *J. Biomech.* **25**, 1425–1441 (1992).
57. Weinans, H., Huiskes, R. & Grootenboer, H. J. Effects of Material Properties of Femoral Hip Components on Bone Remodeling. *J. Orthop. Res.* 845–853 (1992).
58. Adachi, Taiji, Tomita, Y., Sakaue, H., Tanaka, M. Simulation of Trabecular Surface Remodeling based on Local Stress Nonuniformity. *Trans. Japanese Soc. Mech. Eng.* **63**, 777–784 (1997).
59. Tsubota, K., Adachi, T. & Tomita, Y. Functional adaptation of cancellous bone in human proximal femur predicted by trabecular surface remodeling simulation toward uniform stress state. *J. Biomech.* **35**, 1541–1551 (2002).
60. Lanyon, L. E. Experimental support for the trajectorial theory of bone structure. *Bone Joint J.* **56**, 160–166 (1974).
61. Ford, C. M. & Keaveny, T. M. The Dependence of Shear Failure Properties of Trabecular Bone on Apparent Density and Trabecular Orientation. *J. Biomech.* **29**, 1309–1317 (1996).
62. Mullender, M. G. & Huiskes, R. Proposal for the regulatory mechanism of Wolff's law. *J. Orthop. Res.* **13**, 503–512 (1995).
63. Jang, I.G., Kim, I.Y., Kwak, B. M. Analogy of Strain Energy Density Based Bone-Remodeling Algorithm and Structural. *J. Biomech.* **131**, 1–7 (2009).
64. Christen, P. *et al.* Bone remodelling in humans is load-driven but not lazy. *Nature* (2014). doi:10.1038/ncomms5855
65. Kim, I. Y. & Kwak, B. M. Design space optimization using a numerical design continuation method. *Int. J. Numer. Methods Eng.* **53**, 1979–2002 (2002).
66. Bendsoe, M. P. & Sigmund, O. *Topology Optimization - Theory, Methods, and Applications.* (Springer Verlag, 2003).
67. Ashman, R. B., Cowin, S. C., Van Buskirk, W. C. & Rice, J. C. A continuous wave technique for the measurement of the elastic properties of cortical bone. *J. Biomech.* **17**, 349–361 (1984).
68. Turner, C. H., Rho, J., Takano, Y., Tsui, T. Y. & Pharr, G. M. The elastic properties of trabecular and cortical bone micros are similar: results from two microscopic measurement techniques. *J. Biomech.* **32**, 437–441 (1999).
69. Cuppone, M., Seedhom, B. B., Berry, E. & Ostell, A. E. The longitudinal Young's modulus of cortical bone in the midshaft of human femur and its correlation with CT scanning data. *Calcif. Micro Int.* **74**, 302–309 (2004).
70. Beaupre, G. S., Orr, T. E. & Carter, D. R. An approach for time-dependent bone modeling and remodeling--theoretical development. *J. Orthop. Res.* **8**, 651–661 (1990).
71. Hambl, R., Katerchi, H. & Benhamou, C. Multiscale methodology for bone remodelling simulation using coupled finite element and neural network computation. *Biomech. Model. Mechanobiol.* **10**, 133–145 (2011).
72. Fernandes, P., Rodrigues, H. & Jacobs, C. A Model of Bone Adaptation Using a Global Optimisation Criterion Based on the Trajectorial Theory of Wolff. *Comput. Methods Biomech. Biomed. Engin.* **2**, 125–138 (1999).
73. Geraldes, D. M. & Phillips, A. T. M. A comparative study of orthotropic and isotropic bone

- adaptation in the femur. *Int. j. numer. method. biomed. eng.* **30**, 873–889 (2014).
74. Murray, P. D. F. *Bones: a study of the development and structure of the vertebrate skeleton*. (CUP Archive, 1936).
  75. Carter, D. R., Orr, T. E. & Fyhrie, D. P. Relationships between loading history and femoral cancellous bone architecture. *J. Biomech.* **22**, 231–244 (1989).
  76. López-Vaca, O. R. & Garzón-Alvarado, D. A. Spongiosa Primary Development: A Biochemical Hypothesis by Turing Patterns Formations. *Comput. Math. Methods Med.* **2012**, 748302 (2012).
  77. Keaveny, Tony M., Mmacro, E.F., Niebur, G.L., Yeh, O. C. Biomechanics of Trabecular Bone. *Annu. Rev. Biomed. Eng.* **3**, 307–333 (2001).
  78. Wang, X. & Niebur, G. L. Microdamage propagation in trabecular bone due to changes in loading mode. *J. Biomech.* **39**, 781–790 (2006).
  79. Geraldes, D. M., Modenese, L. & Phillips, A. T. M. Consideration of multiple load cases is critical in modelling orthotropic bone adaptation in the femur. *Biomechanics and Modeling in Mechanobiology* **15**, 1029–1042 (2016).
  80. Newitt, D.C., Majumdar, S., van Rietbergen, B., von Ingersleben, G., Harris, S.T., Genant, H.K., Chesnut, C., Garnero, P., MacDonald, B. In Vivo Assessment of Architecture and Micro-Finite Element Analysis Derived Indices of Mechanical Properties of Trabecular Bone in the Radius. *Osteoporos. Int.* **13**, 6–17 (2002).
  81. Hahn, M., Vogel, M., Pompesius-Kempa, M. & Delling, G. Trabecular bone pattern factor—a new parameter for simple quantification of bone microarchitecture. *Bone* **13**, 327–330 (1992).
  82. Hernandez, C. J., Beaupré, G. S., Keller, T. S. & Carter, D. R. The influence of bone volume fraction and ash fraction on bone strength and modulus. *Bone* **29**, 74–78 (2001).
  83. Cowin, S. C. The Relationship between the Elasticity Tensor and the Fabric Tensor. *Mech. Mater.* **4**, 137–147 (1985).
  84. Perilli, E., Parkinson, I. H. & Reynolds, K. J. Micro-CT examination of human bone: from biopsies towards the entire macro. *Ann. dell'Istituto Super. di Sanità* **48**, 75–82 (2012).
  85. Low, S. C., Bain, G. I., Findlay, D. M., Eng, K. & Perilli, E. External and internal bone micro-architecture in normal and Kienböck's lunates: A whole-bone micro-computed tomography study. *J. Orthop. Res.* **32**, 826–833 (2014).
  86. Stauber, M. & Müller, R. in *Osteoporosis: Methods and Protocols* (ed. Westendorf, J. J.) 273–292 (Humana Press, 2008). doi:10.1007/978-1-59745-104-8\_19
  87. Parsa, A., Ibrahim, N., Hassan, B., van der Stelt, P. & Wismeijer, D. Bone quality evaluation at dental implant site using multislice CT, micro-CT, and cone beam CT. *Clin. Oral Implants Res.* **26**, e1–e7 (2015).
  88. Moreno, R., Borga, M. & Smedby, O. Generalizing the mean intercept length tensor for gray-level images. *Med. Phys.* **39**, 4599–4612 (2012).
  89. Schindelin, J. *et al.* Fiji: an open-source platform for biological-image analysis. *Nat Meth* **9**, 676–682 (2012).
  90. Qiang, M., Chen, Y., Zhang, K., Li, H. & Dai, H. Measurement of three-dimensional morphological characteristics of the calcaneus using CT image post-processing. *J. Foot Ankle Res.* **7**, 19 (2014).
  91. Lenaerts, L., Wirth, A. J. & van Lenthe, G. H. Quantification of trabecular spatial orientation from low-resolution images. *Comput. Methods Biomech. Biomed. Engin.* **18**, 1392–1399 (2015).
  92. Odgaard, A. Three-dimensional methods for quantification of cancellous bone architecture. *Bone* **20**, 315–328 (1997).
  93. Klatt, M. A. & Mecke, K. Mean-intercept anisotropy analysis of porous media . I . Analytic formulae for anisotropic Boolean models. *Med. Phys.* **0**, (2017).
  94. Harrigan, T. P. & Mann, R. W. Characterization of microstructural anisotropy in orthotropic materials using a second rank tensor. *J. Mater. Sci.* **19**, 761–767 (1984).
  95. Robin, P.-Y. F. Determination of fabric and strain ellipsoids from measured sectional ellipses — theory. *J. Struct. Geol.* **24**, 531–544 (2002).
  96. Ketcham, R. & Ryan, T. M. Angular orientation of trabecular bone in the femoral head and its relationship to hip joint loads in leaping primates. *J. Morphol.* **265**, 249–263 (2005).
  97. Kersh, M. E. *et al.* Measurement of structural anisotropy in femoral trabecular bone using clinical-resolution CT images. *J. Biomech.* **46**, 2659–2666
  98. Hosseini, H. S., Maquer, G. & Zysset, P. K.  $\mu$ CT-based trabecular anisotropy can be reproducibly

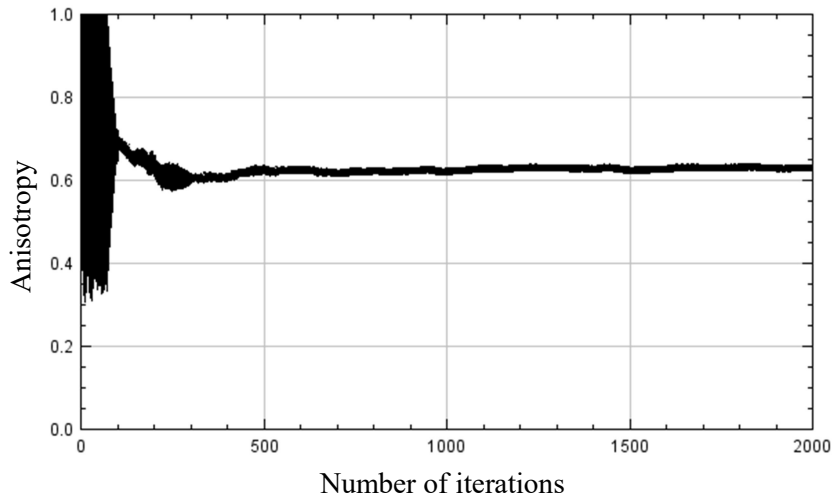


- computed from HR-pQCT scans using the triangulated bone surface. *Bone* **97**, 114–120 (2017).
99. Smit, T.H., Odgaard, A., Schneider, E. Structure and function of vertebral trabecular bone. *Spine (Phila. Pa. 1976)*. (1998).
  100. Smit, T. H. The use of a quadruped as an in vivo model for the study of the spine - biomechanical considerations. *Eur. spine J. Off. Publ. Eur. Spine Soc. Eur. Spinal Deform. Soc. Eur. Sect. Cerv. Spine Res. Soc.* **11**, 137–144 (2002).
  101. Busscher, I., Ploegmakers, J. J. W., Verkerke, G. J. & Veldhuizen, A. G. Comparative anatomical dimensions of the complete human and porcine spine. *European Spine Journal* **19**, 1104–1114 (2010).
  102. Doube, M. *et al.* BoneJ: Free and extensible bone image analysis in ImageJ. *Bone* **47**, 1076–1079 (2010).
  103. Krause, M. *et al.* Effects of long-term alendronate treatment on bone mineralisation, resorption parameters and biomechanics of single human vertebral trabeculae. *Eur. Cells Mater.* **28**, 152–165 (2014).
  104. Hibbeler, R. C. *Statics and Mechanics of Materials*. (Pearson Education, 2011).
  105. Kourtis, D., Magnusson, M. L., Smith, F., Hadjipavlou, A. & Pope, M. H. Spine Height and Disc Height Changes As the Effect of Hyperextension Using Stadiometry and MRI. *The Iowa Orthopaedic Journal* **24**, 65–71 (2004).
  106. Hirata, H. *et al.* A rat tail temporary static compression model reproduces different stages of intervertebral disc degeneration with decreased notochordal cell phenotype. *J. Orthop. Res.* **32**, 455–463 (2014).
  107. Adams, Michael A., Roughley, P. j. What is Intervertebral Disc Degeneration, and What Causes it? *Spine (Phila. Pa. 1976)*. **31**, 2151–2161 (2006).
  108. Yeni, Y. N., Kim, D.-G., Divine, G. W., Johnson, E. M. & Cody, D. D. Human cancellous bone from T12–L1 vertebrae has unique microstructural and trabecular shear stress properties. *Bone* **44**, 130–136 (2009).
  109. Majumdar, S. *et al.* Correlation of Trabecular Bone Structure with Age, Bone Mineral Density, and Osteoporotic Status : In Vivo Studies in the Distal Radius Using High Resolution Magnetic Resonance Imaging. *J. Bone Miner. Res.* **12**, 111–118 (1997).
  110. Alexandru, D. & So, W. Evaluation and Management of Vertebral Compression Fractures. *The Permanente Journal* **16**, 46–51 (2012).
  111. Karadogan E., R. L. W. Three-Dimensional Static Modeling of the Lumbar Spine. **0**, 2–6 (2012).
  112. Gross, T., Pahr, D., Gross, T., Pahr, D. H. & Zysset, P. K. Morphology-elasticity relationships using decreasing fabric information of human trabecular bone from ... anatomical locations. *Biomech. Model. Mechanobiol.* (2012). doi:10.1007/s10237-012-0443-2
  113. Berggren, S. A., Lukkassen, D., Meidell, A. & Simula, L. Some Methods for Calculating Stiffness Properties of Periodic Structures. *Appl. Math.* **48**, 97–110 (2003).
  114. Van Rietbergen, B., Odgaard, A., Kabel, J. & Huiskes, R. Direct mechanics assessment of elastic symmetries and properties of trabecular bone architecture. *J. Biomech.* **29**, 1653–1657 (1996).
  115. Link, T. M. Osteoporosis Imaging: State of the Art and Advanced Imaging. *Radiology* **263**, 3–17 (2012).

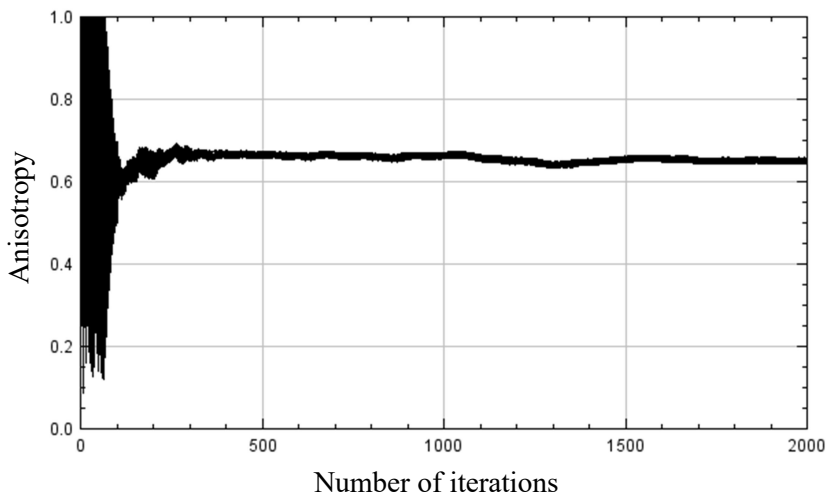
# Appendix

## A. Degree of Anisotropy

The convergences of a calculation of a degree of anisotropy (DA) with an error tolerance of 0.0005, on which fabric principal directions were based, on the macro level (Part I):



The convergence of a calculation of a DA with an error tolerance of 0.0005 on the micro level (Part II):




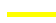

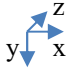
## B. Structural indices

Structural indices of 12 vertebral bodies, scanned with a resolution of 120 micron (= 0.12 mm) from 6 different spines:

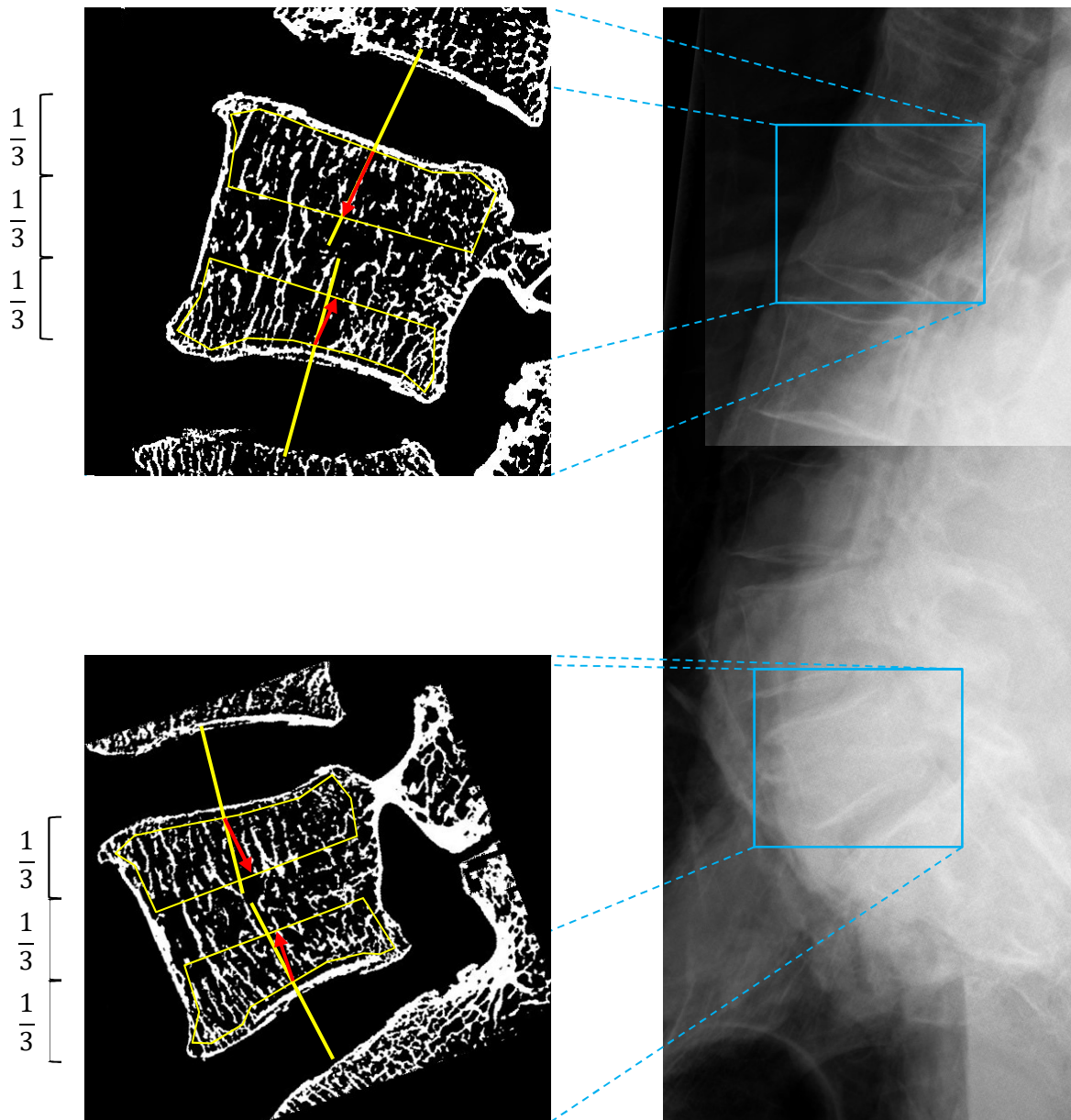
Spine	Vertebra	Sup./Infer.	BV/TV	Tb. Th. mean (pixels)	Tb. Sp. mean (pixels)	DA
<b>1</b>	L1	Superior	0.175	3.328	9.192	0.620
<b>1</b>	L1	Inferior	0.204	3.218	8.494	0.642
<b>1</b>	L5	Superior	0.191	3.284	8.619	0.607
<b>1</b>	L5	Inferior	0.214	3.027	7.756	0.648
<b>2</b>	L1	Superior	0.112	3.230	11.253	0.583
<b>2</b>	L1	Inferior	0.129	2.778	9.704	0.598
<b>2</b>	L5	Superior	0.102	2.915	12.197	0.634
<b>2</b>	L5	Inferior	0.111	3.059	11.746	0.512
<b>2.1</b>	L1	Superior	0.088	2.648	10.807	0.591
<b>2.1</b>	L1	Inferior	0.116	2.631	8.771	0.519
<b>2.1</b>	L5	Superior	0.133	2.890	8.971	0.619
<b>2.1</b>	L5	Inferior	0.130	2.726	8.971	0.590
<b>3</b>	L1	Superior	0.091	2.471	9.609	0.414
<b>3</b>	L1	Inferior	0.080	2.500	10.184	0.550
<b>3</b>	L5	Superior	0.058	2.441	12.563	0.522
<b>3</b>	L5	Inferior	0.132	2.483	8.055	0.408
<b>5</b>	L1	Superior	0.098	2.763	10.385	0.500
<b>5</b>	L1	Inferior	0.157	2.766	8.108	0.407
<b>5</b>	L5	Superior	0.176	3.195	8.295	0.684
<b>5</b>	L5	Inferior	0.196	3.251	8.492	0.707
<b>6</b>	L1	Superior	0.136	3.001	9.425	0.659
<b>6</b>	L1	Inferior	0.125	2.932	9.171	0.645
<b>6</b>	L5	Superior	0.086	2.781	10.748	0.644
<b>6</b>	L5	Inferior	0.091	2.749	10.493	0.714

### C. Trabecular primary orientation-normal to endplate visualizations

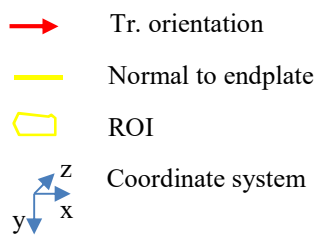
#### Spine 1

-  Tr. orientation
-  Normal to endplate
-  ROI
-  Coordinate system

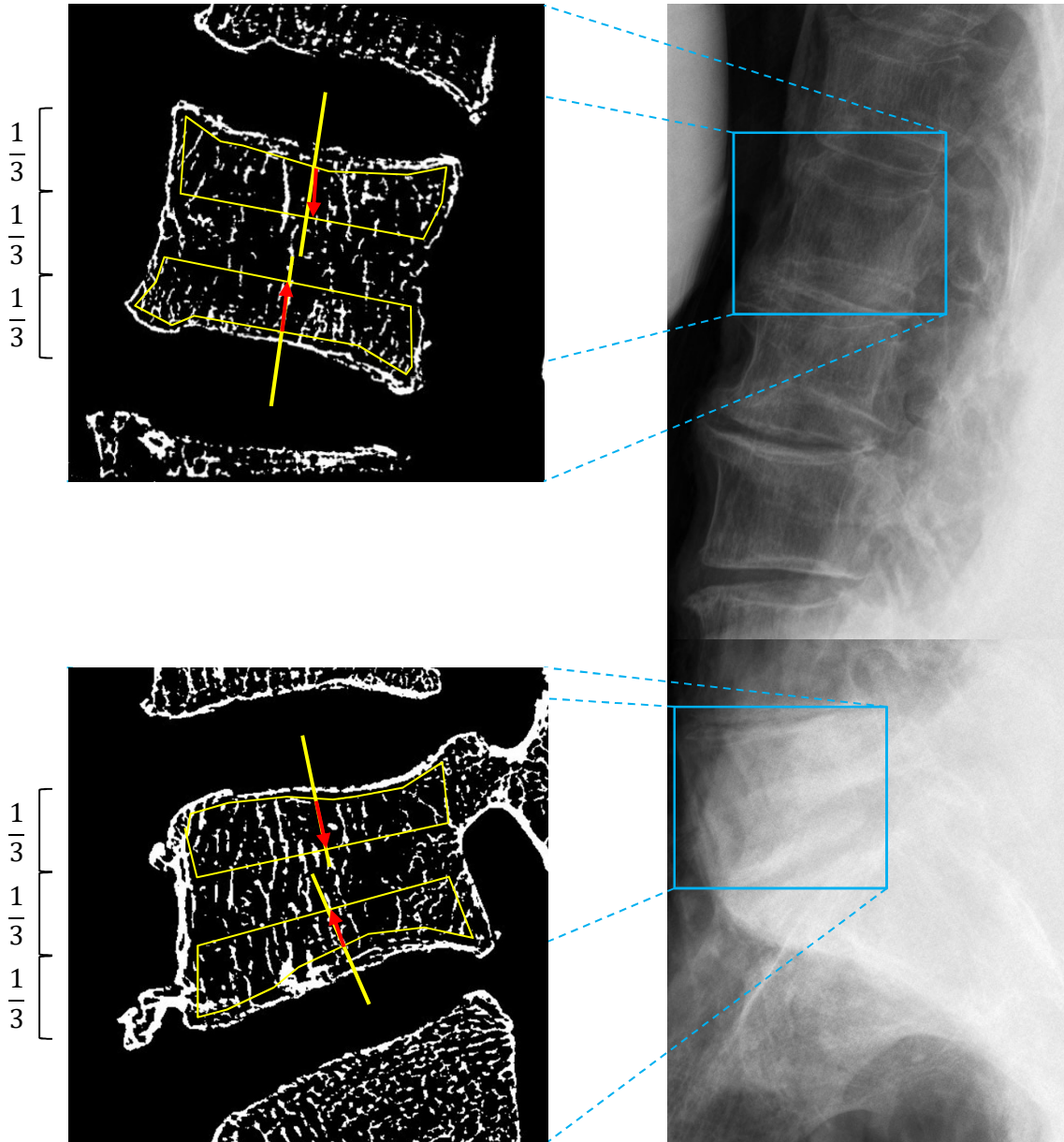
Ver.	Sup/Infer	$ \theta (^{\circ})$	Direction	BV/TV	DA
L1	Superior	0.883	Posterior	0.175	0.620
L1	Inferior	7.19	Posterior	0.204	0.642
L5	Superior	7.80	Posterior	0.191	0.607
L5	Inferior	4.15	Posterior	0.214	0.648






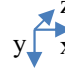
## Spine 2



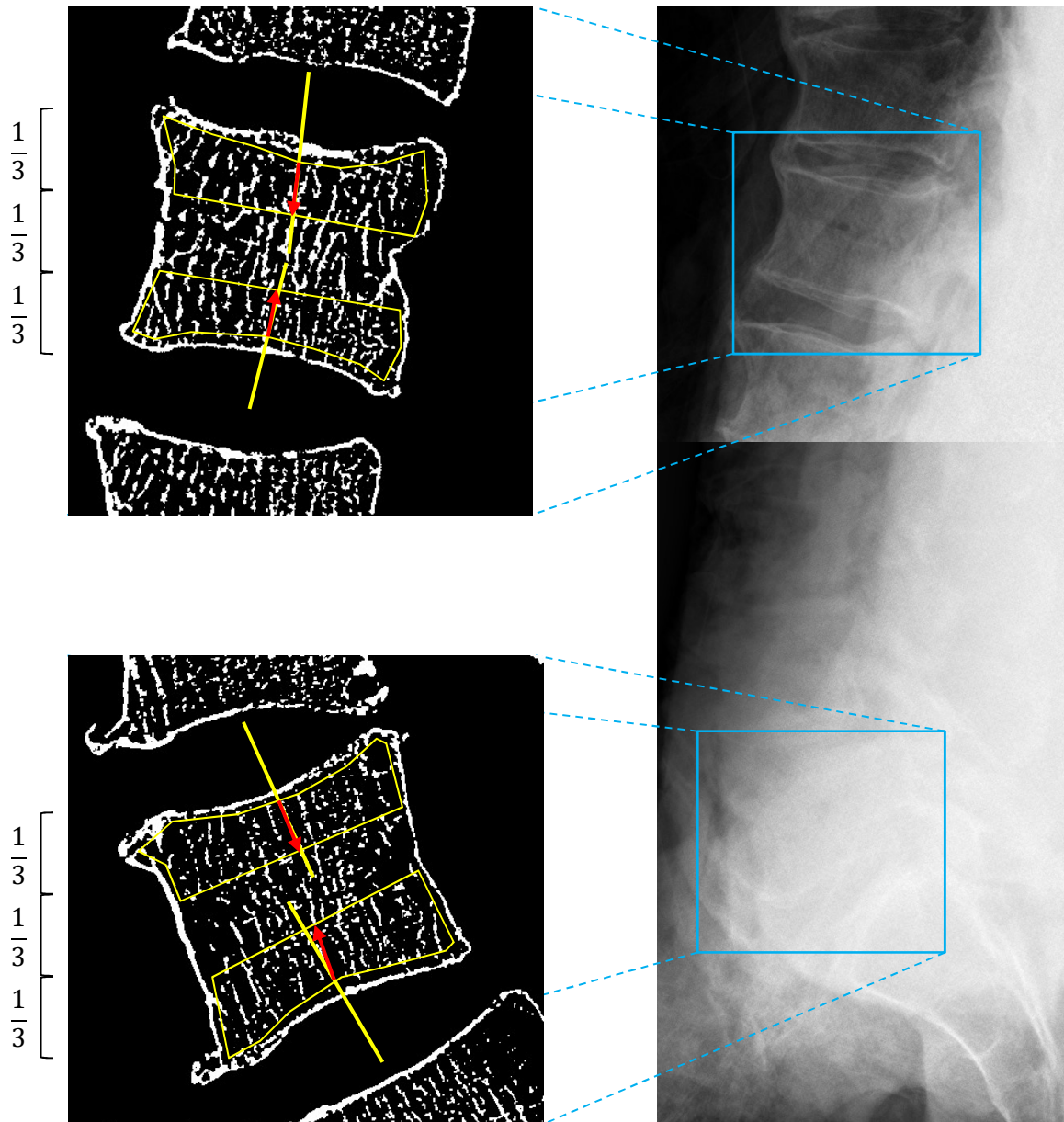
	Ver.	Sup/Infer	$ \theta (^{\circ})$	Direction	BV/TV	DA
L1	Superior		3.11	Posterior	0.112	0.583
L1	Inferior		1.44	Anterior	0.129	0.598
L5	Superior		0.526	Posterior	0.102	0.634
L5	Inferior		1.78	Posterior	0.111	0.512






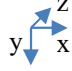
### Spine 3

-  Tr. orientation
-  Normal to endplate
-  ROI
-  Coordinate system

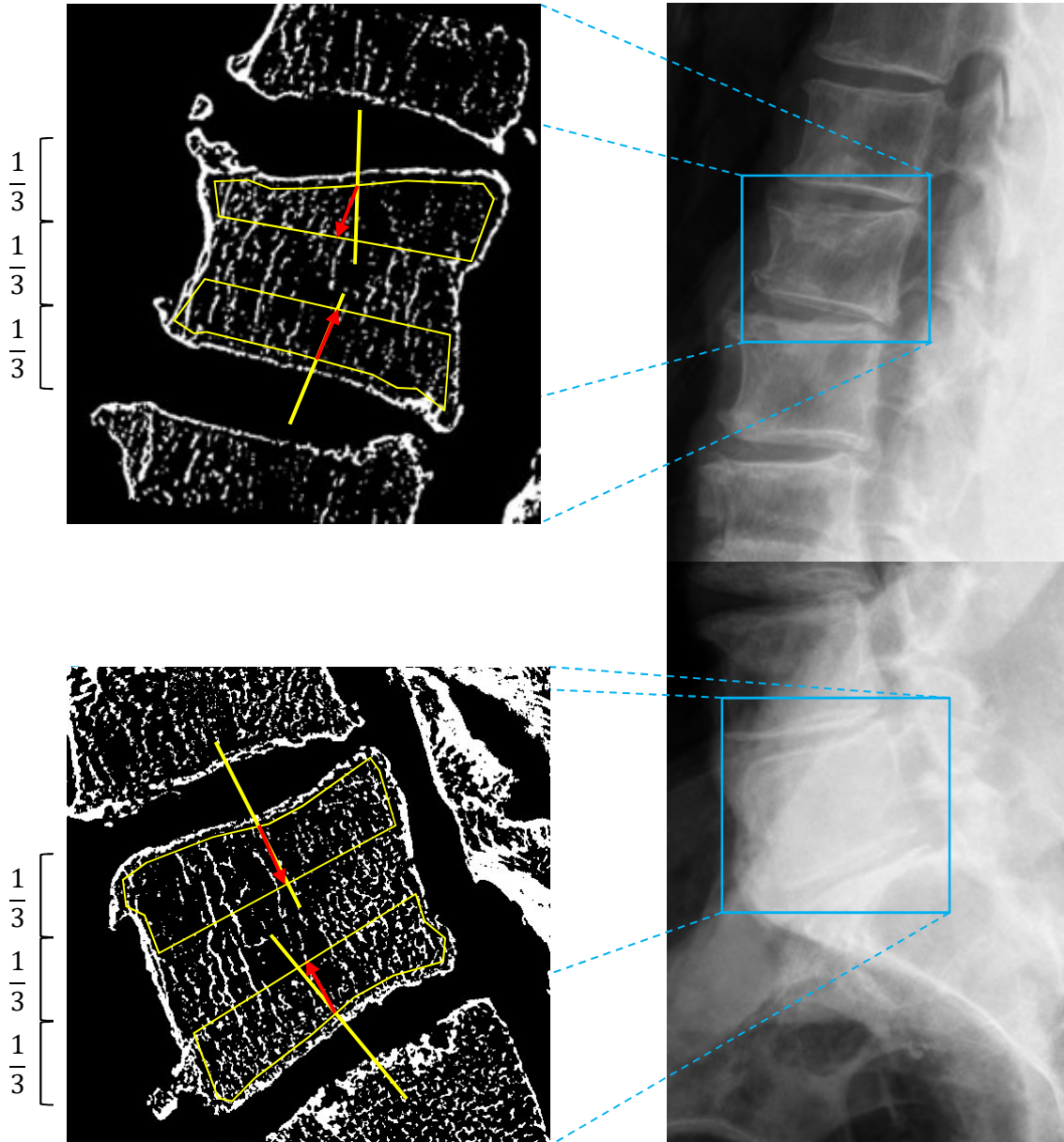
Ver.	Sup/Infer	$ \theta (^{\circ})$	Direction	BV/TV	DA
L1	Superior	0.474	Equal (Ant)	0.088	0.591
L1	Inferior	1.98	Anterior	0.116	0.519
L5	Superior	2.02	Anterior	0.133	0.619
L5	Inferior	8.66	Posterior	0.130	0.590



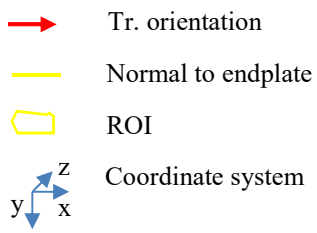
### Spine 4

-  Tr. orientation
-  Normal to endplate
-  ROI
-  Coordinate system

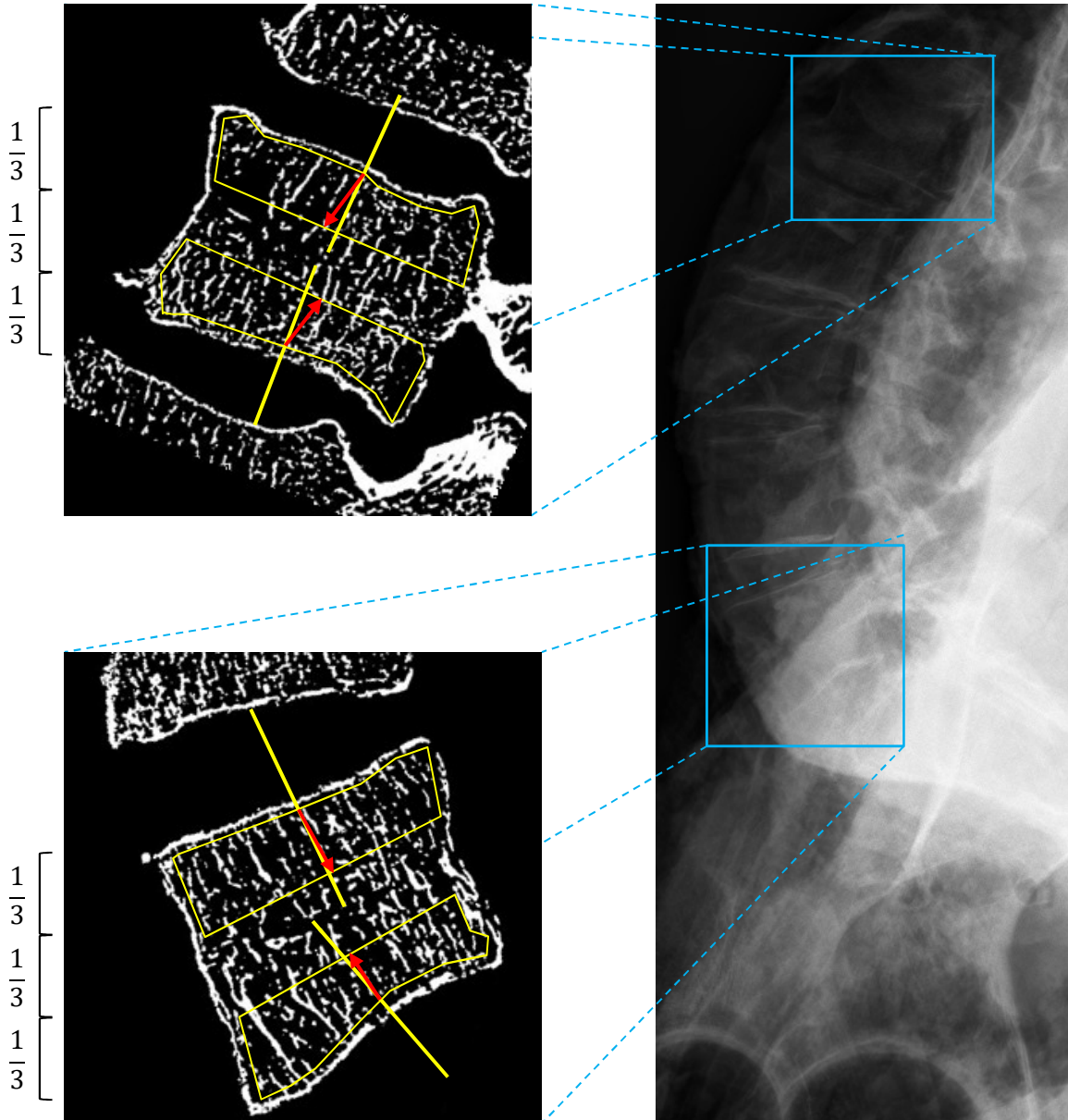
Ver.	Sup/Infer	$ \theta (^{\circ})$	Direction	BV/TV	DA
L1	Superior	17.32	Anterior	0.091	0.414
L1	Inferior	0.282	Equal	0.080	0.550
L5	Superior	1.34	Anterior	0.058	0.522
L5	Inferior	9.72	Posterior	0.132	0.408



## Spine 5

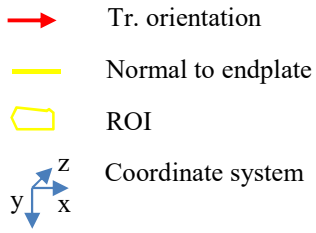


Ver.	Sup/Infer	$ \theta (^{\circ})$	Direction	BV/TV	DA
L1	Superior	9.12	Anterior	0.098	0.500
L1	Inferior	13.18	Posterior	0.157	0.407
L5	Superior	3.57	Posterior	0.176	0.684
L5	Inferior	7.98	Posterior	0.196	0.707

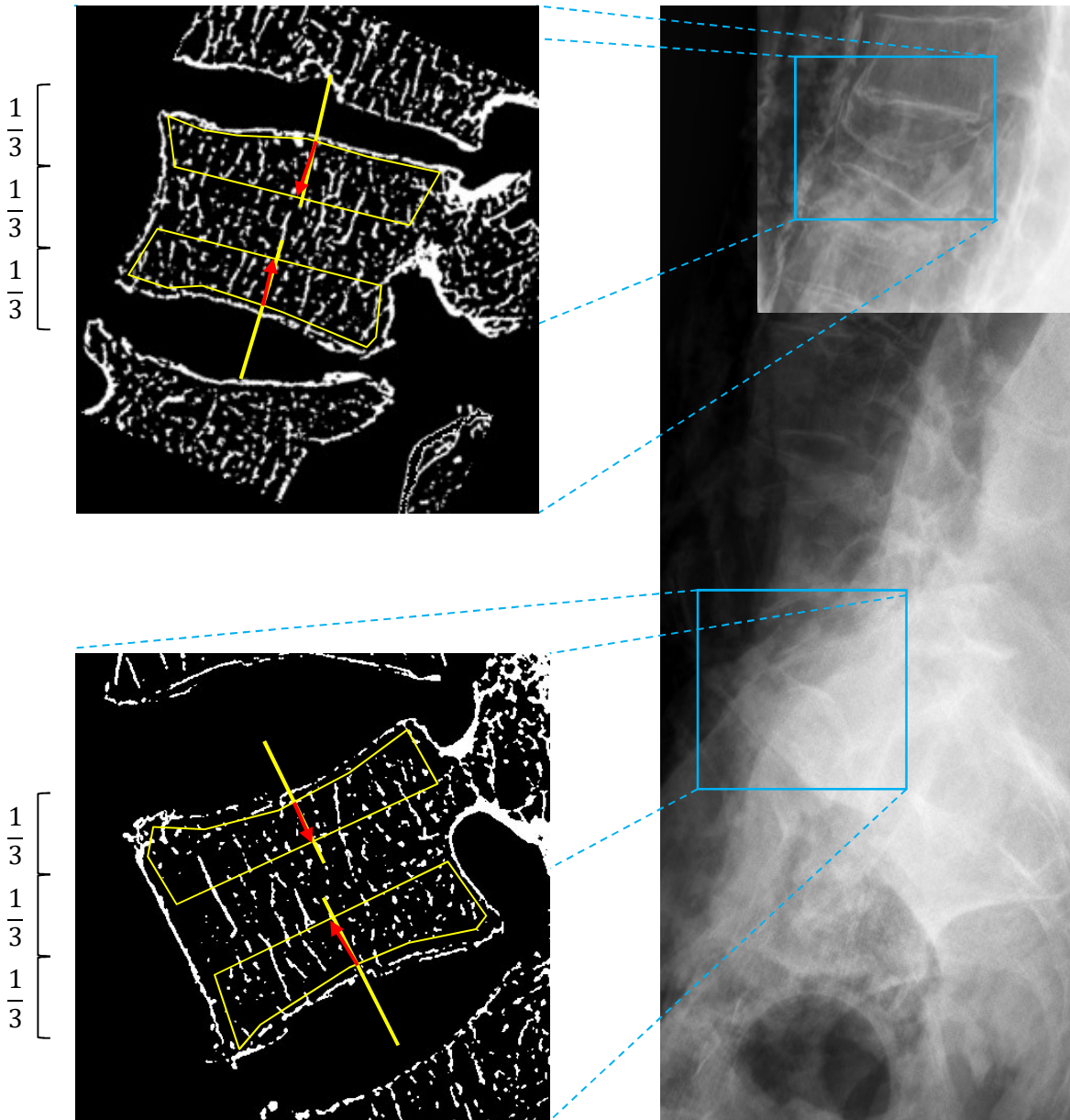




## Spine 6

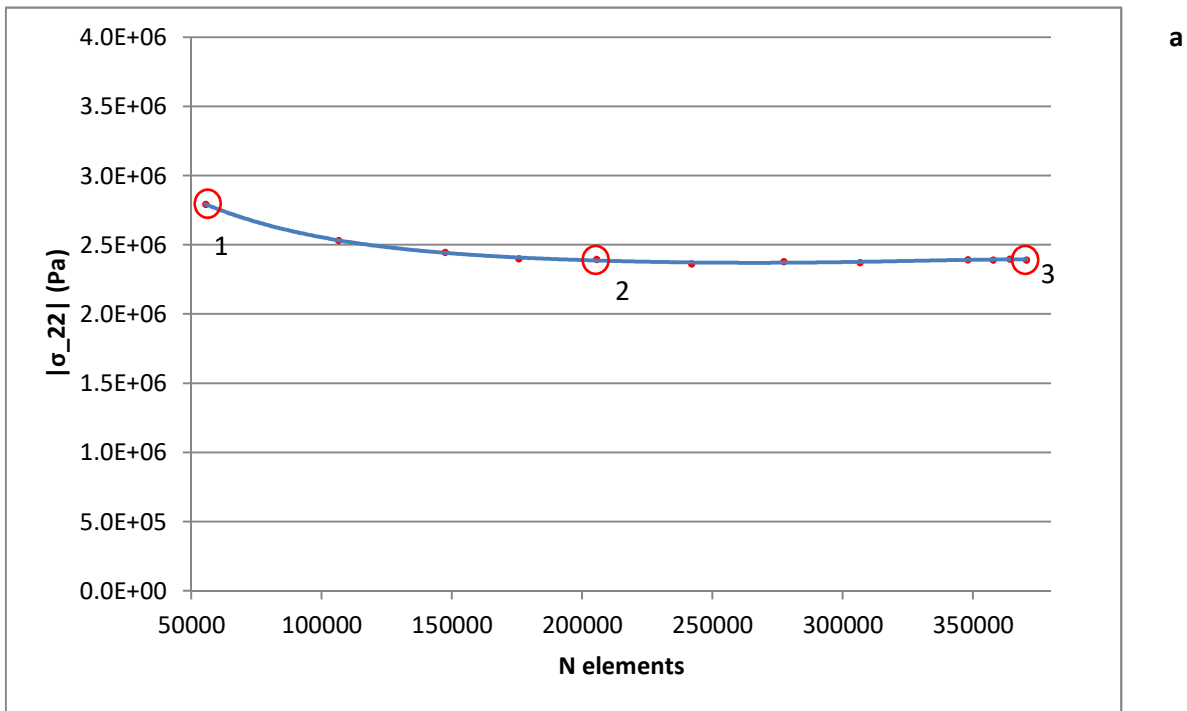


	Ver.	Sup/Infer	$ \theta (^{\circ})$	Direction	BV/TV	DA
	<b>L1</b>	Superior	3.62	Anterior	0.136	0.659
	<b>L1</b>	Inferior	2.62	Anterior	0.125	0.645
	<b>L5</b>	Superior	0.255	Equal (Ant)	0.086	0.644
	<b>L5</b>	Inferior	4.076	Anterior	0.091	0.714

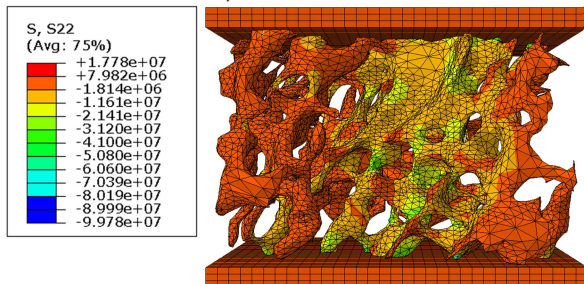


## D. Finite element model validation

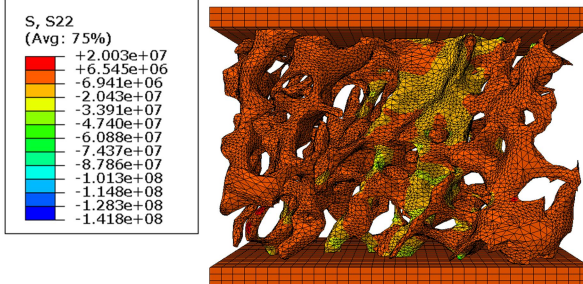
The FE-models were validated by evaluating the convergence of the solution of the FE-models as a result of mesh refinement. The stress levels of a trabecular bone cube in compression were calculated in relation to the element number. Figure 17 shows a clear convergence of the stress level of the cube as a consequence of an increase of element number. An element number of the mesh for the calculation of stiffness components was chosen at a point where convergence was apparent, corresponding to a division of the original element sizes, as pre-defined by Mimics, by 2. Although a larger element number would lead to more accurate outcomes, dividing the original element sizes by 2 was assumed sufficient for accurate FE-simulations without demanding too much computational costs.



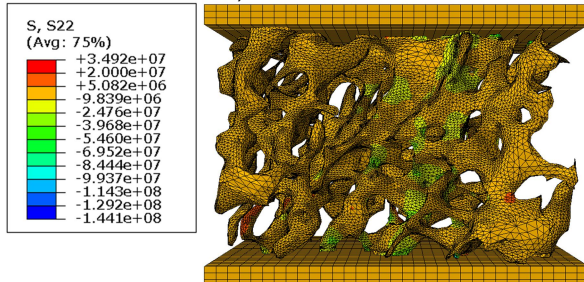
1. N elements = 55354; Runtime = 27s



2. N elements = 205462; Runtime = 75s



3. N elements = 370525; Runtime = 132s



**Figure 17:** **a** A polynomial with an accuracy of  $R^2=0.9976$  showing convergence of the average stress in the negative y (22)-direction at an increasing number of elements. **b** FE-models displaying the negative stress contributions over a cube of trabecular bone in compression at three refinements of element meshes corresponding to the circled points in the graph. The number of elements and runtime of the simulations are also given. Although colours of mesh 2 and 3 differ, stress values are in the same region, as the graph and stress legends indicate.



## E. Algorithm rotation to orthotropic elasticity

Program getmaindir in Fortran, retrieved from van Rietbergen et al.<sup>114</sup>

```
c*****
c Calculates the stiffness matrix in the best orthogonal
c coordinate system
c*****
  implicit none
  character(130) Ematfile
  integer
  1 i,
  1 j
  real(8)
  1 E2(6,6),
  1 E2r(6,6),
  1 Q(3,3)
  common/matmatr/E2,E2r,Q

c**** start

  write(6,*) 'Specify filename of matrixfile:'
  read(5,1000) Ematfile
1000 format(a)

  open(unit =10,
  1 file = Ematfile,
  1 form = 'FORMATTED',
  1 status = 'OLD',
  1 action = 'READ',
  1 err = 900)

  read(10,*,err=910) ((E2(i,j),j=1,6),i=1,6)

  write(6,*) 'Ematrix as read from file:'
  write(6,2000) ((E2(i,j),j=1,6),i=1,6)
2000 format(6f10.3)

  call maindir

  write(6,*) 'Ematrix after rotation:'
  write(6,2000) ((E2r(i,j),j=1,6),i=1,6)

  write(6,*)
  write(6,*) 'Rotation matrix:'
  write(6,2010) ((Q(i,j),j=1,3),i=1,3)
2010 format(3f10.3)
  goto 999

c**** error messages

900 write(6,*) ' ERROR: cannot open file: ',Ematfile
  goto 999
910 write(6,*) ' ERROR: format error in file: ',Ematfile
  goto 999
```

999 end

```
c*****
c MAINDIR.FOR Subroutine
c
c Calculates the mechanical main directions
c*****
  subroutine maindir
c =====
  implicit none
  integer(4) nmax
  parameter (nmax=3)
c common
  real(8)
  1 E2(6,6),
  1 E2r(6,6),
  1 Q(3,3)
  common/matmatr/E2,E2r,Q
c local
  integer(4)
  1 iter,
  1 n
  real(8)
  1 fret,
  1 ftol,
  1 p(nmax),
  1 pi,
  1 xi(nmax*nmax),
  1 R(3,3)      ! rotation matrix for sorting
ccor
  real(8),external :: OrthogError
ccor
c start

  pi= 2.0*asin(1.0)

  n= 3
  if (n.gt.nmax) then
    write(6,*) '!% Error in maindir; n>nmax'
    stop
  endif

  ftol= 1.0e-4

  call initpowell(n,
  2      p,
  3      xi)

  call powell(n,
  2      p,
  3      xi,
  4      ftol,
  5      iter,
  6      fret,
  7      OrthogError)

  return
```

```

end

c*****
c ORTHOGERROR.FOR Function
c
c Calculates the error if the matrix is considered as orthotropic
c*****
real(8) function OrthogError(x)
c =====
implicit none
c arguments
real(8)
1 x(3)
c common
real(8)
1 E2(6,6),
1 E2r(6,6),
1 Q(3,3)
common/matmatr/E2,E2r,Q
c local
real(8)
1 error,
1 eta,
1 fi,
1 teta
c start

c write(6,*) ' OrthogError'

fi = x(1)
teta= x(2)
eta = x(3)

c**** determine rotation matrix Q

Q(1,1)= cos(fi)*cos(eta)+sin(fi)*sin(teta)*sin(eta)
Q(2,1)= -sin(fi)*cos(eta)+cos(fi)*sin(teta)*sin(eta)
Q(3,1)= cos(teta)*sin(eta)
Q(1,2)= sin(fi)*cos(teta)
Q(2,2)= cos(fi)*cos(teta)
Q(3,2)= -sin(teta)
Q(1,3)= -cos(fi)*sin(eta)+sin(fi)*sin(teta)*cos(eta)
Q(2,3)= sin(fi)*sin(eta)+cos(fi)*sin(teta)*cos(eta)
Q(3,3)= cos(teta)*cos(eta)

c**** rotate the stiffness matrix E2 to E2r

call rotate4(E2,E2r,Q)

c**** calculate 'error' for orthogonal properties:

error= E2r(1,4)*E2r(1,4) +
+ E2r(1,5)*E2r(1,5) +
+ E2r(1,6)*E2r(1,6) +
+ E2r(2,4)*E2r(2,4) +
+ E2r(2,5)*E2r(2,5) +
+ E2r(2,6)*E2r(2,6) +
+ E2r(3,4)*E2r(3,4) +

```

```

+ E2r(3,5)*E2r(3,5) +
+ E2r(3,6)*E2r(3,6) +
+ E2r(4,5)*E2r(4,5) +
+ E2r(4,6)*E2r(4,6) +
+ E2r(5,6)*E2r(5,6)

```

```

OrthogError= error
return
end

```

```

c*****

```

```

c Rotate4.FOR Function

```

```

c

```

```

c Rotates a 4th rank tensor

```

```

c*****

```

```

subroutine rotate4(E2,E2r,Q)

```

```

c arguments

```

```

real(8)

```

```

1 E2(6,6),

```

```

1 E2r(6,6),

```

```

1 Q(3,3)

```

```

c local

```

```

integer(4)

```

```

1 i1,

```

```

1 i2,

```

```

1 ind(3,3),

```

```

1 j1,

```

```

1 j2,

```

```

1 k1,

```

```

1 k2,

```

```

1 l1,

```

```

1 l2

```

```

real(8)

```

```

1 E4(3,3,3,3),

```

```

1 E4r(3,3,3,3)

```

```

c*** set indices for rotation to 4th order tensor

```

```

ind(1,1)= 1

```

```

ind(1,2)= 6

```

```

ind(1,3)= 5

```

```

ind(2,1)= 6

```

```

ind(2,2)= 2

```

```

ind(2,3)= 4

```

```

ind(3,1)= 5

```

```

ind(3,2)= 4

```

```

ind(3,3)= 3

```

```

c*** translation matrix E2 to fourth-order tensor E4

```

```

do i1=1,3

```

```

do j1=1,3

```

```

do k1=1,3

```

```

do l1=1,3

```

```

E4(i1,j1,k1,l1)= E2(ind(i1,j1),ind(k1,l1))

```

```

enddo

```

```

enddo

```

```

enddo

```

```
enddo
```

```
c**** rotation of fourth-order tensor E4 to E4r
```

```
do i1=1,3
  do j1=1,3
    do k1=1,3
      do l1=1,3
        E4r(i1,j1,k1,l1)= 0.0d0
        do i2=1,3
          do j2=1,3
            do k2=1,3
              do l2=1,3
                E4r(i1,j1,k1,l1)= E4r(i1,j1,k1,l1) +
+ Q(i1,i2)*Q(j1,j2)*Q(k1,k2)*Q(l1,l2)*E4(i2,j2,k2,l2)
              enddo
            enddo
          enddo
        enddo
      enddo
    enddo
  enddo
enddo
```

```
c**** translation of E4r to second-order matrix E2r
```

```
do i1=1,3
  do j1=1,3
    do k1=1,3
      do l1=1,3
        E2r(ind(i1,j1),ind(k1,l1))= E4r(i1,j1,k1,l1)
      enddo
    enddo
  enddo
enddo
return
end
```

```
c*****
```

```
c INITPOWELL.FOR Subroutine
```

```
c
```

```
c From Numerical Recipies
```

```
c*****
```

```
subroutine initpowell(n,
```

```
2      p,
```

```
3      xi)
```

```
c
```

```
implicit none
```

```
c arguments
```

```
integer(4)
```

```
1 n
```

```
real(8)
```

```
1 p(n),
```

```
1 xi(n,n)
```

```
c local
```

```
integer(4)
```

```
1 i,
```

```

1 j
c start

c**** initial starting point

do i=1,n
  p(i)= 0.0
enddo

c**** initial direction vectors

do i=1,n
  do j=1,n
    xi(i,j)= 0.0
    if (i.eq.j) xi(i,j)= 1.0d0
  enddo
enddo

return
end

c*****
c POWELL.FOR Subroutine
c
c From Numerical Recipies
c*****
subroutine powell(n,
2      p,
3      xi,
4      ftol,
5      iter,
6      fret,
7      functie)
c =====
implicit none
integer(4) nmax
parameter (nmax=3)
c arguments
integer(4)
1 iter,
1 n
real(8)
1 ftol,
1 fret,
1 functie,
1 p(n),
1 xi(n,n)
external functie
c local
integer(4)
1 i,
1 ibig,
1 itmax,
1 j
real(8)
1 crit,
1 del,
1 errorcrit,

```



```

1  fp,
1  fptt,
1  t,
1  pt(nmax),
1  ptt(nmax),
1  xit(nmax)
c start

if (n.gt.nmax) then
  write(6,*) '!!% Program error in powell; n>nmax'
  stop
endif

itmax= 200

fret= funcie(p)
do j=1,n
  pt(j)= p(j)
enddo

iter= 0

1  iter= iter+1
  fp = fret
  ibig= 0
  del = 0.0
  do i=1,n
    do j=1,n
      xit(j)= xi(j,i)
    enddo
    fptt= fret
    call linmin(n,p,xit,fret)

    if (abs(fptt-fret).gt.del) then
      del= abs(fptt-fret)
      ibig= i
    endif
  enddo

  errorcrit= 2.0*abs(fp-fret)
  crit= ftol*(abs(fp)+abs(fret))
  if (2.0*abs(fp-fret).le.ftol*(abs(fp)+abs(fret))) then
    return
  endif

  if (iter.eq.itmax) write(6,*) '!!% Powell exceeding max. # iterat.',
  do j=1,n
    ptt(j)= 2.0*p(j)-pt(j)
    xit(j)= p(j)-pt(j)
    pt(j)= p(j)
  enddo
  fptt= funcie(ptt)
  if (fptt.ge.fp) goto 1
  t= 2.0*(fp-2.0*fret+fptt)*(fp-fret-del)**2-del*(fp-fptt)**2
  if (t.ge.0) goto 1

  call linmin(n,
2    p,

```

```

3      xit,
4      fret)

do j=1,n
  xi(j,ibig)= xi(j,n)
  xi(j,n)= xit(j)
enddo
goto 1
end

c*****
c  LINMIN.FOR Subroutine
c
c  From Numerical Recipies
c*****
  subroutine linmin(n,
2      p,
3      xi,
4      fret)
c =====
  implicit none
  integer(4) nmax
  parameter (nmax=3)
c arguments
  integer(4)
  1  n
  real(8)
  1  fret,
  1  p(n),
  1  xi(n),
  1  tol
c local
  integer(4)
  1  j,
  1  ncom,
  1  nmaxcom
  real(8)
  1  ax,
  1  bx,
  1  fa,
  1  fb,
  1  fx,
  1  xmin,
  1  xx,
  1  pcom(nmax),
  1  xicom(nmax),
  1  brent
ccor
  real(8),external :: fl dim
ccor
c commmon
  common/fl com/pcom,xicom,ncom,nmaxcom
c start
  tol  = 1.0d-4
  nmaxcom= nmax
  ncom  = n
  if (n.gt.nmax) then
    write(6,*) '!% Program error in linmin: n>nmax'

```

```

        stop
    endif

    do j=1,n
        pcom(j)= p(j)
        xicom(j)= xi(j)
    enddo
    ax= 0.0
    xx= 1.0

    call mnbrak(ax,
2       xx,
3       bx,
4       fa,
5       fx,
6       fb,
7       fl dim)

    fret= brent(ax,
2       xx,
3       bx,
4       fl dim,
5       tol,
6       xmin)
    do j=1,n
        xi(j)= xmin*xi(j)
        p(j)= p(j)+xi(j)
    enddo
    return
end

c*****
c  F1DIM.FOR Subroutine
c
c  From Numerical Recipies
c*****
real(8) function fl dim(x)
c =====
    implicit none
    integer(4) nmax
    parameter (nmax=3)
c arguments
    real(8)
    1  x
c local
    integer(4)
    1  j,
    1  n,
    1  nmaxcom
    real(8)
    1  orthogerror,
    1  p(nmax),
    1  xi(nmax),
    1  xt(nmax)
c common
    common/fl com/p,xi,n,nmaxcom
c start

```

```

if (n.gt.nmax .or. nmaxcom.ne.nmax) then
  write(6,*) '!% n,nmax,nmaxcom=',n,nmax,nmaxcom
  write(6,*) '!% Program error in fl dim; n>nmax or ncom<>nmax'
  stop
endif

do j=1,n
  xt(j)= p(j)+x*xi(j)
enddo
fl dim= OrthogError(xt)
return
end

c*****
c  BRENT.FOR Subroutine
c
c  From Numerical Recipies
c*****
  real(8) function brent(ax,
2      bx,
3      cx,
4      f,
5      tol,
6      xmin)
c =====
  implicit none
  real(8)
  1  cgold,
  1  zeps
  parameter (cgold= 0.3819660,
  1      zeps = 1.0e-10)
c arguments
  real(8)
  1  ax,
  1  bx,
  1  cx,
  1  tol,
  1  xmin
ccor
c  removed f from arguments declaration
  real(8),external :: f
ccor
c local
  integer(4)
  1  iter,
  1  itmax
  real(8)
  1  a,
  1  b,
  1  d,
  1  e,
  1  etemp,
  1  fu,
  1  fv,
  1  fw,
  1  fx,
  1  p,
  1  q,

```

```

1  r,
1  tol1,
1  tol2,
1  u,
1  v,
1  w,
1  x,
1  xm
c start

itmax= 500

a= min(ax,cx)
b= max(ax,cx)
v= bx
w= v
x= v
e= 0.0
fx= f(x)
fv= fx
fw= fx
do iter=1,itmax
  xm= 0.5*(a+b)
  tol1= tol*abs(x)+zeps
  tol2= 2.0*tol1
  if (abs(x-xm).le.(tol2-0.5*(b-a))) goto 3
  if (abs(e).gt.tol1) then
    r= (x-w)*(fx-fv)
    q= (x-v)*(fx-fw)
    p= (x-v)*q-(x-w)*r
    q= 2.0*(q-r)
    if (q.gt.0) p= -p
    q= abs(q)
    etemp= e
    e= d
    if (abs(p).ge.abs(0.5*q*etemp).or.p.le.q*(a-x).or.
+     p.ge.q*(b-x)) goto 1
    d= p/q
    u= x+d
    if (u-a.lt.tol2 .or. b-u.lt.tol2) d=sign(tol1,xm-x)
    goto 2
  endif
1  if (x.ge.xm) then
    e= a-x
  else
    e= b-x
  endif
  d= cgold*e
2  if (abs(d).ge.tol1) then
    u= x+d
  else
    u= x+sign(tol1,d)
  endif
  fu= f(u)
  if (fu.le.fx) then
    if (u.ge.x) then
      a= x
    else

```

```

        b= x
    endif
    v= w
    fv= fw
    w= x
    fw= fx
    x= u
    fx= fu
else
    if (u.lt.x) then
        a= u
    else
        b= u
    endif
    if (fu.le.fw .or. w.eq.x) then
        v= w
        fv= fw
        w= u
        fw= fu
    else if (fu.le.fv .or. v.eq.x .or. v.eq.w) then
        v= u
        fv= fu
    endif
endif
enddo
c  pause 'brent exceed max. # iterations'
write(6,*) '!% brent exceed max. # iterations (',itmax,')'
3  xmin= x
   brent= fx
   return
end

c*****
c  MNBRAK.FOR Subroutine
c
c  From Numerical Recipies
c*****
subroutine mnbrak(ax,
2      bx,
3      cx,
4      fa,
5      fb,
6      fc,
7      func)
c =====
implicit none
real(8)
1  gold,
1  glimit,
1  tiny
parameter (gold = 1.618034,
1      glimit= 100.0,
1      tiny = 1.0e-20)
c arguments
real(8)
1  ax,
1  bx,
1  cx,

```

```

1 fa,
1 fb,
1 fc,
1 func
external func
c local
real(8)
1 dum,
1 fu,
1 q,
1 r,
1 u,
1 ulim
c start

fa= func(ax)
fb= func(bx)
if (fb.gt.fa) then
  dum= ax
  ax= bx
  bx= dum
  dum= fb
  fb= fa
  fa= dum
endif
cx= bx+gold*(bx-ax)
fc= func(cx)
1 if (fb.ge.fc) then
  r= (bx-ax)*(fb-fc)
  q= (bx-cx)*(fb-fa)
  u= bx-((bx-cx)*q-(bx-ax)*r)/(2.0*sign(max(abs(q-r),tiny),q-r))
  ulim= bx+glimit*(cx-bx)
  if ((bx-u)*(u-cx).gt.0) then
    fu= func(u)
    if (fu.lt.fc) then
      ax= bx
      fa= fb
      bx= u
      fb= fu
      return
    else if (fu.gt.fb) then
      cx= u
      fc= fu
      return
    endif
    u= cx+gold*(cx-bx)
    fu= func(u)
  else if ((cx-u)*(u-ulim).gt.0) then
    fu= func(u)
    if (fu.lt.fc) then
      bx= cx
      cx= u
      u= cx+gold*(cx-bx)
      fb= fc
      fc= fu
      fu= func(u)
    endif
  else if ((u-ulim)*(ulim-cx).ge.0.0) then

```

```
u= ulim
fu= func(u)
else
u= cx+gold*(cx-bx)
fu= func(u)
endif
ax= bx
bx= cx
cx= u
fa= fb
fb= fc
fc= fu
goto 1
endif
return
end
```